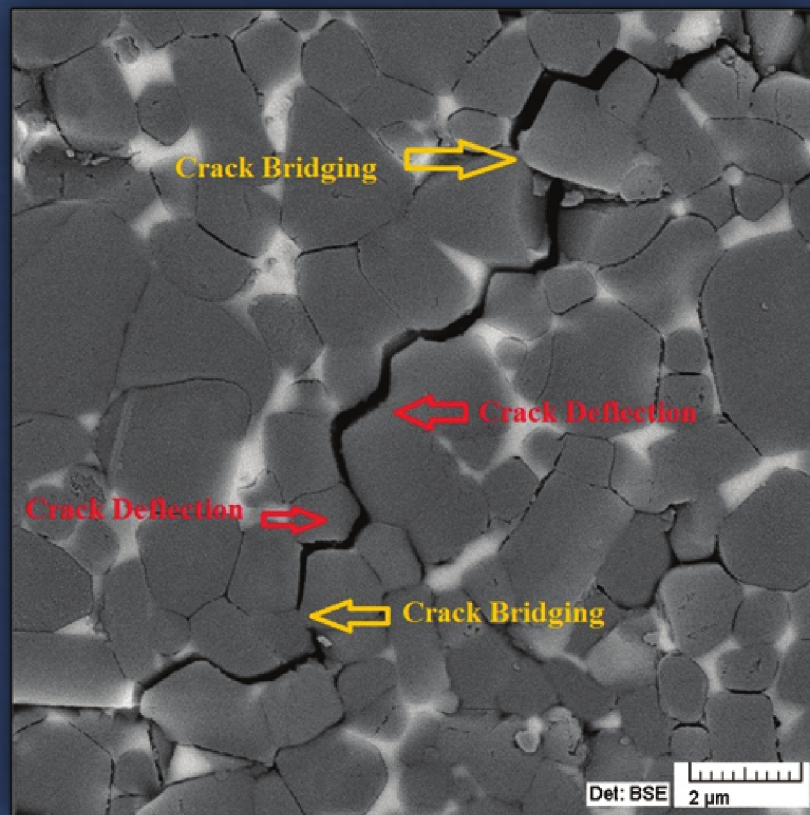


Advanced Ceramics Progress



Materials and Energy
Research Center



Iranian Ceramic Society

In The name of God

Advanced Ceramics Progress

DIRECTOR IN CHARGE

A. R. Khavandi

EDITOR IN CHIEF

M. R. Rahimipour

EXECUTIVE MANAGER

M. Razavi

EDITORIAL BOARD

- | | |
|---|--|
| A. R. Aghaei, Materials and Energy Research Center | M. R. Rahimipour, Materials and Energy Research Center |
| P. Alizadeh, Tarbiat Modares University | M. Razavi, Materials and Energy Research Center |
| T. Ebadzadeh, Materials and Energy Research Center | E. Salehi, Materials and Energy Research Center |
| M. A. Faghihi Sani, Sharif University of Technology | M. Salehi, Isfahan University of Technology |
| M. M. Mohebi, Imam Khomeini University | M. T. Salehi, Iran University Science and Technology |

EDITORIAL ADVISORY BOARD

Ş. Tǎlu, F.S. Torknik

ENGLISH LANGUAGE EDITUR

M. Sabzevari

TECHNICAL STAFF

E. Pouladi, V. Hajabdolali, R. Chaluei

DISCLAIMER

The publication of papers in Advanced Ceramics Progress does not imply that the editorial board, editorial advisory board, reviewers or the publisher accept, approve or endorse the data and conclusions of authors.

Advanced Ceramics Progress (ISSN 2423-7477) (e-ISSN 2423-7485)

Web Site: www.acerp.ir, E-mail: office@acerp.ir

Tel: +98 (0) 26 36280040-7 ext.: 382, Fax: +98 (0) 26 36201888

Tel:+98 (0)21 88771626-7 ext.: 8931, Fax: +98 (0)21 88773352

Materials and Energy Research Center (MERC); Iranian Ceramic Society (ICERS)

CONTENTS

S. M. Nahvi	Effect of Carbide Particle Size on the Microstructure, Mechanical properties, and Wear Behavior of HVOF-sprayed WC-17% Co Coatings	1-14
M. Khodaei, O. Yaghoobizadeh, S. A. Safavi, N. Ehsani, H. R. Baharvandi, S. Esmaceli	The Effect of TiC Additive with Al ₂ O ₃ -Y ₂ O ₃ on the Microstructure and Mechanical Properties of SiC Matrix Composites	15-24
P. Safarzadeh Kermani, M. Ghatee, A. Yazdani	Synthesis and Characterization of Barium Aluminosilicate Glass as the Sealant for Solid Oxide Fuel Cell Application	25-30
J. Esmacilzadeh, H. Setayesh	Bioabsorbable Screws for Anterior Cruciate Ligament Reconstruction Surgery: A Review	31-46
M. Rezvani, E. Alahgholiyan, L. Roshangar	Synthesis of a Macroporous Glass-Ceramic Scaffold Containing Fluorapatite Crystalline Phase for Bone Substitutes	47-54
M. Hanachi, Z. S. Seyedraoufi, V. Abouei	Investigation of Microstructure, Hardness, and Corrosion Resistance of Ni-P-GO Electroless Nanocomposite Coating on AZ31D Alloy Surface	55-62



Effect of Carbide Particle Size on the Microstructure, Mechanical properties, and Wear Behavior of HVOF-sprayed WC-17% Co Coatings

S. M. Nahvi ^{a *}

^a Department of Materials Engineering, Isfahan University of Technology, Isfahan, 84156-83111, Iran

PAPER INFO

Paper history:

Received 25 April 2020
Accepted in revised form 18 May 2020

Keywords:

WC-Co
HVOF
Microstructure
Mechanical Properties
Abrasive Wear

ABSTRACT

This study investigates the effect of carbide particle size on the microstructure, mechanical properties, and abrasive wear resistance of WC-17%Co HVOF-sprayed coatings. The characteristics of WC-1, WC-2, and WC-3 coatings with carbide sizes of 1 μm , 0.9 μm , and 0.5 μm , respectively, were also investigated. WC-1 coating experienced the maximum carbon loss of 42%, while WC-2 and WC-3 coatings underwent lower carbon losses of 30% and 29%, respectively. The XRD pattern revealed $\text{W}_2\text{C}/\text{WC}$ peak ratios of 15.58, 9.14, and 14.96% for WC-1, WC-2, and WC-3 coatings, respectively. The Vickers microhardness of WC-1, WC-2, and WC-3 coatings was measured as 1418 ± 61 , 1306 ± 71 , and 1203 ± 57 kgf/mm^2 , respectively. The WC-2 coating showed the maximum fracture toughness of 5.9 $\text{MPa}\cdot\text{m}^{1/2}$, after which WC-3 and WC-1 coatings were characterized by 5.6 and 5.4 $\text{MPa}\cdot\text{m}^{1/2}$, respectively. The wear rate of the coatings abraded by alumina 60 was 1.2-7.8 times higher than that of the coatings abraded by silica 70 almost over the whole range of applied loads (19.6-127.5 N). The WC-3 coating exhibited lower abrasive wear resistance against alumina 60 than WC-1 and WC-2 coatings. The worn surfaces produced by alumina 60 abrasive showed indications of grooving, pitting, and cutting of the coatings' surfaces. For all coatings abraded by silica 70, removal of the matrix, micro-grooving, carbide particles fragmentation, and voids formation through carbide pullout were detected. For WC-3 coating, in contrast to WC-2 and WC-3, the indications of sub-surface cracking were identified when abraded by both alumina 60 and silica 70.

1. INTRODUCTION

Sintered WC-Co materials consisting of hard WC particles and a ductile cobalt binder phase are extensively utilized in wear-resistant applications such as cutting and machining tools, extrusion dies, etc. due to their excellent combination of high hardness, fracture toughness, and superior wear resistance [1-4]. Due to a decrease in WC particle size on the nanometer scale, the mean free path of cobalt matrix is reduced, thus resulting in greater resistance against deformation and binder phase extrusion. As a result, compared to conventional materials, sintered nanostructured WC-Co materials exhibited higher hardness and greater wear resistance [5-8]. Thermally sprayed WC-Co coatings, mostly deposited by High Velocity Oxygen Fuel (HVOF) spraying, have also received increasing attention and is utilized in numerous applications such as seats and gates in the petroleum industry, as well as copper crystallizers

and pinch rolls in the steel industry [9-11]. Researchers have studied the same approach with respect to nanostructured WC-Co coatings; however, the obtained results of the performance of coatings have been controversial to date. In other words, a review of several related studies shows that HVOF-sprayed nanostructured WC-Co coatings outperform conventional WC-Co coatings in terms of their higher hardness, wear resistance, and lower friction coefficient [12-14]. However, other researchers reached a different conclusion [15-18]. Therefore, additional investigations are required in this domain in order to explore a comprehensive study on WC-Co coatings and the relationship among the carbide particle size, mechanical properties, and wear resistance.

In the present study, WC-17%Co powders of three different carbide particle sizes were deposited by HVOF thermal spraying. The effect of carbide particle size on the mechanical properties, microstructure, and abrasive

* Corresponding Author Email: mehran.nahvi@cc.iut.ac.ir (S. M. Nahvi)

wear resistance was evaluated.

2. EXPERIMENTAL PROCEDURES

2.1. FEEDSTOCK POWDERS AND HVOF COATINGS

Three commercial WC-Co powders with different WC particle sizes of 1 (WC-1), 0.9 (WC-2), and 0.5 μm (WC-3) were utilized as HVOF feedstock materials. All powders were agglomerated and sintered spheroids with nominal diameters ranging from 15 to 45 μm . Malvern Mastersizer S (Malvern Instruments Ltd, Worcestershire, UK) laser particle size analyzer was utilized to measure the particle-size distribution of the powders. Table 1 presents the general properties of the powders.

TABLE 1. General properties of WC-Co powders

Powder	Manufacturer	Powder designation	WC size (μm)	Composition (wt%)			
				W	Fe	Co	C
WC-1	H.C. Starck	Amperite 526	1	78.09	0.05	16.83	5.03
WC-2	Sulzer Metco	Woka 3202	0.9	77.97	0.04	16.83	5.16
WC-3	Sulzer Metco	Woka 3202 FC	0.5	77.85	0.03	17.02	5.1

Plain-carbon steel (0.12% C, 0.7% Mn) sheets with dimensions of $59 \times 25 \times 3$ mm and hardness of 241 kgf.mm^{-2} were used as substrates for coating deposition. Prior to HVOF spraying, grit blasting the substrates with ~ 250 μm brown alumina is required to degrease and roughen the surface. Praxair/UTP Top-Gun HVOF spray system, whose parameters are specified in Table 2, was used to spray the feedstock powders onto the substrates. Hydrogen and nitrogen as the fuel and carrier gases, respectively, were used and the samples were cooled with compressed air jets during spraying.

TABLE 2. Spray parameters employed for coatings deposition

Spray parameter	WC-1	WC-2	WC-3
O ₂ flow rate (l min^{-1})	240	240	240
Fuel gas (H ₂) flow rate (l min^{-1})	640	640	640
Carrier gas (N ₂) flow rate (l min^{-1})	17	17	17
Spray distance (mm)	250	250	250
Number of pass	40	40	40
Length of pass (mm)	77	77	77
Carousel diameter (mm)	280	280	280
Substrate velocity (m s^{-1})	1	1	1
Gun transverse speed (mm s^{-1})	5	5	5
Coating time (s)	733	674	669
Consumption of powder (g)	665	710	711
Coating thickness (μm)	350	445	460
Powder feed rate (g min^{-1})	54	63	63

2.2. MICROSTRUCTURAL CHARACTERIZATIONS

This study used X-Ray Diffraction (XRD) (Siemens D500 diffractometer, 40 kV, 25 mA) to identify the phase composition of the powders and coatings via monochromatic Cu K α ($\lambda = 0.15406$ nm) radiation. The XRD spectra were recorded over a 2θ range of 30° – 80° with a step size of 0.010° and 4s dwell time per step. Scanning Electron Microscope (SEM) (Philips XL30, FEI Ltd.) equipped with energy dispersive X-ray (EDX) analysis was used for microstructural examination of feedstock powders and as-sprayed coatings. SEM observations were carried out at an accelerating voltage value of 20 kV in both Secondary Electron (SE) and Back-Scattered Electron (BSE) modes. Image analysis software (ImageJ 1.41) evaluated SEM/BSE images at a magnification of $2500\times$ to figure out the porosity of the coatings. The mean pore volume fraction was calculated by recording at least ten images. The line analysis method derived from BSE micrographs at magnifications ranging from 5000 to $10000\times$ was utilized to estimate the volume fraction of phases and the carbide particle size of the powders and coatings. Chemical analysis of as-sprayed coatings by LSM Ltd. (London and Scandinavian Metallurgical Co. Limited, South Yorkshire, UK) was conducted. While XRF-HSS (quantitative) was applied to determine Oxygen and Carbon contents, X-Ray Fluorescence (XRF) technique using XRF-UniQuant (semiquantitative) was used to determine other elements.

2.3. EVALUATION of MECHANICAL PROPERTISE

LECO M-400 microhardness tester was applied in this study to measure Vickers microhardness of as-sprayed coatings under a load of 300 gf at a dwell time interval of 15 s. The coatings' hardness is described as the average value of 10 indents taken along the mid-plane of the cross-section parallel to the coating/substrate interface.

An indentation method was utilized to measure the coatings' fracture toughness. To this end, Vickers indentation measurements were performed on the metallographically prepared cross-sections of the coating under a load of 5 kgf. The image analysis software (ImageJ 1.41) was also utilized to measure the length of cracks parallel to the substrate/coating interface via optical micrographs at a magnification of $400\times$. At least 35 indentations were conducted for each coating. The model proposed by A.G. Evans and T.R. Wilshaw was considered to calculate the coatings' fracture toughness (K_{IC}) [19]:

$$K_{IC} = 0.079 \left(\frac{P}{a^{3/2}} \right) \log \left(\frac{4.5a}{c} \right) \quad (1)$$

where P is the applied indentation load (N), a is the indentation half diagonal (m), and c is the crack length from the center of the indent (m). The recommended c/a ratio for valid use of this equation is $0.6 \leq c/a < 4.5$.

2.4. ABRASIVE WEAR TESTING

To carefully study the coatings' behavior under three-body low stress-abrasion conditions, Dry Sand Rubber Wheel (DSRW) test was applied to test the samples. As shown in Fig. 1, the coating sample is held in a slot at the top of the rotating wheel to control the feed of abrasive to be passed between the wheel and the sample.

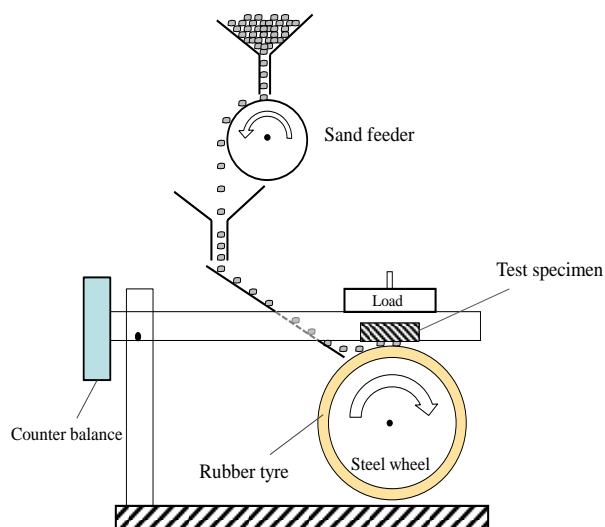


Figure 1. Schematic representation of dry sand rubber wheel abrasion test apparatus

The rubber wheel made of a polyurethane cast elastomer (monothane A60; CIL, Preston, UK) was coated around an inner steel wheel to increase the total diameter to 227 mm. According to Wallace Hardness Meter, the width and international rubber hardness of the tyre were 12 mm and 63 ± 3 degrees, respectively. The rotation speed of the rubber was set at 195 rpm, equivalent to the sliding speed of 2.32 m s^{-1} and in agreement with ASTM standard G65.

This study used two groups of abrasives: (a) angular alumina 60 (Abrasive Developments, Henley-in-Arden, UK) in a size range of 212 to 300 μm and sand feed rate of 2.64 g s^{-1} , and (b) rounded silica 70 (The David Ball Company, Bar Hill, UK) in the size range of 180 to 250 μm and sand feed rate of 2.37 g s^{-1} (Fig. 2). The LECO M-400 micro hardness tester at load hardness of 300 gf was used to measure the hardness of the abrasive particles. Abrasive particles were mounted on a hot hardening resin and, then, polished in order to keep the

flat cross-section of the particles exposed to indentation. The reported hardness is the average of 5 indents taken from different regions. The Vickers hardness rates of silica 70 and alumina 60 abrasives assessed in the polished cross-sections with an indentation load of 300 gf were $1116 \pm 47 \text{ kgf.mm}^{-2}$ and $2103 \pm 25 \text{ kgf.mm}^{-2}$, respectively.

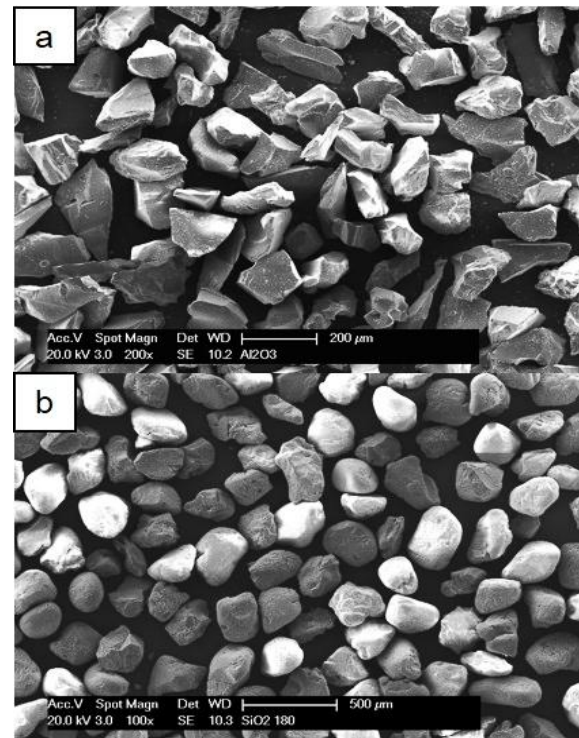


Figure 2. SEM images of (a) alumina 60 and (b) silica 70 abrasive particles

The wear experiments were carried out under the applied loads of 19.6, 49, 98, and 127.5 N. The abrasive particles were fed via a chute towards the rubber wheel just before the contact region between the test specimen and the wheel.

Before and after each test, the coatings' loss of mass was assessed through a GF-200 balance (A&D Instruments Ltd., Tokyo, Japan) with capacity and accuracy of 10g and 0.001 g, respectively. Prior to calculating the wear loss, the coating samples were washed in methanol and, then, dried. For the coating samples, the abrasion distances were 800, 1600, 2400, 3200, and 4000 revolutions. The wear rate was obtained from the slope of the steady state part of the mass loss versus sliding distance graph.

The wear mechanisms were studied by observing the worn surface of the coating samples using Scanning Electron Microscopy (SEM) (Philips XL30, FEI Ltd, Cambridge, UK) with an accelerating voltage of 20 kV

in Secondary Electron (SE) and Back-Scattered Electron (BSE) imaging modes.

3. RESULTS

3.1. MICROSTRUCTURE OF FEEDSTOCK POWDERS AND HVOF COATINGS

The XRD patterns of WC-1, WC-2, and WC-3 powders (Fig. 3) show the main peaks corresponding to WC phase and small peaks related to Co matrix. The XRD patterns reveal no additional carbide phase such as W_2C indicating that all the tungsten content in the starting powders exists in the form of WC phase.

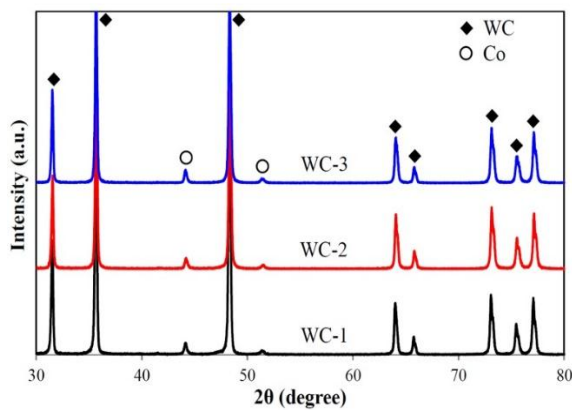


Figure 3. XRD patterns of starting WC-1, WC-2, and WC-3 powders

Fig. 4 shows the SEM images from morphology and cross-section of WC-1, WC-2, and WC-3 powders. It is evident that the agglomerated and sintered particles possess a spherical morphology and a highly porous structure.

The results of the analysis conducted on the particle size distribution of different powders (Fig. 5), derived from laser diffractometry technique, reveal deviations from the size range and average size of particles in a way that WC-1 and WC-2 powders indicate the minimum and maximum $d_{50\%}$ of 32 and 38 μm , respectively.

Table 3 presents the particle size and volume fraction of WC phase calculated according to the cross-sectional BSE images of the powders through the line analysis method. Moreover, given the assumption that WC and Co densities are $15.63 \text{ g}\cdot\text{cm}^{-3}$ [22] and $8.90 \text{ g}\cdot\text{cm}^{-3}$, respectively, Table 3 shows the calculated volume fraction of WC based on the mass fractions claimed by the manufacturers. The results obtained from the calculated volume fraction of WC phase are in good agreement with each other, which verifies their accuracy.

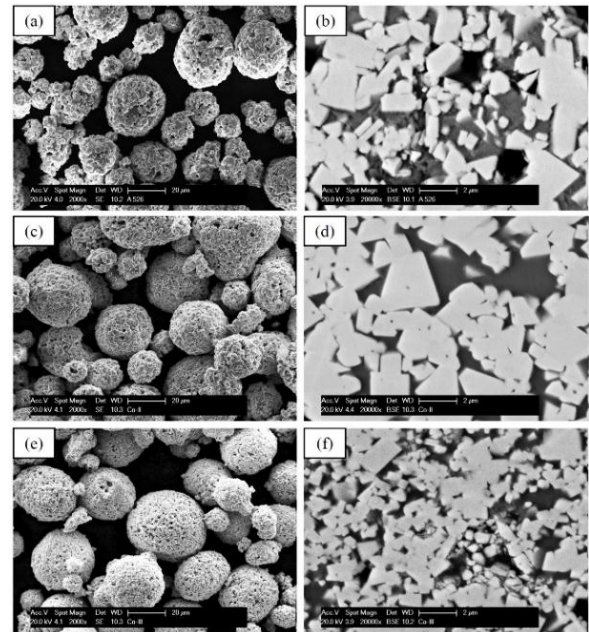


Figure 4. SEM images from morphology and cross-section of (a,b) WC-1, (c,d) WC-2, and (e,f) WC-3 powder particles

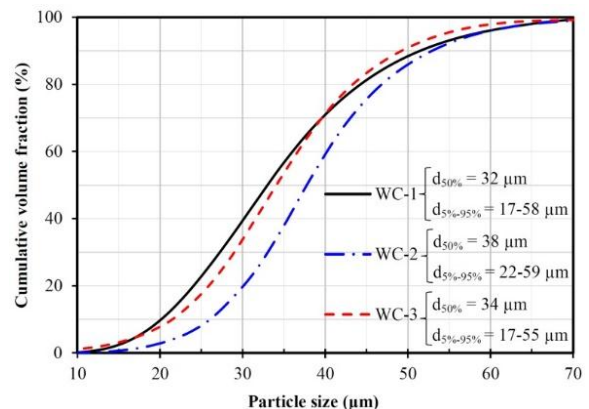


Figure 5. Particle size analysis of WC-1, WC-2, and WC-3 powder particles

TABLE 3. Particle size and volume fraction of WC in the powders measured via line analysis and calculated from the chemical composition of the powders

Powder	Measured volume fraction of WC (%)	Calculated volume fraction of WC (%)	WC particle size (μm)
WC-1	72	74	1.0
WC-2	67	74	0.9
WC-3	71	73	0.5

Table 4 presents the chemical composition, carbon loss, and (W_2C/WC) peak ratio of as-sprayed coatings. Obviously, for all coatings, significant carbon loss during HVOF spraying was observed. While WC-1 coating experienced the highest rate of carbon loss (42%), WC-2 and WC-3 coatings underwent lower rates, i.e., 30% and 29%, respectively.

Fig. 6 shows the comparative XRD patterns of WC-1, WC-2, and WC-3 coatings sprayed under the conditions specified in Table 2.

TABLE 4. Chemical composition, carbon loss, and (W_2C/WC) peak ratio for different coatings

Coating	Composition (wt%)				Carbon loss (%)	XRD peak height ratio (W_2C/WC) $\times 100$
	W	Fe	Co	C		
WC-1	79.90	0.05	17.16	2.89	42	15.58
WC-2	79.26	0.04	17.09	3.61	30	9.14
WC-3	79.05	0.03	17.29	3.63	29	14.96

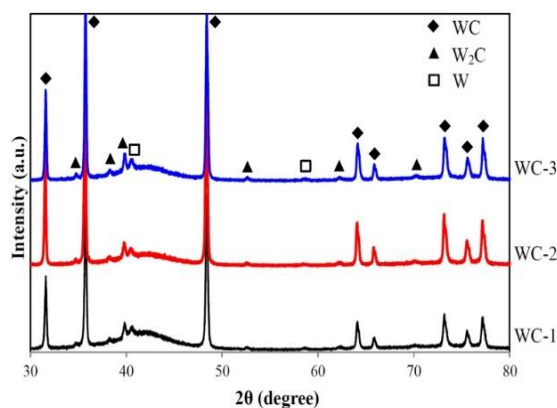


Figure 6. XRD patterns of as-sprayed WC-1, WC-2, and WC-3 coatings

According to the observations, all types of coating experience WC decarburization during HVOF spraying. However, the levels of WC decarburization are different. When WC-1, WC-2, and WC-3 powder particles are exposed to high-temperature HVOF flame ($\sim 3000^\circ C$), Co matrix melts upon which WC particles begin to dissolve into the liquid Co. The oxidizing atmosphere of HVOF flame makes a portion of dissolved Carbon oxidized in the form of CO/CO_2 gas mixture that finally leads to decarburization. Some of the remaining dissolved W and C are recrystallized as W_2C and W phases in the solidification process and the rest are kept in the binder to form W-rich Co matrix [23-25]. For all coatings, XRD peaks that correlate with W_2C and W phases formed during deposition are

detected. A broad diffraction halo between 2θ values of approximately 37 and 47° for each coating is found, suggesting that there is an amorphous phase in the deposits. Moreover, the coatings' XRD patterns show no crystalline peaks corresponding to the Co binder phase. The analysis of XRD pattern reveals that the W_2C/WC peak ratios of WC-1, WC-2, and WC-3 coatings are 15.58, 9.14, and 14.96%, respectively. According to Table 2, the spray parameters for all coatings were nearly the same; therefore, the powder's particle size is likely the reason why the levels of decarburization are different. In other words, the smaller the particle size is, the higher the temperature reached by the powder particles leading to the larger extent of WC decarburization. According to the aforementioned findings, one can conclude that the maximum carbon loss and W_2C/WC ratios of WC-1 coating (42% and 15.58%, respectively) are highly dependent on its smaller particle size ($32\ \mu m$), compared to WC-2 ($38\ \mu m$) and WC-3 ($34\ \mu m$). However, this trend is not observed when comparing WC-2 and WC-3 coatings. In comparison with WC-2 with the particle size, carbon loss, and W_2C/WC ratio of $38\ \mu m$, 30%, and 9.14%, respectively, WC-3 with the particle size of $34\ \mu m$ shows almost the same carbon loss (29%), but a higher W_2C/WC ratio (14.96%). This implies that at the same rate of carbon loss, the amount of W_2C phase varies depending on the WC particle size. Given the reduction of the size of WC from $0.9\ \mu m$ for WC-2 to $0.5\ \mu m$ for WC-3, W_2C/WC ratio increases from 9.14 to 14.96%. It can be suggested that at the same level of decarburization, smaller WC particles stimulate the formation of W_2C phase upon solidification by acting as more effective nucleation sites for W_2C precipitation than the larger WC particles. Fig. 7 illustrates the BSE images of cross-section of WC-1, WC-2, and WC-3 coatings.

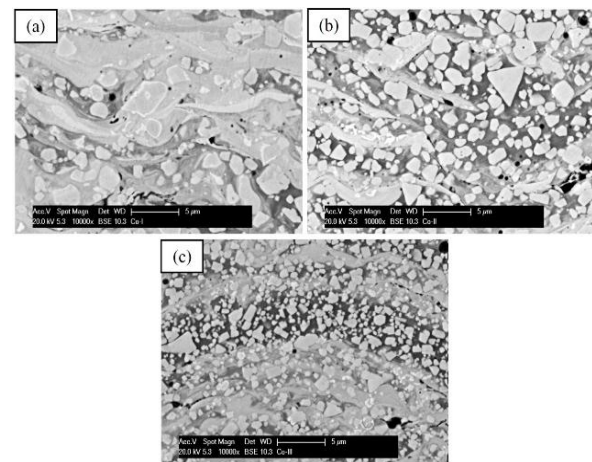


Figure 7. BSE images of cross-section of (a) WC-1, (b) WC-2, and (c) WC-3 coatings

The above images demonstrate splat-like microstructures of thermal spraying characterized by bright and dark contrast matrix layers that correspond to the areas containing higher and lower average atomic numbers, respectively. Angular WC particles are visible within the darker regions of all coatings, whereas WC particles are round in shape and are fully or partially enclosed by an irregular bright fringe identified as W_2C phase in the brighter areas [26,27]. Different dissolved W levels primarily give rise to different contrast levels of the matrices. Even though the size of the shells that cover WC particles prevents precise SEM/EDS, they clearly possess considerably lower carbon levels than the particle centers. Therefore, W_2C and W phases as identified by XRD are likely to be the shells that cover WC particles. As shown in Fig. 7a, the microstructure of WC-1 coatings is characterized by a large extent of amorphous (high tungsten) binder phase in which rounded WC particles mostly surrounded by W_2C phase are evident.

After that, WC-3 (Fig. 7c) coating reveals the highest level of amorphous binder phase with bright contrast in which smaller WC particles partly enclosed by W_2C are randomly distributed. As for WC-2 coatings, WC particles of angular morphology are distributed in a darker binder phase and more limited evidence of W_2C phase is observed than WC-1 and WC-3 coatings. This finding can be ascribed to the larger sizes of WC-2 particles (38 μm) that lead to their lower heating during spraying and, consequently, a lower W_2C/WC ratio (9.14%) than other coatings.

The metallographic technique of line analysis was employed to measure mean diameter of WC particles and volume fraction of the binder on the all coating cross-sections. Then, the following equation was used to measure the mean free path of the binder (λ) based on BSE images [28]:

$$\lambda = \frac{(1-f)}{N_L} \quad (2)$$

where N_L represents the number of discontinuous particles which are converged on a metallographic plane by a line of unit length and f is the volume fraction of the dispersed phase. In the case of every coating, the average of five measurements was reported. Table 5 presents the average volume fraction of binders, WC particle size, and mean free path of the binders for all coatings.

The results indicate that WC-1 coating is characterized by the lowest carbide phase amount and the highest mean free path value, while these values specific to WC-2 and WC-3 coatings are comparable. Table 6 presents WC particle size and carbide volume fraction of both powders and coatings.

It is obvious that the most significant change in volume fraction of carbide phase takes place during spraying of WC-1 (51%), while WC-2 by 18% exhibits the minimum change in the carbide phase volume fraction. Furthermore, the carbide particle size varied by -10%, 11% upon spraying of WC-1 and WC-2 coatings, whereas the changes in carbide particle size of WC-3 were negligible. The image analysis of BSE images of the coatings was taken into account to calculate their porosity. Figure 8 represents the typical images of the coating's cross-section followed by the coatings' porosity analysis.

TABLE 5. Volume fraction of carbide, WC particle size, and mean free path of the binders for WC-1, WC-2, and WC-3 coatings derived from line analysis method

Coating	Volume fraction of WC (%)	WC particle size (μm)	Mean free path (μm)
WC-1	35	~1.1	2.03
WC-2	55	~0.8	0.68
WC-3	49	~0.5	0.54

TABLE 6. Comparison of volume fractions and particle size of carbide in the powder and coating

Coating	Carbide phase volume fraction (%)			Size of carbide particle (μm)		
	Powder	Coating	Changes	Powder	Coating	Changes
WC-1	72	35	51 %	1.0	1.1	-10 %
WC-2	67	55	18 %	0.9	0.8	11 %
WC-3	71	49	33 %	0.5	0.5	0 %

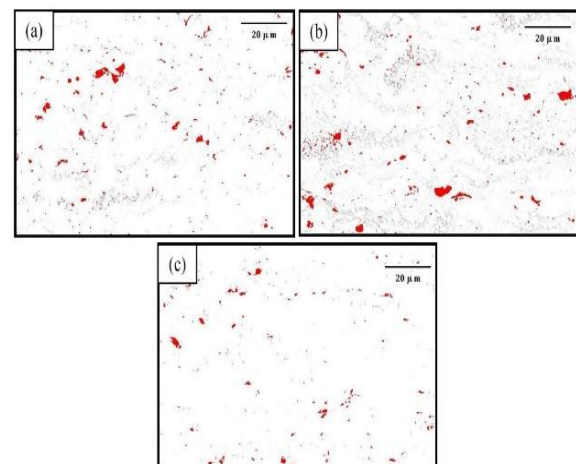


Figure 8. Image analysis performed on the cross-sectional BSE images of (a) WC-1, (b) WC-2, and (c) WC-3 coatings

Table 7 indicates the volume fraction of the porosity together with the average pore size of the coatings. According to the findings, the porosity levels of WC-1, WC-2, and WC-3 coatings are quite limited (< 1.8 vol%) due to the high degree of melting and uniform plastic flow of splats upon impact to the substrate. WC-1 and WC-3 coatings reveal the maximum and minimum average pore sizes of 0.27 and 0.42 μm , respectively.

TABLE 7. Porosity percentage and mean pore size measured by image analysis of the cross-sectional BSE images of the coatings

Coating	Average pore size (μm)	Porosity (vol %)
WC-1	0.27	1.6
WC-2	0.36	1.8
WC-3	0.42	1.2

3.2. MECHANICAL PROPERTISE OF THE COATINGS

The measured Vickers microhardness of WC-1, WC-2, and WC-3 coatings was 1418 ± 61 , 1306 ± 71 , and 1203 ± 57 kgf/mm^2 , respectively. While the hardness of WC-3 was found to be the lowest, that of WC-1 coating was the highest. The hardness of thermally sprayed WC cermet coatings is highly dependent on the following criteria: the volume fraction of retained hard WC phase, volume fraction of new phases (e.g., W_2C and W), hardness of the binder phase, and microstructural properties of the coating (i.e., porosity, mean free path of binder, and WC particle size). The retained carbide phase plays a key role in assessing the hardness of the thermally sprayed WC cermet coatings. In this respect, considerable attempts have been made to take control over the decomposition of the carbide phase during the spraying process. According to the relevant investigations, the hardness of WC cermet coatings increases through decreasing decomposition [29,30]. Usmani et al. [31] suggested that upon an increase in the W_2C content, the hardness of the coating decreased. The formation of a more brittle W_2C phase around the WC particles reduces the WC-matrix cohesion and, consequently, deteriorates the mechanical properties including hardness [32,33].

On the contrary, the larger the extent of WC decarburization during spraying is, the more enriched the binder phase in W and C will be. This happens due to the high solubility of these elements in the binder phase during rapid solidification [34]. Moreover, the hardness and brittleness of coatings are enhanced as a result of this enrichment. Although decarburization lessens the volume fraction of WC phase, its damaging impact on the hardness is compensated through

hardening the cobalt matrix during the dissolution process of W and C into the binder phase [35]. WC-1 coating owes its maximum hardness of 1418 ± 61 kgf/mm^2 to this enrichment. In fact, compared to WC-2 and WC-3 coatings, the highest decarburization (42%) and low WC fraction signify considerable enrichment of the binder phase in both W and C that guarantees an increase in the hardness.

Despite approximately the same decarburization degree of WC-2 and WC-3 coatings, their hardness is different from each other. According to the data given in Table 6, the volume fraction of carbide in WC-2 (55%) is higher than that of WC-3 (49%); however, the lower $\text{W}_2\text{C}/\text{WC}$ ratio in the former (9.14%) verifies more retained WC phase in the coating's microstructure. This is why WC-2 exhibits shows greater hardness than WC-3 coating. Evans and Wilshaw's Equation was used to calculate the coatings' fracture toughness through measuring the Vickers indentations under a vertical load of 5 kgf . For each coating, the measured fracture toughness ranged orderly from low toughness (long cracks) to high toughness (short cracks). In the light of this approach, Fig. 9a presents the cumulative distribution of fracture toughness for different coatings.

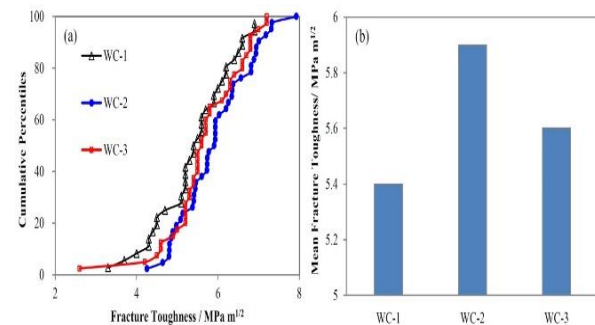


Figure 9. (a) Cumulative percentiles and (b) mean values of indentation fracture toughness for WC-1, WC-2, and WC-3 coatings

As shown in Fig. 9a, the cumulative percentile versus fracture toughness shows a very similar variation for different coatings. Fig. 9a confirms that WC-2 coating has the maximum mean fracture toughness of 5.9 $\text{MPa.m}^{1/2}$; WC-3 and WC-1 coatings show lower values of 5.6 and 5.4 $\text{MPa.m}^{1/2}$, respectively. The lower fracture toughness of WC-1 coating than that of other coatings results from the larger extent of decarburization (42%), amorphous binder phase formation (see Fig. 7a), and higher $\text{W}_2\text{C}/\text{WC}$ ratio (15.58%). It is well established that the amorphous W-rich binder phase, embrittled by WC dissolution, is the preferential path for crack propagation, thereby deteriorating the coatings' fracture toughness [36-38]. In addition, large amount of

W₂C phase precipitated in the vicinity of WC particles for WC-1 coating weakens the cohesion of WC-binder interface enabling the initiation and propagation of cracks on the coating [39]. Although WC-2 and WC-3 coatings undergo the same decarburization level, the lower W₂C/WC ratio in the former (9.14%) accounts for its greater fracture toughness.

3.3. THE COATINGS' ABRASIVE WEAR

The Dry Sand Rubber Wheel (DSRW) testing was implemented to calculate the coatings' abrasive wear by means of alumina 60 and silica 70 abrasives under four different loads of 19.6, 49, 98, and 127.5 N, respectively. The least squares fit of the data in the linear (steady state) regime determines the wear rate. Fig. 10 represents the rates of steady state wear with alumina 60 and silica 70 abrasives for each type of coating as a function of load.

WC-1 coating abraded by alumina 60 shows a marginal increase in wear rate from 0.0245 to 0.0417 mg.m⁻¹ as the applied load rises in the range of 19.6 to 127.5 N. A slightly higher wear rate with maximum amount of 0.054 mg.m⁻¹ was obtained for WC-2 coating abraded by alumina 60 under the load of 49 N. On the contrary, the wear rate of WC-3 coating, in comparison to WC-1 and WC-2 coatings, shows a significant increase from 0.0628 to 0.191 mg.m⁻¹ with the applied load ranging from 19.6 to 127.5 N, which suggests lower abrasive wear resistance against alumina 60.

The wear rate of WC-1 coating abraded by silica 70 particles increases in the range of 0.0091 to 0.0327 mg.m⁻¹ with an increase in the applied load from 19.6 to 98 N; this is followed by a drop in the wear rate to 0.0239 mg.m⁻¹ at the load of 127.5 N. The wear rate of WC-2 coating constantly increases from 0.0114 to 0.0449 with the applied load of up to 98 N, reaching a plateau with further load increase to 127.5 N. Finally, the wear rate of WC-3 coating shows an increasing linear trend ranging from 0.016 to 0.0415 mg.m⁻¹ with the applied load rising from 19.6 to 127.5 N. As shown in Fig. 10c, the wear rate of the coatings abraded by alumina 60 is ~1.2-7.8 times higher than that of coatings abraded by silica 70 almost over the whole range of the applied load. The wear rate is sensitive to the ratio of abrasive hardness H_a to the surface hardness H_s . Abrasion under $H_a/H_s > 1.2$ and $H_a/H_s < 1.2$ conditions can be termed as "hard abrasion" and "soft abrasion", respectively [40]. Fig. 11 illustrates the H_a/H_s values for each coating-abrasive combination. It is observed that the abrasive wear by silica 70 is located in the "soft" regime, while abrasion by alumina 60 imposes "hard" regime on all coatings.

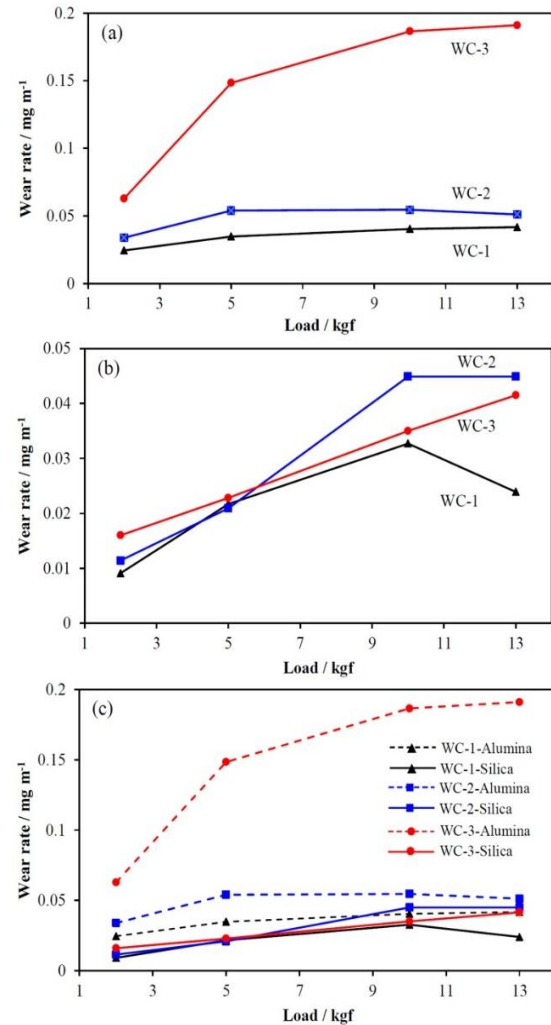


Figure 10. Plots indicating wear rates of WC-1, WC-2, and WC-3 coatings abraded by (a) alumina 60 and (b) silica 70 under different loads; (c) Comparison of the wear rates of the coatings abraded by alumina 60 and silica 70

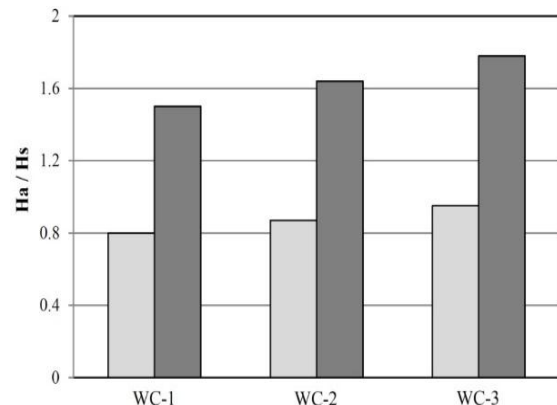


Figure 11. A plot indicating transition between "hard" and "soft" abrasive wear mechanisms ($H_a/H_s = 1.2$) for the coatings abraded by silica 70 and alumina 60

Following wear testing, the central zone of the worn surfaces abraded under minimum and maximum applied loads was examined by SEM. Fig. 12 a,b shows the plan-view SEM images of WC-1 coating abraded by alumina 60 under the loads of 19.6 and 127.5 N, respectively. In both cases, two areas with high and low densities of carbides are apparently separated. Moreover, the wear track formed at the applied load of 19.6 N shows evidence of grooving, carbide cracking and voids; the latter is caused by carbide pull-out. These features become more notable at the load of 197.5 N, leading to the formation of some small pits. The carbide cracking and pull-out are also obvious in the cross-sectional view of WC-1 worn surface (Fig. 12c), while no evidence of subsurface cracking can be observed. Fig. 12 d,e illustrates the plan-view images of wear scar of WC-1 coating after abrasion with silica 70 under the minimum (19.6 N) and maximum (127.5 N) applied loads. The worn surfaces appearing at both loads suggest that the matrix is removed at a higher rate, leaving the exposed carbide particles as well as carbide cracking and pull-out that are of significance at higher loads. Although the cross-sectional SEM image taken at the highest load (Fig. 12f) reveals no significant subsurface cracking, it indicates that the carbide particles are standing proud of the matrix signifying the preferential wear of the matrix phase.

Fig. 13 a,b shows the SEM images of the WC-2 coating after abrasion with alumina 60 at the loads of 19.6 and 127.5 N, respectively. Carbide pull-out voids and a number of furrows are detected after the matrix removal. Cracked carbides and higher density of voids are observed at higher loads. While no subsurface cracking takes place during abrasion testing of WC-2 by alumina 60, the cross-section of the worn surface (Fig. 13c) confirms WC pull-out and cracking. Plan-view SEM images of wear scars of WC-2 coating after abrasion with silica 70 at the minimum (19.6 N) and maximum (127.5 N) applied loads are presented in Fig. 13 d,e. These wear scars are characterized by three different criteria: 1) regions densely occupied by carbide particles, 2) regions less occupied by carbide particles, and 3) dark regions appearing as carbide pull-out voids. At higher loads (Fig. 13e), some carbides' cracking and a number of furrows are observed as a result of matrix removal. The matrix removal, by itself, results in leaving the carbides unprotected and making them more susceptible to pull-out mechanism during abrasion. Cross-sectional SEM image of worn surface of WC-2 coating abraded by silica 70 (Fig. 13f) shows no subsurface cracks.

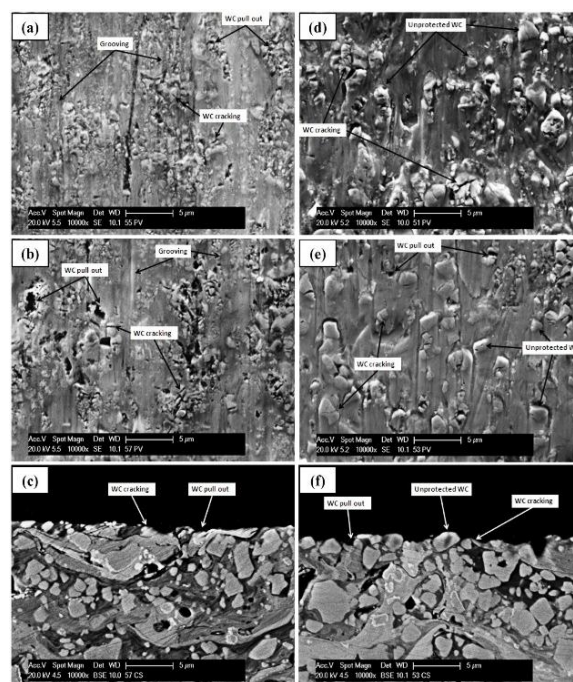


Figure 12. Plan-view SEM images of wear scar of WC-1 coating abraded by (a,b) alumina 60 and (d,e) silica 70 at the loads of 19.6 and 127.5 N, respectively. Cross-sectional SEM images of wear scar of WC-1 coating abraded by (c) alumina 60 and (f) silica 70 at the load of 127.5 N

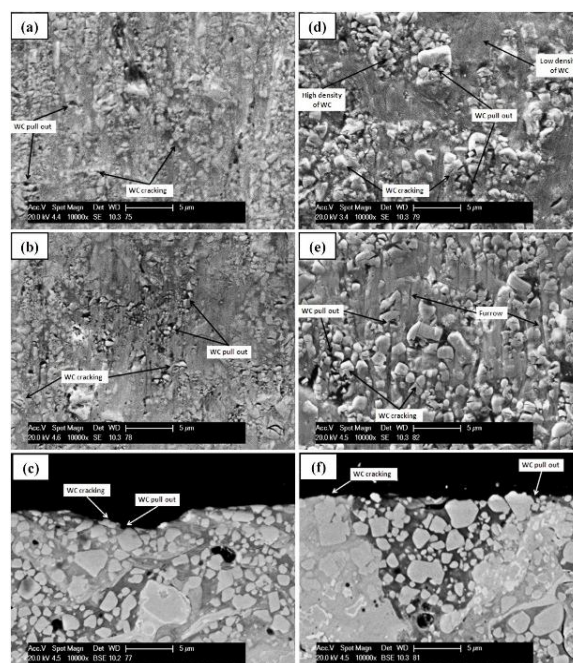


Figure 13. Plan-view SEM images of wear scar of WC-2 coating abraded by (a,b) alumina 60 and (d,e) silica 70 under 19.6 and 127.5 N, respectively. Cross-sectional SEM images of wear scar of WC-2 coating abraded by (c) alumina 60 and (f) silica 70 under 127.5 N

Fig. 14 a,b demonstrates SEM images of the WC-3 coating after abrasion by alumina 60 at minimum (19.6 N) and maximum (127.5 N) applied loads. Two different regions having high and low densities of carbides are evident at both loads. In addition, under 19.6 N load (Fig. 14a), many scratches and some narrow grooves in different directions can be detected, while at the highest applied load (Fig. 14b), wide and deep grooves along the direction of sliding flow are visible. The cross-sectional image of the worn surface under the highest load (Fig. 14c) presents sub-surface cracking with cracks running through the bright binder phase region. Fig. 14.d,e shows images of the central zone of the wear scar on WC-3 coating followed by abrasion with silica 70 at the lowest (19.6 N) and the highest (127.5 N) applied loads, respectively. The wear scars comprise areas with high and low densities of carbides accompanied by a small number of voids caused by carbide pull-out. Further, a number of furrows on the sides of carbide particles because of the removal of matrix at higher rates are visible. The worn surface cross-section after wear at the highest load (Fig. 14f) reveals sub-surface cracks propagating through the bright binder phase. Further, unshielded carbide particles due to preferential wear of the binder phase are apparent on the surface.

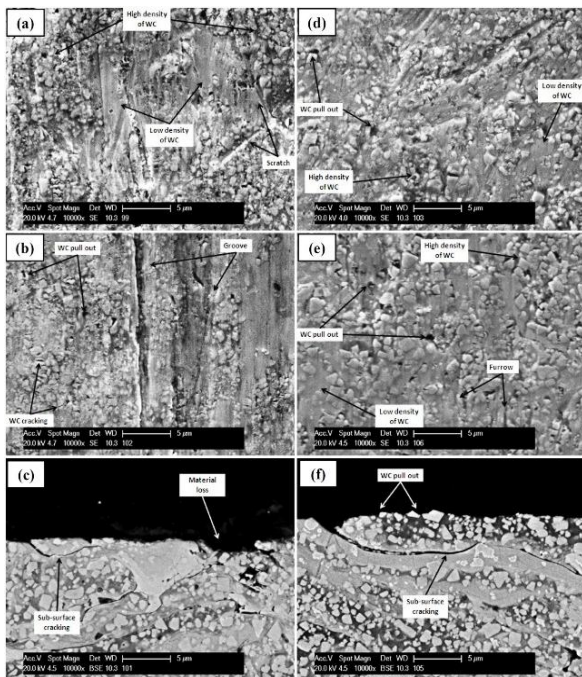


Figure 14. SEM images of wear scar of WC-3 coating abraded by (a,b) alumina 60 and (d,e) silica 70 under 19.6 and 127.5 N, respectively. Cross-sectional SEM images of wear scar of WC-3 coating abraded by (c) alumina 60 and (f) silica 70 under 127.5 N

4. DISCUSSION

4.1. WEAR MEASUREMENTS

The abrasive wear rate of the coatings generally increases with the applied load during abrasion by both alumina 60 and silica 70 (see Fig. 10). However, there are several exceptions for WC-2 abraded by alumina 60 and for WC-1 and WC-2 abraded by silica 70 so that with increasing the applied load to 127.5 N load, the wear rate reveals either unchanged or lower values. This arises from the fact that in DSRW test, the temperature of both sample and wheel increases, the degree of which under a given test parameter depends on abrasive type, sample materials, and applied load [41]. Increasing the rubber temperature as a result of higher load leads to its lower hardness; accordingly, the wear rate decreases in some cases as the applied load increases to 127.5 N [42]. The ratio of abrasive particle hardness to coating hardness shows that for all coatings, the abrasive wear by alumina is “harder” than that by silica which is “soft” (Fig. 11). For all the coatings and test conditions examined, the wear rate by silica 70 particles is significantly lower than that by alumina 60. The worn surface examination verifies that almost in all cases, silica 70 abrasive shows evidence of the preferential cobalt matrix abrasion followed by carbide cracking and pull-out, while alumina abrasive imposes more severe carbide cracking and pull-out together with grooving along the direction of abrasive flow. Increasing the applied load facilitates the formation of deeper grooves. Further, pieces of evidence of subsurface cracking are observed for WC-3 coating abraded by both silica 70 and alumina 60 abrasives. The angular morphology and higher hardness of alumina than those of more rounded silica particles result in significant differences in wear behavior of the coatings.

Fig. 15 displays the wear rate of WC-1, WC-2, and WC-3 coatings as a function of the coating hardness.

The results confirm that the wear rate of the coatings abraded by silica 70 does not necessarily decrease with increasing the coatings’ hardness; for instance, WC-2 coating abraded by silica 60 under 98 and 127.5 N shows a higher rate of wear than WC-3 coating, although the former is subject to higher hardness. This originates from the complicated mechanism of abrasive wear in thermally sprayed cermet coatings and importance of parameters other than coatings hardness, e.g., type of abrasive, fracture toughness of the coatings, applied load during DSRW testing, etc.

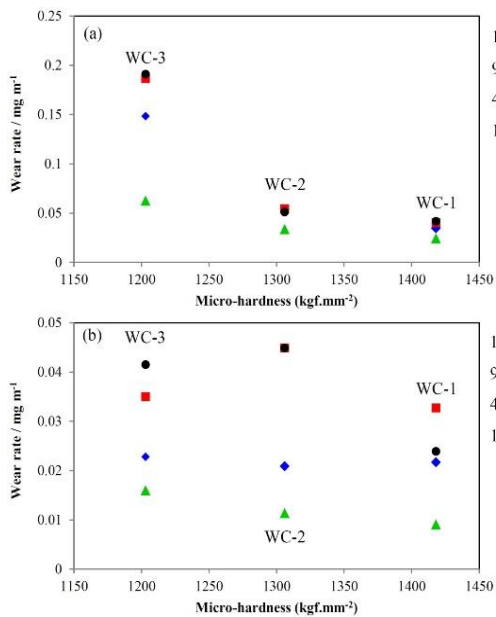


Figure 15. Wear rate versus microhardness plots of WC-1, WC-2, and WC-3 coatings abraded by (a) alumina 60 and (b) silica 70 abrasives

4.2. ABRASIVE WEAR WITH ALUMINA

The hardness of alumina 60 particles (2103 ± 25 kgf.mm⁻²) is higher than that of all the three coatings examined. These abrasive particles exhibit an angular morphology and a narrow size range (Fig. 2b). Moreover, as plotted in Fig. 11, the ratios of abrasive hardness (H_a) to the hardness of the coatings' surface (H_s) for all coatings are higher than 1.2, demonstrating the role of "hard wear" mechanism. These conditions are conducive to plastic deformation that occurs mostly by plastic ploughing, cutting followed by some local associated fracture in the more brittle cermet coatings [43].

The worn surfaces produced by alumina abrasive show indications of grooving, pitting, and cutting of the coatings' surface. Based on cross-sectional examinations, abrasive wear of WC-3 coating is accompanied by subsurface cracking.

These results show that the two main wear mechanisms, namely plastic deformation and fracture, play a role in material removal. The passage of hard and sharp abrasive facilitates plastic deformation of the surface, leading to the formation of grooves with materials piling up at the groove's edges at the first stage. At the second stage, due to the preferential elimination of the cobalt binder phase, the support is no longer present for carbide particles, leaving them unshielded against the collision of abrasives and leading to both carbides fracture and their pull-out from matrix during abrasive wear. The comparison of the wear rates of the three coatings

indicate the highest, medium, and the lowest abrasion resistance rates of WC-1, WC-2, and WC-3 coatings. Considering that the difference in fracture toughness of the coatings is inconsiderable (varying between 5.4-5.9 MPa.m^{1/2} as shown in Fig. 9), it is proposed that the overall hardness of the coatings controls the rate of abrasion by alumina 60; in other words, the higher the coating's hardness, the higher the resistance against alumina 60 abrasive particles. As for WC-3 coating, besides carbides fracture and pull-out, subsurface cracking caused by fatigue of the surface layers leads to the spallation type of failure (see Fig. 14c). As a result, the high-level removal of materials takes place for WC-3 coating resulting in the higher wear rate than the wear rate of WC-1 and WC-2 coatings abraded in the same conditions.

4.3. ABRASIVE WEAR WITH SILICA

The hardness of silica 70 particles (1116 kgf.mm⁻²) is lower than that of all three coatings examined. These abrasives are characterized by a round morphology and a narrow size range (Fig. 2a). Abrasive hardness (H_a) to the hardness of coatings' surface (H_s) ratio of all coatings is lower than 1.2 indicating "soft wear" regime and, as such, particle blunting is likely to occur during abrasion resulting in a lower wear rate under a three-body (rolling) abrasion mechanism than the wear rate of harder alumina 60 abrasive particles. As proposed in Ref [44], the removal of selective binder phase from the near-surface layers is a significant step in the wear process of cermet materials by soft abrasives. Cyclic indenting contact of abrasive particles during a three-body abrasion process leads to compressive stresses on the coatings' surface. Therefore, the binder is initially compressed out of the surface ahead of and to the sides of the indenter. The next stage is damage to carbide particles located in the heavily loaded regions in which the binder phase has plastically flowed. Hence, carbide particles are exposed to fracture into small fragments and are gradually pulled off the surface.

Cross-sectional examination of WC-3 worn surface abraded by silica 70 (Fig. 14f) confirms that sub-surface cracks mostly propagate through W-rich binder phase of this coating, while no significant evidence of this type of cracking can be observed for WC-1 and WC-2 coatings. Elastic-plastic indentation of the abrasive, facilitating the formation of sub-surface crack close to the WC-3 coating's surface, leads to the detachment of the surface material [45].

As illustrated based on the SEM images of wear scars on all coatings, it can be seen that the metal matrix is abraded at a higher rate, leaving carbides unprotected on the surface. For all coatings, removal of matrix is more pronounced at higher applied loads with micro-grooves being formed by the sides of the carbide particles and,

also, a number of fragmented carbide particles and voids due to the pulling out of the carbides.

A comparison of the wear rates of WC-1, WC-2, and WC-3 coatings shows a similar trend until high applied loads (98 and 127.5 N) are reached. WC-1 with the largest carbide particles and the lowest WC volume fraction (owing to the high degree of decomposition during spray process) shows maximum resistance against silica 70 abrasive, probably because of its higher overall hardness than other coatings. The high hardness of thermally sprayed composite carbide with relatively low carbide content results from the high hardness of the brittle amorphous phase formed after spraying. The higher hardness of the binder phase in an abrasion wear test makes its preferential wear quite limited, leading to a reduction in the wear rate [46,47].

5. CONCLUSIONS

- 1) The highest carbon loss was measured for WC-1 (42%), while lower values of 30% and 29% were obtained for WC-2 and WC-3 coatings, respectively.
- 2) The Vickers microhardness of WC-1, WC-2, and WC-3 coatings was calculated as 1418 ± 61 , 1306 ± 71 , and 1203 ± 57 kgf/mm², respectively.
- 3) WC-2 coating had the maximum fracture toughness of 5.9 MPa.m^{1/2}, after which WC-3 and WC-1 coatings showed lower values of 5.6 and 5.4 MPa.m^{1/2}, respectively.
- 4) The wear rate of the coatings abraded by alumina 60 was ~1.2-7.8 times higher than that of the coatings abraded by silica 70 almost over the whole range of applied loads (19.6-127.5 N).
- 5) The wear rate of WC-3 coating showed a significant increase from 0.0628 to 0.191 mg.m⁻¹ with the applied load ranging from 19.6 to 127.5 N, which demonstrated its lower abrasive wear resistance against alumina 60 than WC-1 and WC-2 coatings.

6. ACKNOWLEDGEMENTS

The author sincerely appreciates Professors Philip Shipway and Graham McCartney from Department of Mechanical, Materials, and Manufacturing Engineering, The University of Nottingham, UK, for their supervision, advice and encouragement throughout this research.

REFERENCES

1. Lim, N. S., Das, S., Park, S. Y., Kim, M. C., Park, C. G., "Fabrication and microstructural characterization of nanostructured WC/Co coatings", *Surface and Coatings Technology*, Vol. 205, No. 2, (2010), 430-435. <https://doi.org/10.1016/j.surfcoat.2010.07.004>

2. Jia, C., Sun, L., Tang, H., Qu, X., "Hot pressing of nanometer WC-Co powder", *International Journal of Refractory Metals and Hard Materials*, Vol. 25, No. 1, (2007), 53-56. <https://doi.org/10.1016/j.ijrmhm.2005.11.003>
3. Kim, H. C., Shon, I. J., Yoon, J. K., Doh, J. M., "Consolidation of ultrafine WC and WC-Co hard materials by pulsed current activated sintering and its mechanical properties", *International Journal of Refractory Metals and Hard Materials*, Vol. 25, No. 1, (2007), 46-52. <https://doi.org/10.1016/j.ijrmhm.2005.11.004>
4. Bonache, V., Rayón, E., Salvador, M. D., Busquets, D., "Nanoindentation study of WC-12Co hard metals obtained from nanocrystalline powders: Evaluation of hardness and modulus on individual phases", *Materials Science and Engineering: A*, Vol. 527, No. 12, (2010), 2935-2941. <https://doi.org/10.1016/j.msea.2010.01.026>
5. Li, C. J., Yang, G. J., "Relationships between feedstock structure, particle parameter, coating deposition, microstructure and properties for thermally sprayed conventional and nanostructured WC-Co", *International Journal of Refractory Metals and Hard Materials*, Vol. 39, (2013), 2-17. <https://doi.org/10.1016/j.ijrmhm.2012.03.014>
6. Mateen, A., Saha, G. C., Khan, T. I., Khalid, F. A., "Tribological behaviour of HVOF sprayed near-nanostructured and microstructured WC-17wt.% Co coatings", *Surface and Coatings Technology*, Vol. 206, (2011), 1077-1084. <https://doi.org/10.1016/j.surfcoat.2011.07.075>
7. Saha, G. C., Khan, T. I., "The corrosion and wear performance of microcrystalline WC-10Co-4Cr and near-nanocrystalline WC-17Co high velocity oxy-fuel sprayed coatings on steel substrate", *Metallurgical and Materials Transactions A*, Vol. 41, No. 11, (2010), 3000-3009. <https://doi.org/10.1007/s11661-010-0296-1>
8. Chivavibul, P., Watanabe, M., Kuroda, S., Shinoda, K., "Effects of carbide size and Co content on the microstructure and mechanical properties of HVOF-sprayed WC-Co coatings", *Surface and Coatings Technology*, Vol. 202, No. 3, (2007), 509-521. <https://doi.org/10.1016/j.surfcoat.2007.06.026>
9. Ghadami, F., Ghadami, S. and Abdollah-Pour, H., "Structural and oxidation behavior of atmospheric heat treated plasma sprayed WC-Co coatings", *Vacuum*, Vol. 94, (2013), 64-68. <https://doi.org/10.1016/j.vacuum.2013.01.019>
10. Aristizabal, M., Sanchez, J. M., Rodriguez, N., Ibarreta, F., Martinez, R., "Comparison of the oxidation behaviour of WC-Co and WC-Ni-Co-Cr cemented carbides", *Corrosion Science*, Vol. 53, No. 9, (2011), 2754-2760. <https://doi.org/10.1016/j.corsci.2011.05.006>
11. Zhu, Q., Zhu, H. T., Tieu, A. K., Reid, M., Zhang, L. C., "In-situ investigation of oxidation behaviour in high-speed steel roll material under dry and humid atmospheres", *Corrosion Science*, Vol. 52, No. 8, (2010), 2707-2715. <https://doi.org/10.1016/j.corsci.2010.04.027>
12. Qiao, Y., Fischer, T. E., Dent, A., "The effects of fuel chemistry and feedstock powder structure on the mechanical and tribological properties of HVOF thermal-sprayed WC-Co coatings with very fine structures", *Surface and Coatings Technology*, Vol. 172, No. 1, (2003), 24-41. [https://doi.org/10.1016/S0257-8972\(03\)00242-1](https://doi.org/10.1016/S0257-8972(03)00242-1)
13. Zhao, H., Ding, Z., Zhang, Y., Wang, Q., "Properties of Nanostructured WC-12Co Coatings Sprayed by HVOF", In *Thermal Spray 2007: Global Coating Solutions (ASM International)*, (2007), 884-889.

14. Schroeder, S., Melnyk, C., Grant, D., Gansert, R., Saha, G., Glenesk, L., "Properties of Powders, Coatings and Consolidated Components Produced from Nano-and Near-Nano Crystalline Powders", *Thermal Spray 2009: Expanding Thermal Spray Performance to New Markets and Applications*, Marple, B. R., Hyland, M. M., Lau, Y. -C., Li, C. -J., Lima, R. S., Montavon, G., Eds., ASM International, Materials Park, OH., USA, (2009), 403-408. <https://doi.org/10.1361/cp2009itsc0403>
15. Cho, T. Y., Yoon, J. H., Kim, K. S., Song, K. O., Joo, Y. K., Fang, W., Zhang, S. H., Youn, S. J., Chun H. G., Hwang, S. Y., "A Study on HVOF Coatings of Micron and Nano WC-Co Powders", *Surface and Coatings Technology*, Vol. 202, No. 22-23, (2008), 5556-5559. <https://doi.org/10.1016/j.surfcoat.2008.06.106>
16. Stewart, D. A., Shipway, P. H., McCartney, D. G., "Abrasive wear behaviour of conventional and nanocomposite HVOF-sprayed WC-Co coatings", *Wear*, Vol. 225-229, (1999), 789-798. [https://doi.org/10.1016/S0043-1648\(99\)00032-0](https://doi.org/10.1016/S0043-1648(99)00032-0)
17. Guilemany, J. M., Dosta, S., Miguel, J. R., "The enhancement of the properties of WC-Co HVOF coatings through the use of nanostructured and microstructured feedstock powders", *Surface and Coatings Technology*, Vol. 201, No. 3-4, (2006), 1180-1190. <https://doi.org/10.1016/j.surfcoat.2006.01.041>
18. Baik, K. H., Kim, J. H., Seong, B. G., "Improvements in hardness and wear resistance of thermally sprayed WC-Co nanocomposite coatings", *Materials Science and Engineering: A*, Vol. 449-451, (2007), 846-849. <https://doi.org/10.1016/j.msea.2006.02.295>
19. Moore, M. A., "Abrasive Wear", in *Treatise on Materials Science and Technology*, Scott, D., Ed., Academic Press: New York, NY, USA, (1979), p. 217-257.
20. Hewitt, S. A., Kibble, K. A., "Effects of ball milling time on the synthesis and consolidation of nanostructured WC-Co composites", *International Journal of Refractory Metals and Hard Materials*, Vol. 27, No. 6, (2009), 937-948. <https://doi.org/10.1016/j.ijrmhm.2009.05.006>
21. Pang, C., Guo, Z., Luo, J., Hou, T., Bing, J., "Effect of vanadium on synthesis of WC nanopowders by thermal processing of V-doped tungsten precursor", *International Journal of Refractory Metals and Hard Materials*, Vol. 28, No. 3, (2010), 394-398. <https://doi.org/10.1016/j.ijrmhm.2009.12.006>
22. Blau, P. J., *ASM Handbook, Volume 18-Friction, Lubrication, and Wear Technology*, ASM International, (1992).
23. Park, S. Y., Kim, M. C., Park, C. G., "Mechanical properties and microstructure evolution of the nano WC-Co coatings fabricated by detonation gun spraying with post heat treatment", *Materials Science and Engineering: A*, Vol. 449-451, (2007), 894-897. <https://doi.org/10.1016/j.msea.2006.02.444>
24. Guilemany, J. M., De Paco, J. M., Miguel, J. R., Nutting, J., "Characterization of the W₂C phase formed during the high velocity oxygen fuel spraying of a WC+12 Pct Co powder", *Metallurgical and Materials Transactions A*, Vol. 30, No. 8, (1999), 1913-1921. <https://doi.org/10.1007/s11661-999-0002-3>
25. Wood, R. J., "Tribology of thermal sprayed WC-Co coatings", *International Journal of Refractory Metals and Hard Materials*, Vol. 28, No. 1, (2010), 82-94. <https://doi.org/10.1016/j.ijrmhm.2009.07.011>
26. Watanabe, M., Owada, A., Kuroda, S., Gotoh Y., "Effect of WC size on interface fracture toughness of WC-Co HVOF sprayed coatings", *Surface and Coatings Technology*, Vol. 201, No. 3-4, (2006), 619-627. <https://doi.org/10.1016/j.surfcoat.2005.12.019>
27. Kear, B. H., Skandan, G., Sadangi, R. K., "Factors controlling decarburization in HVOF sprayed nano-WC/Co hard coatings", *Scripta Materialia*, Vol. 44, No. 8-9, (2001), 1703-1707. [https://doi.org/10.1016/S1359-6462\(01\)00867-3](https://doi.org/10.1016/S1359-6462(01)00867-3)
28. Fullman, R. L., "Measurement of Particle Sizes in Opaque Bodies", *JOM-Journal of the Minerals, Metals and Materials Society*, Vol. 5, No. 3, (1953), 447-452. <https://doi.org/10.1007/BF03398971>
29. Di Girolamo, G., Pilloni, L., Pulci, G., Marra, F., "Tribological Characterization of WC-Co Plasma Sprayed Coatings", *Journal of the American Ceramic Society*, Vol. 92, No. 5, (2009), 1118-1124. <https://doi.org/10.1111/j.1551-2916.2009.03023.x>
30. Sánchez, E., Bannier, E., Salvador, M. D., Bonache, V., García, J. C., Morgiel, J., Grzonka, J., "Microstructure and Wear Behavior of Conventional and Nanostructured Plasma-Sprayed WC-Co Coatings", *Journal of Thermal Spray Technology*, Vol. 19, No. 5, (2010), 964-974. <https://doi.org/10.1007/s11666-010-9480-5>
31. Usmani, S., Sampath, S., Houck, D. L., Lee, D., "Effect of carbide particle size on the sliding and abrasive wear behavior of thermally sprayed WC-Co coatings", *Tribology Transactions*, Vol. 40, No. 3, (1997), 470-478.
32. Sudaprasert, T., Shipway, P. H., McCartney, D. G., "Sliding wear behavior of HVOF sprayed WC-Co coatings deposited with both gas-fuelled and liquid-fuelled systems", *Wear*, Vol. 255, No. 7-12, (2003), 943-949. [https://doi.org/10.1016/S0043-1648\(03\)00293-x](https://doi.org/10.1016/S0043-1648(03)00293-x)
33. Picas, J. A., Punset, M., Baile, M. T., Martin, E., Forn, A., "Properties of WC-CoCr Based Coatings Deposited by Different HVOF Thermal Spray Processes", *Plasma Processes and Polymers*, Vol. 6, No. S1, (2009), S948-S953. <https://doi.org/10.1002/ppap.200932402>
34. Shaw, K. G., Gruninger, M. F., Jarosinski, W. J., "High temperature intermetallic binders for HVOF carbides", In *1994 Thermal Spray Industrial Applications: Proceedings*, (1994).
35. Schwetzke, R., Kreye, H., "Microstructure and properties of tungsten carbide coatings sprayed with various high-velocity oxygen fuel spray systems", *Journal of Thermal Spray Technology*, Vol. 8, No. 3, (1999), 433-439. <https://doi.org/10.1361/105996399770350395>
36. Stewart, D. A., Shipway, P. H., McCartney, D. G., "Microstructural evolution in thermally sprayed WC-Co coatings: comparison between nanocomposite and conventional starting powders", *Acta Materialia*, Vol. 48, No. 7, (2000), 1593-1604. [https://doi.org/10.1016/S1359-6454\(99\)00440-1](https://doi.org/10.1016/S1359-6454(99)00440-1)
37. Ban, Z. G., Shaw, L. L., "Characterization of thermal sprayed nanostructured WC-Co coatings derived from nanocrystalline WC-18wt.% Co powders", *Journal of Thermal Spray Technology*, Vol. 12, No. 1, (2003), 112-119. <https://doi.org/10.1361/105996303770348564>
38. Ishikawa, Y., Kuroda, S., Kawakita, J., Sakamoto, Y., Takaya, M., "Sliding Wear Properties of HVOF Sprayed WC-20% Cr3C2-7% Ni Cermet Coatings", *Surface and Coatings Technology*, Vol. 201, No. 8, (2007), 4718-4727. <https://doi.org/10.1016/j.surfcoat.2006.10.007>
39. Rodriguez, M., Klisans, J., Bavaresco, L., Scagni, A., Arenas, F., "Wear resistance of HVOF sprayed carbide coatings", In *Thermal Spray 2001: New Surfaces for a New Millennium, Proceedings, International Thermal Spray Conference (ITSC 2001)*, Singapore, 28-30 May, (2001), 1061-1068.
40. Hutchings, I. M., "Tribology: Friction and Wear Engineering Materials", Ed. Edward Arnold, a Division of Hodder Headline PLC., (1992), 273.

41. Nahvi, S. M., Shipway, P. H., McCartney, D. G., "Particle motion and modes of wear in the dry sand-rubber wheel abrasion test", *Wear*, Vol. 267, No. 11, (2009), 2083-2091. <https://doi.org/10.1016/j.wear.2009.08.013>
42. Stevenson, A. N. J., Hutchings, I. M., "Development of the dry sand rubber wheel abrasion test", *Wear*, Vol. 195, No. 1-2, (1996), 232-240. [https://doi.org/10.1016/0043-1648\(96\)06965-7](https://doi.org/10.1016/0043-1648(96)06965-7)
43. Tylczak, J. H., Hawk, J. A., Wilson, R. D., "A comparison of laboratory abrasion and field wear results", *Wear*, Vol. 225-229, No. 2, (1999), 1059-1069. [https://doi.org/10.1016/S0043-1648\(99\)00043-5](https://doi.org/10.1016/S0043-1648(99)00043-5)
44. Blombery, R. I., Perrot, C. M., Robinson, P. M., "Abrasive wear of tungsten carbide-cobalt composites. I. Wear mechanisms", *Materials Science and Engineering*, Vol. 13, No. 2, (1974), 93-100. [https://doi.org/10.1016/0025-5416\(74\)90176-1](https://doi.org/10.1016/0025-5416(74)90176-1)
45. Chen, H., Xu, C., Zhou, Q., Hutchings, I. M., Shipway, P. H., Liu, J., "Micro-scale abrasive wear behaviour of HVOF sprayed and laser-remelted conventional and nanostructured WC-Co coatings", *Wear*, Vol. 258, No. 1-4, (2005), 333-338. <https://doi.org/10.1016/j.wear.2004.09.044>
46. Lee, H. C., Gurland, J., "Hardness and deformation of cemented tungsten carbide", *Materials Science and Engineering*, Vol. 33, No. 1, (1978), 125-133. [https://doi.org/10.1016/0025-5416\(78\)90163-5](https://doi.org/10.1016/0025-5416(78)90163-5)
47. Nahvi, S. M., "Investigating the Abrasive Wear Resistance of Thermal-Sprayed WC-Based Coatings", *Advanced Ceramics Progress*, Vol. 6, No. 2, (2020), 7-16. <https://doi.org/10.30501/ACP.2020.107360>



The Effect of TiC Additive with Al₂O₃-Y₂O₃ on the Microstructure and Mechanical Properties of SiC Matrix Composites

M. Khodaei^{a*}, O. Yaghubizadeh^b, S. A. Safavi^a, N. Ehsani^a, H. R. Baharvandi^a, S. Esmaeeli^b

^a Composite Materials & Technology Center, Malek Ashtar University of Technology, Tehran, Iran

^b Department of Materials Science and Engineering, Faculty of Technology and Engineering, Imam Khomeini International University (IKIU), Qazvin, Iran

^c Department of Ceramic, Shahreza Branch, Islamic Azad University, Shahreza, Iran

PAPER INFO

Paper history:

Received 23 April 2020
Accepted in revised form 20 June 2020

Keywords:

Pressureless Sintering
SiC-TiC
Liquid-Phase Sintering
Toughness Mechanisms
Mechanical Properties

ABSTRACT

In this research, the SiC-matrix composite with different amounts of TiC (0, 2.5, 5, 7.5, and 10 wt%) supplemented with additives including 4.3 wt% Al₂O₃ and 5.7 wt% Y₂O₃ were utilized to initiate the required liquid phase. The sintering process was performed using pressureless sintering at 1900 °C for 1.5 hours under argon atmosphere. The composition and microstructure of the obtained composites were analyzed using X-Ray Diffraction (XRD), Field Emission Scanning Electron Microscope (FESEM), and Energy-Dispersive X-ray Spectroscopy (EDX). The results showed that TiC additives improved the densification of samples and impeded the growth of SiC grains. According to the phase analysis, the SiC was the main phase, while the TiC and YAG were characterized as partial phases. Additionally, due to the reaction of TiC and Al₂O₃, the composition of the liquid phase contained YAG and YAM. Assessments revealed that the microstructure and the final properties of composites were affected by density, produced phases and their distribution in the matrix, and grain size. According to the results, upon increasing the TiC up to 5 wt%, all the measured properties including density, hardness, elastic modulus, and fracture toughness improved and reached 97.40%, 26.73 GPa, 392 GPa, and 5.80 MPa.m^{1/2}, respectively. However, with increasing the additives to more than 5 wt%, these properties deteriorated. Microscopic evaluations revealed that crack deflection and crack bridging mechanisms contributed to the fracture toughness of SiC ceramics.

1. INTRODUCTION

Due to high thermal conductivity, low thermal expansion coefficient, and stability of mechanical strength up to 1400-1500 °C, silicon carbide (SiC) can readily tolerate thermal cycles at elevated temperatures [1-7]. The SiC is resistant to thermal shocks [8-11]. In addition, using SiC ceramics is 10 to 50% more energy-efficient than metallic superalloys [11]. Silicon carbide is a hard material (17-25 GPa) with Young's modulus of 400-450 GPa [8,11]. The chemical reactivity of SiC is low at room temperature, which is regarded as one of its inherent chemical properties [8].

Given the mentioned characteristics, SiC ceramics are utilized in industrial heat exchangers, steam and gas turbines, glass industry, metallurgical industries, ceramic

industry, nuclear and thermal power stations, and aeronautical constructions [12-14].

Despite these desirable characteristics, there are also other undesirable ones including low fracture toughness which not only limit the use of SiC in the industry but also encourage scientists to solve this weakness [8,11]. Some researchers argue that reinforcing the structure of SiC ceramics is the best solution to this flaw [15,16].

SiC-matrix composites are manufactured in different ways [8]. Among them, pressureless sintering is the most significant one since it provides the possibility of producing large pieces or complicated shapes [11,13].

In order to reach over 95% of the theoretical density, the methods of solid-state and liquid-state pressureless sintering were employed [17-20]. Liquid-state sintering yields superior mechanical properties to those produced

* Corresponding Author Email: mahdi.khodaei01@gmail.com (M. Khodaei)

by solid-state sintering for the SiC, increasing the employment of liquid-state sintering [11, 20].

The presence of the liquid phase produces improved homogeneity and mechanical properties, especially fracture toughness [20-23]. Liquid-phase sintering depends on the composition of base materials and liquid-phase additives [8,11]. In this respect, the most common additives are Al₂O₃-Y₂O₃ [12,19], Al₂O₃-Yb₂O₃ [10], Al₂O₃-La₂O₃ [24], Al₂O₃-Dy₂O₃ [10], and (SiC-AYC) Al₂O₃-Y₂O₃-CaO [11]. Among these additives, Al₂O₃ and Y₂O₃ have been studied more than others because they can react with SiO₂ which exists on the surface of SiC powders, thereby enhancing sinterability [20,26]. Moreover, it has been proved that adding oxides, carbides, nitrides, and borides such as TiO₂, B₄C, TiB₂, and ZrB₂ as the secondary phase or reinforcement improves the fracture toughness of SiC ceramics [20].

The related pieces of research have shown that employing TiC particles increases the sinterability of SiC ceramics [8]. Such particles impede the growth of matrix grains and improve the mechanical properties [27]. Further, the existence of TiC particles on the path of crack growth increases fracture energy [8,20] and generates subgrains and microcracks; in addition, the mismatch between the thermal expansions of TiC and SiC plays a significant role in improving the properties [8].

The present study investigates the effect of different amounts of TiC (0, 2.5, 5, 7.5, and 10 wt%) on the properties and microstructure of the pressureless sintered SiC-TiC composite.

2. EXPERIMENTAL PROCEDURES

2.1. Raw materials and Methods

In this study, α -SiC made by Alfa Aesar, with the mean grain size of 0.3 microns, was utilized as the main powder. In addition, 10 wt% α -Al₂O₃ and Y₂O₃, made by Alfa Aesar, with the particle size less than 1 micron and a ratio of 4.3:5.7 were utilized to produce the liquid phase. TiC powder, with the particle size less than 1 micron was produced by Merck Co., and employed as reinforcement.

Compositions analogous to those shown in Table 1 were prepared to assess the impact of TiC additive on the properties of samples. The weight ratio of Y₂O₃ to Al₂O₃ in these compositions was determined to be 57:43 based on the lowest eutectic temperature.

The powders were mixed in a planetary mill in a tungsten carbide chamber and an ethanol setting, whose rotational speed was set to 180 rpm for 3 hours. Then, the obtained slurry was dried at 100 °C for 24 hours. Next, the samples underwent uniaxial pressing (90 MPa) and turned into cylindrical specimens. Finally, the samples

were sintered at 1900 °C under argon atmosphere for 1.5 hours.

The heating rate was 2 °C/min. After sintering, samples were kept at environment temperature inside the furnace.

According to the assessments, 1900 °C was the best temperature for sintering SiC-Al₂O₃-Y₂O₃ system [8, 11, 20, 25].

TABLE 1. Compositions of each sample

Raw materials	wt%				
	Sample 1	Sample 2	Sample 3	Sample 4	Sample 5
SiC	90	87.5	85	82.5	80
TiC	0	2.5	5	7.5	10
Al ₂ O ₃	4.3	4.3	4.3	4.3	4.3
Y ₂ O ₃	5.7	5.7	5.7	5.7	5.7

2.2. Measurement of properties

The density and porosity of the sintered samples were measured using the Sartorius LA 230S digital scale (with the precision of 0.0001 g), according to C373–88 standard, through Archimedes' method. Equation (1) was used to calculate the theoretical density:

$$\rho_{com} = v_a \rho_a + v_b \rho_b + v_c \rho_c + \dots \quad (1)$$

where v and ρ are the volume fraction and density of a given phase, respectively. Crystalline phases were characterized by X-ray diffraction. Micro-Hardness was measured by Vickers method according to ASTM C1327. The hardness was also calculated by exerting a force of 5 N in an MXT-al microhardness tester, as shown in Equation (2):

$$H = (1.854)P/d^2 \quad (2)$$

where P and d represent the applied force and indentation diameter, respectively.

The indentation fracture toughness of samples was measured based on the ASTM C1421-10 standard. In this method, ESE WEY microhardness tester, DVRB–TV model, was utilized to exert a force of 300 N on the surface of samples so as to develop cracks on their surface. Then, the length of the produced surface cracks was measured, and the toughness of samples was determined using Equation (3):

$$K_{IC} = 0.0752 P/C^{3/2} \quad (3)$$

where P and C represent the applied force and length of the produced surface crack, respectively. In order to study the microstructure, samples were etched by Murakami's reagent using a chemical method. Microstructural studies of the polished and etched surfaces of the sintered samples were undertaken by applying a voltage of 15-20 kV using a scanning electron microscope called Tescan model.

3. RESULTS AND DISCUSSION

3.1. Phase analysis of samples

In Fig. 1, the X-ray diffraction pattern of the samples containing 0, 5, and 10 wt% TiC additives is depicted. In the sample devoid of TiC additives, there can be observed SiC as the dominant phase as well as a negligible amount of the $Y_3Al_5O_{12}$ phase known as the Alumina–Yttria–Garnet (YAG) that exists as the grain-boundary phase. However, in the samples containing TiC additives, other than the SiC phase SiC (JCPDS card 01-073-1663), which is the dominant phase, YAG (JCPDS card 01-088-2048), YAM ($Y_4Al_2O_9$) (JCPDS card 00-014-0475) phases, and TiC (JCPDS card 065-7994) phases are obtained.

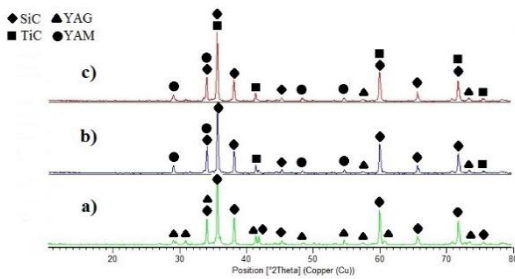
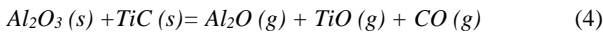


Figure 1. XRD analysis of the sample containing a) 0, b) 5, and c) 10 wt% TiC

According to Fig. 1 (b and c), with an increase in the amount of TiC phase, the intensity and number of TiC peaks increase as well. Additionally, with a rise in the amount of TiC phase, the intensity of YAG peaks decreases and YAM phase reaches the peaks in the XRD of the sintered samples. The probable reaction between the TiC and Al_2O_3 phases (reaction 4), together with the withdrawal of the Al_2O_3 from the composition of the liquid phase, is one of the reasons why the YAM phase is formed [27].



According to Reaction (4), the withdrawal of Al_2O_3 from the composition of the liquid phase and the stoichiometric changes in the YAG phase based on the Al_2O_3 – Y_2O_3 phase diagram (Fig 2.) form the YAM phase. On the one hand, the formation of this phase may be due to the rapid cooling of the samples at room temperature after sintering and decomposing the YAG phase [8,25]. On the other hand, it is possible that with the withdrawal of Al_2O_3 , some excess Y_2O_3 remain in the samples. This Y_2O_3 can react with the SiO_2 existing on the surface of SiC particles, forming Y_2SiO_5 [28]. However, given the XRD patterns of the sintered samples, no Y_2SiO_5 was found.

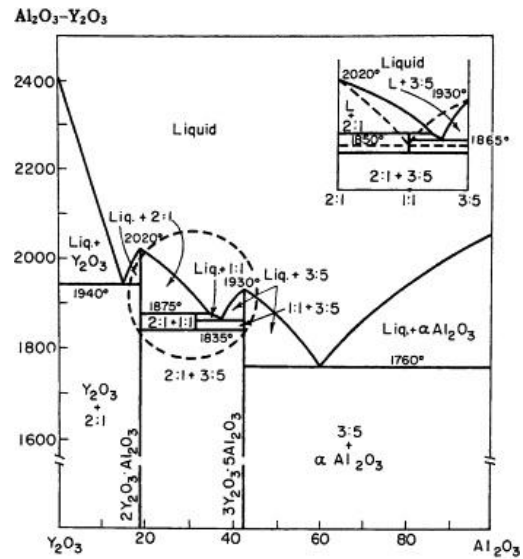


Figure 2. Phase diagram of Al_2O_3 - Y_2O_3 [25]

3.2. Microstructure

In Fig. 3, the line scan analysis of the sample containing 7.5 wt% TiC is depicted. The white-colored regions in grain boundaries contain Al, Y, and O, which somehow confirms the presence of the YAG in the grain boundary of samples. Moreover, given the presence of Ti and C elements in this region, X-Ray diffraction patterns prove the existence of the TiC phase.

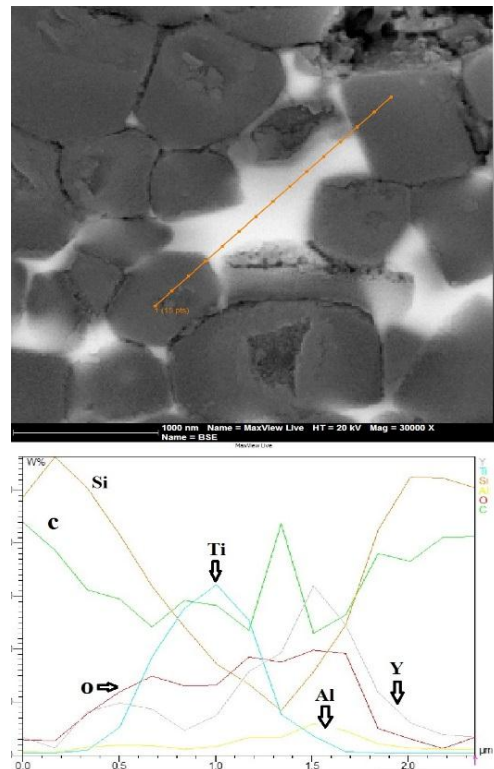


Figure 3. Line scan analysis of sample containing 7.5 wt% TiC

Map analysis of the composition containing 5 wt% TiC additives is depicted in Fig. 4. Clearly, secondary phase particles are homogeneously distributed everywhere.

The microstructures of the samples containing 0, 5, and 10 wt% TiC are represented in Fig. 5. Based on the microstructures of the samples devoid of TiC additives shown in Fig. 5 (a), most of SiC grains are relatively equiaxed and only a negligible amount of elongation in SiC grains is observed.

As observed in Fig. 5 (b-c), in the sample with 5 wt% TiC, the amount of porosity was lower than that in the sample with 10 wt% TiC. Therefore, the relative density of the former is higher than that of the latter. Additionally, according to the images of both samples and presented data in Table 2, it can be concluded that adding up to 5 wt% TiC impedes the excessive growth of SiC grains and refines the microstructure. Nonetheless, Adding up to 10 wt% TiC results in grain growth and based on the obtained results, it reduces the density as well as attenuates mechanical properties.

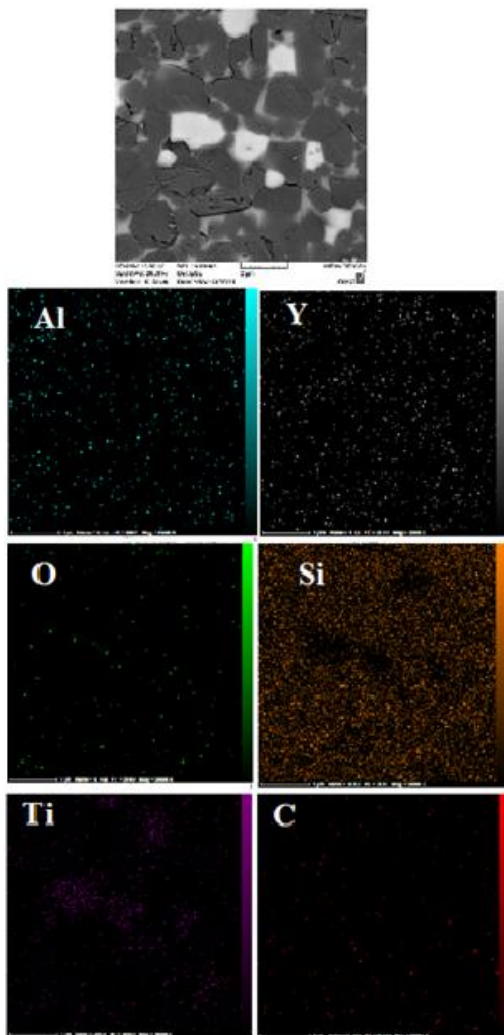


Figure 4. Map analysis of sample containing 5 wt% TiC

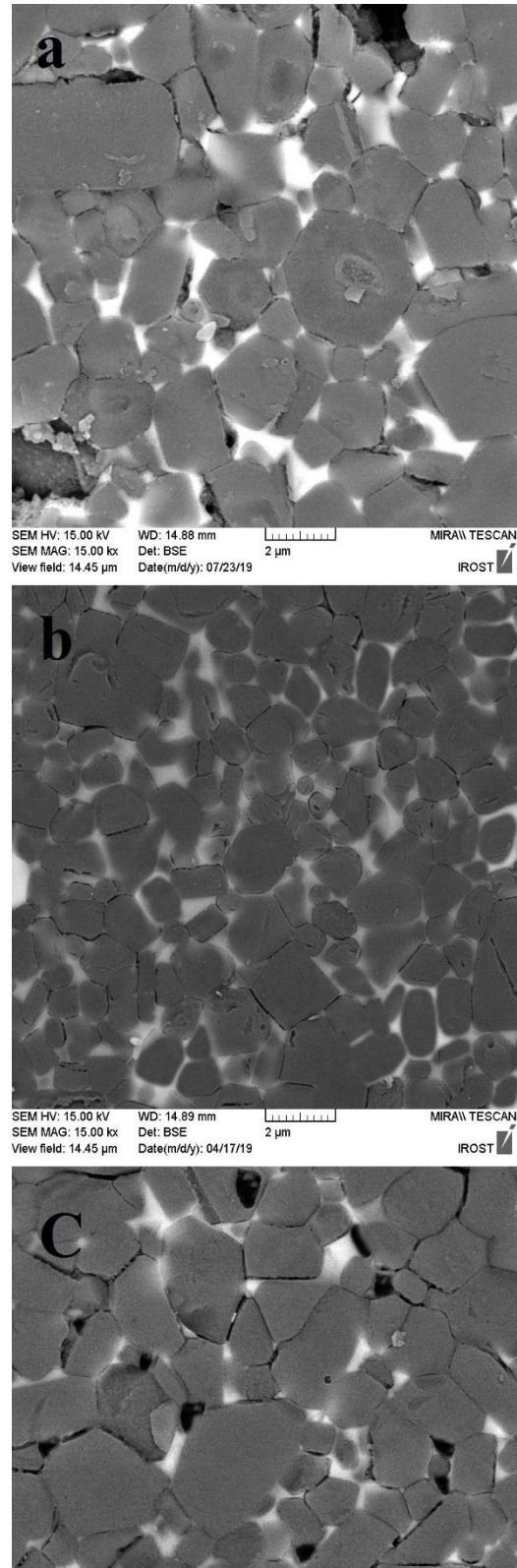


Figure 5. Microstructure images of samples containing a) 0, b) 5, and c) 10 wt% TiC

TABLE 2. The effects of different TiC additives on the grain size of composites

TiC (wt. %)	0	2.5	5	7.5	10
Grain size (μm)	2 ± 0.04	1.5 ± 0.3	1.36 ± 0.07	1.5 ± 0.6	1.8 ± 0.13

Given the presence of TiC particles on the boundaries of SiC grains and their homogeneous distribution in the SiC matrix, a microstructure with fine equiaxed grains is attained in the samples containing 5 wt% and 10 wt% TiC. This suggests that adding TiC impedes the excessive growth of SiC grains and refines the microstructure. Researchers have found that according to Zener's model, the secondary phase impedes the growth of matrix grains [29]. The grain size of the matrix can be calculated using Equation (5).

$$G = 4r/3f \quad (5)$$

where r and f present the radius and volume fraction of the secondary phase, respectively. Equation (5) shows that with an increase in the fraction of the secondary phase, the grain size of the matrix decreases [8,29].

In addition, in compositions with up to 5 wt% TiC additives, the presence of TiC particles on the grain boundaries of the SiC increases the aspect ratio. These obtained results are significant with respect to toughening since any increase in aspect ratio enhances the fracture toughness of the composite [30].

Therefore, it can be asserted that the presence of TiC particles in the grain boundaries of SiC not only refines the matrix but also makes SiC grains elongated. This may be due to the fact that TiC particles precipitate in the grain boundaries of the SiC, limiting the preferred sites for the growth of equiaxed grains [27].

3.3. Evaluation of density, weight loss, and linear shrinkage

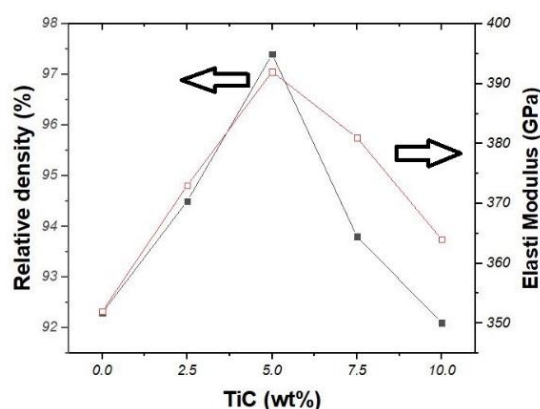
In Fig. 6, the effect of different amounts of TiC additives on densification of the liquid-phased sintered SiC ceramics is illustrated. As observed, by increasing the amount of TiC up to 5 wt%, the density increases, while by adding up to 10 wt% TiC, the density of the composite diminishes. The density of the samples increases due to several reasons: first, the presence of TiC particles on the grain boundaries of SiC reduces the rate of boundary migration, thus minimizing the excessive grain

growth. Second, an increase in surface diffusion and movement of porosities diminish cavities in samples, which increases density during the sintering process [8]. The reason why the density of samples decreases is because there is a reaction between TiC and Al_2O_3 , which is in agreement with the results of XRD patterns. However, if there is not sufficient liquid phase, it cannot wet SiC particles completely, thus creating a great deal

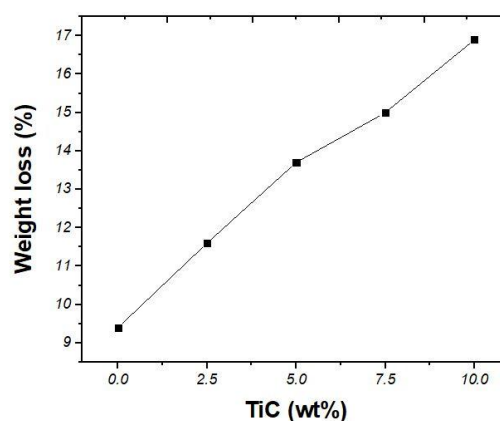
of porosity on the grain boundary phase. This lowers the density and mechanical properties of the sintered samples.

The reactivity between SiC and sintering additives during the sintering process is analyzed by measuring weight loss. Thus, in liquid-phased sintering, the reaction between SiC and additives, especially oxide additives, is almost inevitable, and some weight loss is always observed.

In Fig. 7, the weight loss of the sintered samples is shown according to different amounts of TiC. According to Fig. 7, with an increase in the amount of TiC, the amount of weight loss in samples increases, too.

**Figure 6.** The effect of different amounts of TiC on the relative density and elastic modulus

Given that oxide additives, especially Al_2O_3 , are the main causes of the reactions resulting in the weight loss of samples being sintered, by adding TiC, the constant increase in the weight loss of the samples is predictable.

**Figure 7.** Weight loss variations versus TiC content

3.4. Hardness

In Fig. 8, the hardness variations are shown as a function of the amount of TiC additive. With any

increase in the amount of TiC particles up to 5 wt%, the hardness of the samples increases. However, with the further addition of TiC particles up to 10 wt%, the hardness is diminished. This behavior of the samples was completely congruent with the variations in their density and the highest hardness quantity was achieved in samples with the highest density. Therefore, other than the effect of density on the hardness of samples, grain size reduction can also improve the sample hardness [31-34]. According to hardness results of the samples, adding up to 5 wt% TiC enhances the samples' hardness. It is acknowledged that the presence of TiC particles on the grain boundaries of the SiC lessens the rate of grain-boundary migration and minimizes the excessive grain growth, which increases the samples' density and creates a fine-grained SiC composite [25,29]. Based on Hall-Petch relation [29], it can be asserted that with a reduction in the grain size, the hardness of samples increases.

One of the reasons explaining why an increase in TiC additives reduces the hardness is the formation of microcracks on the interface of SiC and TiC grains, which occurs during the cooling process at the sintering temperature as a result of the mismatch between the thermal expansion coefficient of SiC and that of TiC particles [8]. Fig. 9 presents the produced microcracks in the composition of the composites with 10 wt% TiC.

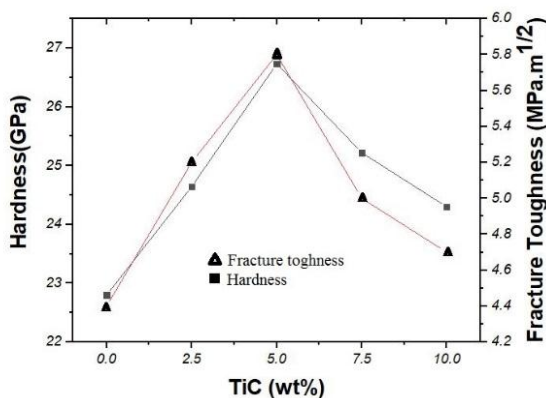


Figure 8. The effect of different amounts of TiC on the Hardness and Fracture Toughness

3.5. Elastic Modulus

Similar to the case of hardness, the elastic modulus is heavily dependent on the porosity and density of samples; therefore, elastic modulus decreases with an increase in porosity or a reduction in the relative density of samples. In Fig. 6, the elastic modulus of the sintered samples with different amounts of TiC additive is represented.

Based on the obtained results, with the addition of TiC, the elastic modulus of the composite went up. However, upon adding more than 5 wt% TiC, the density was diminished and the formation of porosities reduced the sound speed inside the samples. Given that sound waves

are mechanical waves, they need a medium through which they can move. Thus, the lower the amount of matter (less density/more porosity), the slower the speed of sound. Considering the relation between sound speed and Young's modulus, a decline in Young's modulus of samples is expected.

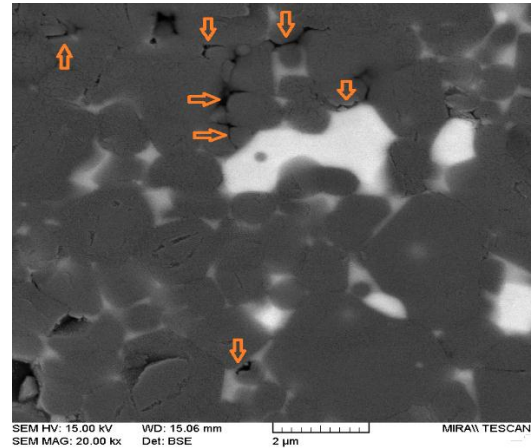


Figure 9. SEM image of the propagation of micro crack in the sample containing 10 wt% TiC

3.6. Fracture Toughness

The variations in fracture toughness are depicted as a function of the amount of TiC additive in Fig. 8. The amount of porosity formed during the sintering process is one of the factors that can affect fracture toughness.

According to the results of the fracture toughness tests such as those of the hardness test, for the samples containing up to 5 wt% TiC, a significant improvement in fracture toughness was achieved. Nevertheless, by adding up to 10 wt% TiC additive to the sintered samples, their fracture toughness steadily decreases. However, the presence of 10 wt% TiC particles in the SiC matrix is beneficial, and the quantities of their fracture toughness are higher than those of the ceramics devoid of TiC additive.

This increase in fracture toughness occurs despite the reduction in the relative density of the samples containing 10 wt% TiC, indicating that the relationship between density and porosity must not be regarded as the only determining factor in the fracture toughness of the samples. Accordingly, it can be asserted that the following elements are influential in the fracture toughness of the SiC-TiC composites: density, reinforcement and its amount, grain morphology, and microstructure [35-37].

The presence of TiC particles on the grain boundaries of SiC enhances the fracture toughness of the sintered bodies due to two reasons: first, the presence of the TiC on the grain boundaries of the SiC refines the matrix grains. The reason why grain refining increases the

fracture toughness can be attributed to the influence of grain boundaries as an obstacle to crack growth [8].

Grain boundaries hinder the movement of cracks. Therefore, a great deal of energy is required for crack nucleation and propagation because it must change its path in order to keep moving on a desirable plane in an adjacent grain.

Another reason for an increase in fracture toughness owing to grain refinement may be related to a reduction in crack length due to the smaller grain size. In such a condition, the crack requires a higher stress for growth and composite failure [8,29].

In addition, using TiC hinders the grain growth and increases the elongation of some SiC grains (Fig. 10), thus improving the fracture toughness of liquid-phase sintered SiC-TiC composites. The elongated SiC grains in the microstructure function as reinforcement and trigger toughening mechanisms such as crack deflection and crack bridging, leading to an improvement in the fracture toughness of SiC bodies. In the following, the toughening mechanisms of this composition will be addressed.

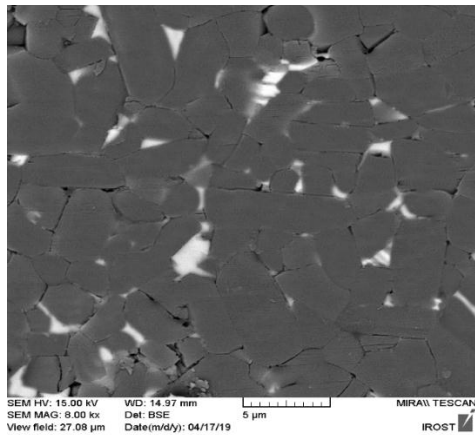


Figure 10. Formation of SiC elongated grains in composite containing 5wt% TiC

3.7. Toughening Mechanisms

The present research utilized Vickers indenter to assess toughening mechanisms and cracks on the polished surface of the samples using a diamond indenter under a 30 kg load. The crack propagation and origin of toughening mechanisms in the SiC ceramics devoid of TiC additive and SiC-TiC composites are presented using an SEM. In Fig. 11 (a), images of crack propagation path in the sample with no TiC additive are shown.

As shown in Fig. 11 (a), the secondary phase is mainly present in the form of a continuous film on the grain boundaries of the SiC. Given that a large proportion of the intergranular phase is comprised of the YAG phase, which is a weak oxide phase, cracks propagate in the form of intergranular cracks. Crack deflection

mechanisms are also observed to a limited extent. In Fig. 11 (b and c), the SEM images of the crack growth path of the ceramics containing 5 wt% and 10 wt% TiC are presented.

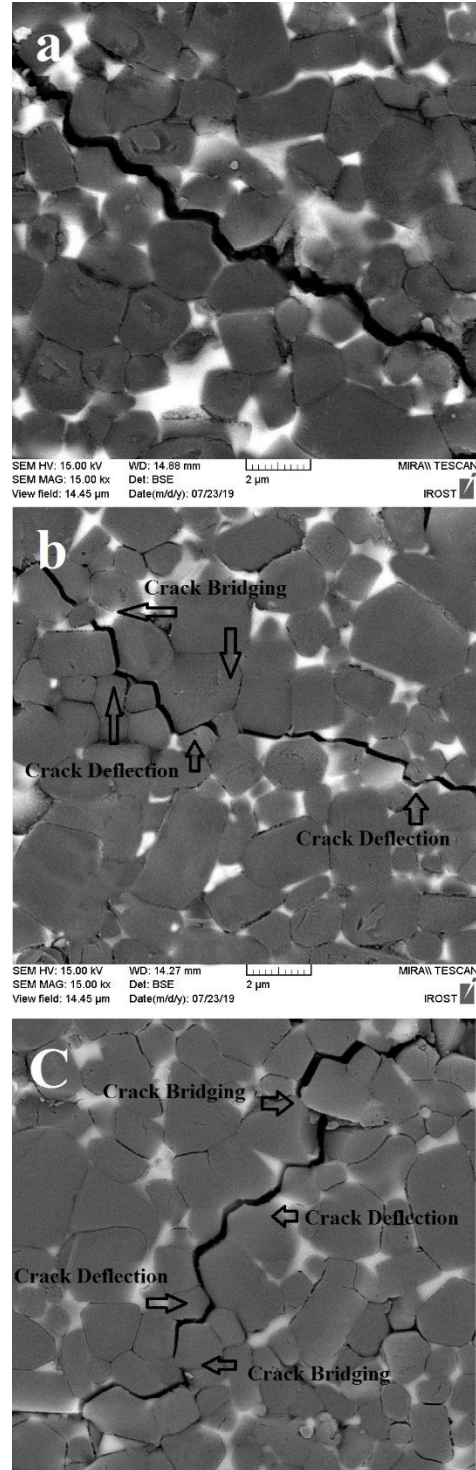


Figure 11. SEM images of the crack path in samples containing: a) 0, b) 5, and c) 10 wt% TiC

According to the evaluations, any enhancement in the fracture toughness of the sintered bodies depends on the grain morphology and formed microstructure [38]. It is probable that in this composition, crack deflection and crack bridging improve fracture toughness. In this regard, the crack deflection mechanism is considered the most significant mechanism in improving the liquid-phase sintered SiC ceramics. The crack deflection mechanism is triggered due to the weak interface between the SiC and the grain boundary phase [8,11].

Another possible mechanism affecting the enhancement of the fracture toughness of these ceramics is the pullout of SiC grains, leading to crack surface bridging.

This mechanism plays a crucial role in the compositions that have elongated grains whose length-to-diameter ratio is high. In the structures containing homogenous (equiaxed) grains, the contribution of this mechanism to the improvement of fracture toughness is not substantial [20,29,39].

A comparison between the results of this study and those of other researchers is presented in Table 3.

TABLE 3. A comparison between the results of this study and those of other researchers

Additive Composition	Relative Density (%)	Hardness (GPa)	Fracture Toughness (MPa.m ^{1/2})	Strength (MPa)	Ref.
Al ₂ O ₃ -Y ₂ O ₃ -TiC	97.40	26.73	5.80	-	This paper
Al ₂ O ₃ -Y ₂ O ₃ -MgO	96.05	26	5.24	440	[32]
Al ₂ O ₃ -Y ₂ O ₃ -TiC	98.1	26.13	4.07	432	[27]
Al ₂ O ₃ -Y ₂ O ₃ -ZrB ₂	98	19.94	6.68	565.70	[39]
Al ₂ O ₃ -Y ₂ O ₃ -TiC	97	-	7.8	-	[40]
Al ₂ O ₃ -Y ₂ O ₃ -TiO ₂	99.2	27.4	4.6	516	[30]
Al ₂ O ₃ -Y ₂ O ₃ -AlN	97	25.7	3.1	582	[41]

4. CONCLUSIONS

1. Based on the results of the present study, the liquid Al₂O₃-Y₂O₃ is a useful additive for the liquid phase sintering of SiC-TiC composites.
2. The sample containing 5 wt% TiC additives exhibits the highest density, Young's modulus, hardness, and fracture toughness. However, with further increasing the amount of TiC additive to 10 wt%, these properties would deteriorate.

3. Introduction of a negligible amount of TiC additive (5 wt%) is sufficient enough to impede the growth of SiC grains and improve the mechanical properties of SiC ceramics.
4. The samples with the highest density and the finest microstructure exhibit higher hardness. The formation of microcracks with an increase in the amount of TiC is one of the reasons why hardness is reduced.
5. Among the parameters that affect the fracture toughness of SiC-TiC composites are density, amount and type of reinforcement, grain morphology, and microstructure.
6. Active mechanisms that improve the fracture toughness of SiC-TiC composite are crack deflection and crack bridging. As a result, crack deflection is the dominant mechanism in the fracture toughness of SiC-TiC composites.

REFERENCES

1. Lopez, O., Ortiz, A., Guiberteau, F., Padture, N., "Microstructural design of sliding wear resistant liquid-phase-sintered SiC: an overview", *Journal of the European Ceramic Society*, Vol. 27, No. 11, (2007), 3351-3357. <https://doi.org/10.1016/j.jeurceramsoc.2007.02.190>
2. Janney, M., "Mechanical properties and oxidation behavior of a hot pressed SiC-15 vol% TiB₂ composite", *American Ceramic Society Bulletin*, Vol. 66, No. 2, (1987), 322-324
3. Ghadami, S., Baharvandi, H. R., Ghadami, F., "Influence of the vol% SiC on properties of pressureless Al₂O₃/SiC nanocomposites", *Journal of Composite Materials*, Vol. 50, No. 10, (2016), 1367-75. <https://doi.org/10.1177/0021998315591300>
4. Noviyanto, A., Yoon, D., "One component metal oxide sintering additive for β-SiC based on thermodynamic calculation and experimental observations", *Metals and Materials International*, Vol. 18, No. 1, (2012), 63-68. <https://doi.org/10.1007/s12540-012-0008-z>
5. Noviyanto, A., Yoon, D., "Metal oxide additives for the sintering of silicon carbide: reactivity and densification", *Current Applied Physics*, Vol. 13, No. 1, (2013), 287-292. <https://doi.org/10.1016/j.cap.2012.07.027>
6. Ortiz, A. L., Borrero-Lopez, O., Quadir, M. Z., Guiberteau, F., "A route for the pressureless liquid-phase sintering of SiC with low additive content for improved sliding-wear resistance", *Journal of the European Ceramic Society*, Vol. 32, No. 4, (2012), 965-976. <https://doi.org/10.1016/j.jeurceramsoc.2011.10.052>
7. Ghadami, S., Taheri-Nassaj, E., Baharvandi, H. R., "Novel HfB₂-SiC-MoSi₂ composites by reactive spark plasma sintering", *Journal of Alloys and Compounds*, Vol. 809, (2019), 151705. <https://doi.org/10.1016/j.jallcom.2019.151705>
8. Khodaei, M., Yaghoobizadeh, O., Baharvandi, H. R., Dashti, A., "Effects of different sintering methods on the properties of SiC-TiC, SiC-TiB₂ composites", *International Journal of Refractory Metals and Hard Materials*, Vol. 70, (2018), 19-31. <https://doi.org/10.1016/j.ijrmhm.2017.09.005>
9. Magnani, G., Beltrami, G., Minoccarri, G. L., pilotti, L., "Pressureless sintering and properties of αSiC-B₄C composite", *Journal of the European Ceramic Society*, Vol. 21, No. 5,

- (2001), 633–638. [https://doi.org/10.1016/S0955-2219\(00\)00244-2](https://doi.org/10.1016/S0955-2219(00)00244-2)
10. Ribeiro, S., Ribeiro, G. C., Mrego de oliveira, “Properties of SiC ceramics sintered via liquid phase using $\text{Al}_2\text{O}_3 + \text{Y}_2\text{O}_3$, $\text{Al}_2\text{O}_3 + \text{Yb}_2\text{O}_3$ and $\text{Al}_2\text{O}_3 + \text{Dy}_2\text{O}_3$ as additives: a comparative study”, *Materials Research*, Vol. 18, No. 3, (2015), 525–529. <https://doi.org/10.1590/1516-1439.311314>
 11. Khodaei, M., Yaghobizadeh, O., Shahraki, A. A., Esmaceli, S., “Investigation of the effect of $\text{Al}_2\text{O}_3\text{-Y}_2\text{O}_3\text{-CaO}$ (AYC) additives on sinterability, microstructure and mechanical properties of SiC matrix composites: a review”, *International Journal of Refractory Metals and Hard Materials*, Vol. 78, (2018), 9–26. <https://doi.org/10.1016/j.jrmhm.2018.08.008>
 12. Suzuki, S., sasaki, M., “Effects of sintering atmosphere on grain morphology of liquid phase- sintered SiC with Al_2O_3 additions”, *Journal of the European Ceramic Society*, Vol. 25, No. 9, (2005), 1611–1618. <https://doi.org/10.1016/j.jeurceramsoc.2004.06.007>
 13. Zhang J., Jiang, D., Lin, Q., Chen, Z., Huang, Z., “Properties of silicon carbide ceramics from gelcasting and pressureless sintering”, *Materials & Design*, Vol. 65, (2015), 12–16. <https://doi.org/10.1016/j.matdes.2014.08.034>
 14. Noviyanto, A., Yoon, D.H., “Rare-earth oxide additives for the sintering of silicon carbide”, *Diamond and Related Materials*, Vol. 38, (2013), 124–130. <https://doi.org/10.1016/j.diamond.2013.07.003>
 15. Tatarko, P., Lojanova, S., Dusza, J., Šajgalik, P., “Influence of various rare-earth oxide additives on microstructure and mechanical properties of silicon nitride based nanocomposites”, *Materials Science and Engineering: A*, Vol. 527, No. 18-19, (2010), 4771–4778. <https://doi.org/10.1016/j.msea.2010.04.069>
 16. Liang, H., Yao, X., Zhang, J., Liu, X., Huang, Z., “The effect of rare earth oxides on the pressureless liquid phase sintering of $\alpha\text{-SiC}$ ”, *Journal of the European Ceramic Society*, Vol. 34, No. 12, (2014), 2865–2874. <https://doi.org/10.1016/j.jeurceramsoc.2014.03.029>
 17. Lopez, O.B., Ortiz, A., Guiberteau, F., Padture, N., “Effect of liquid-phase content on the contact-mechanical properties of liquid-phase-sintered $\alpha\text{-SiC}$ ”, *Journal of the European Ceramic Society*, Vol. 27, No. 6, (2007), 2521–2527. <https://doi.org/10.1016/j.jeurceramsoc.2006.09.012>
 18. Magnani, G., Minocari, G. L., Pilotti, L., “Flexural strength and toughness of liquid phase sintered silicon carbide”, *Ceramic International*, Vol. 26, No. 5, (2000), 495–500. [https://doi.org/10.1016/S0272-8842\(99\)00084-X](https://doi.org/10.1016/S0272-8842(99)00084-X)
 19. Neher, R., Herrmann, M., Brandt, K., Jaenicke-Roessler, K., Pan, Z., Fabrichnaya, O., Seifert, H. J., “Liquid phase formation in the system SiC, Al_2O_3 , Y_2O_3 ”, *Journal of the European Ceramic Society*, Vol. 31, No. 1-2, (2011), 175–181. <https://doi.org/10.1016/j.jeurceramsoc.2010.09.002>
 20. Khodaei, M., Yaghobizadeh, O., Naghavi, S.H., Alhosseini, Esmaceli, S., Mousavi, S.R., “The effect of Oxide, Carbide, Nitride and Boride additives on properties of pressureless sintered SiC: a Review”, *Journal of the European Ceramic Society*, Vol. 39, No. 7, (2019), 2215–2231. <https://doi.org/10.1016/j.jeurceramsoc.2019.02.042>
 21. Ihle, J., Herrmann, M., Adler, J., “Phase formation in porous liquid phase sintered silicon carbide: part III: interaction between $\text{Al}_2\text{O}_3\text{-Y}_2\text{O}_3$ and SiC”, *Journal of the European Ceramic Society*, Vol. 25, No. 7, (2005), 1005–1013. <https://doi.org/10.1016/j.jeurceramsoc.2004.04.017>
 22. Lee, S. M., Kim, T. W., Lim, H. J., Kim, C., Kim, Y. W., Lee, K. S., “Mechanical properties and contact damages of nanostructured silicon carbide ceramics”, *Journal of the Ceramic Society of Japan*, Vol. 115, No. 1341, (2007), 304–309. <https://doi.org/10.2109/jcersj.115.304>
 23. Huang, Z. H., Jia, D. C., Zhou, Y., Wang, Y. J., “Effect of a new additive on mechanical properties of hot-pressed silicon carbide ceramics”, *Materials Research Bulletin*, Vol. 37, No. 5, (2002), 933–940. [https://doi.org/10.1016/S0025-5408\(02\)00704-3](https://doi.org/10.1016/S0025-5408(02)00704-3)
 24. Guo, W., Jin, Z. G., Xu, T. X., Wu, W. B., “Low temperature pressureless sintering of SiC ceramics with $\text{Al}_2\text{O}_3\text{-Y}_2\text{O}_3\text{-La}_2\text{O}_3$ Addition”, In *Key Engineering Materials*, Trans Tech Publications Ltd, Vol. 226, (2002), 725–728. <https://doi.org/10.4028/www.scientific.net/KEM.224-226.725>
 25. Khodaei, M., Yaghobizadeh, O., Ehsani, N., Baharvandi, H. R., “The effect of TiO_2 additive on the electrical resistivity and mechanical properties of pressureless sintered SiC ceramics with $\text{Al}_2\text{O}_3\text{-Y}_2\text{O}_3$ ”, *International Journal of Refractory Metals and Hard Materials*, Vol. 76, (2018), 141–148. <https://doi.org/10.1016/j.jrmhm.2018.06.005>
 26. Huang, Z. H., Jia, D. C., Zhou, Y., Liu, Y. G., “A new sintering additive for silicon carbide ceramic”, *Ceramic International*, Vol. 29, No. 1, (2003), 13–17. [https://doi.org/10.1016/S0272-8842\(02\)00082-2](https://doi.org/10.1016/S0272-8842(02)00082-2)
 27. Liang, H. Q., Yao, X. M., Zhang, H., Liu, X. J., Huang, Z. R., “The effect of TiC on the liquid phase sintering of SiC ceramics with Al_2O_3 and Y_2O_3 additives”, In *Key Engineering Materials*, Trans Tech Publications Ltd, Vol. 602, (2014), 197–201. <https://doi.org/10.4028/www.scientific.net/KEM.602-603.197>
 28. Marchi, J., Bressiani, J. C., Bressiani, A. H.A., “Densification Studies of Silicon Carbide-Based Ceramics with Ytria, Silica and Alumina as Sintering Additives”, *Materials Research*, Vol. 4, No. 4, (2000), 231–236. <https://doi.org/10.1590/s1516-14392001000400002>
 29. Khodaei, M., Yaghobizadeh, O., Ehsani, N., Baharvandi, H. R., Dashti, A., “The effect of TiO_2 additive on sinterability and properties of SiC- $\text{Al}_2\text{O}_3\text{-Y}_2\text{O}_3$ composite system”, *Ceramic International*, Vol. 44, No. 14, (2018), 16535–16542. <https://doi.org/10.1016/j.ceramint.2018.06.073>
 30. Liang, H., Yao, X., Zhang, H., Liu, X., Huang, Z., “In situ toughening of pressureless liquid phase sintered $\alpha\text{-SiC}$ by using TiO_2 ”, *Ceramic International*, Vol. 40, No. 7, (2014), 10699–10704. <https://doi.org/10.1016/j.ceramint.2014.03.055>
 31. Foster, D., Thompson, D. P., “The use of MgO as a densification aid for $\alpha\text{-SiC}$ ”, *Journal of the European Ceramic Society*, Vol. 19, No. 16, (1999), 2823–2831. [https://doi.org/10.1016/S0955-2219\(99\)00060-6](https://doi.org/10.1016/S0955-2219(99)00060-6)
 32. Gubernat, A., Stobierski, L., Labaj, P., “Microstructure and mechanical properties of silicon carbide pressureless sintered with oxide additives”, *Journal of the European Ceramic Society*, Vol. 27, No. 2-3, (2007), 781–789. <https://doi.org/10.1016/j.jeurceramsoc.2006.04.009>
 33. Zawrah, M. F., Shaw, L., “Liquid-phase sintering of SiC in presence of CaO”, *Ceramic International*, Vol. 30, No. 5, (2004), 721–725. <https://doi.org/10.1016/j.ceramint.2003.07.017>
 34. Eom, J. H., Seo, Y. K., Kim, Y. W., “Mechanical and thermal properties of pressureless sintered silicon carbide ceramics with alumina–Ytria–Calcium”, *Journal of the American Ceramic Society*, Vol. 99, No. 5, (2016), 1735–1741. <https://doi.org/10.1111/jace.14114>
 35. Khodaei, M., Yaghobizadeh, O., Baharvandi, H. R., Alipour Shahrakia, A., Mohammadi, H., “The effect of nano- TiO_2 additions on the densification and mechanical properties of SiC-matrix composite”, *Ceramic International*, Vol. 46, No. 5, (2020), 6477–6483. <https://doi.org/10.1016/j.ceramint.2019.11.128>
 36. Ahmoye, D., Krstic, V. D., “Reaction sintering of SiC composites with in situ converted TiO_2 to TiC”, *Journal of Materials Science*, Vol. 50, No. 7, (2015), 2806–2812. <https://doi.org/10.1007/s10853-015-8838-y>
 37. Eom, J. H., Seo, Y. K., Kim, Y. W., Lee, S. J., “Effect of additive composition on mechanical properties of pressureless sintered silicon carbide ceramics sintered with alumina, aluminum nitride and Ytria”, *Metals and Materials International*, Vol. 21, No. 3, (2015), 525–530. <https://doi.org/10.1007/s12540-015-4383-0>
 38. Ahmoye, D., Bucevac, D., Krstic, V. D., “Mechanical properties of reaction sintered SiC-TiC composite”, *Ceramics International*, Vol. 44, No. 12, (2018), 14401–14407. <https://doi.org/10.1016/j.ceramint.2018.05.050>

39. Hui, Y., Lingjie, Z., Xingzhong, G., Xiaoyi, Z., Xiaojian, F., "Pressureless sintering of silicon carbide ceramics containing zirconium diboride", *Ceramic International*, Vol. 37, No. 6, (2011), 2031-2035. <https://doi.org/10.1016/j.ceramint.2011.01.048>
40. Kim, Y. W., Lee, S. G., Lee, Y. I., "Pressureless sintering of SiC-TiC composites with improved fracture toughness", *Journal of Materials Science*, Vol. 35, No. 22, (2000), 5569-5574. <https://doi.org/10.1007/bf00544471>
41. Kim, K. J., Eom, J. H., Kim, Y. W., Seo, W. S., Lee, M. J., Hwang, S. S., "Highly resistive SiC ceramics sintered with Al₂O₃-AlN-Y₂O₃ additions", *Ceramic International*, Vol. 43, No. 6, (2017), 5343-5346. <https://doi.org/10.1016/j.ceramint.2017.01.058>



Synthesis and Characterization of Barium Aluminosilicate Glass as the Sealant for Solid Oxide Fuel Cell Application

P. Safarzadeh Kermani ^a, M. Ghatee ^{a*}, A. Yazdani ^a

^a Department of Materials Science and Engineering, Shahrood University of Technology, Shahrood, Iran

PAPER INFO

Paper History:

Received 21 May 2020
Accepted in revised form 20 June 2020

Keywords:

Barium Aluminosilicate
Glass Sealant
Solid Oxide Fuel Cells
Mechanical Properties

ABSTRACT

In this study, barium aluminosilicate glass sealant was synthesized and characterized for Solid Oxide Fuel Cell (SOFC) applications. First, the stoichiometric amounts of powder were mixed and melted at 1330°C for 2h, followed by quenching in water. They were then pressed into cylindrical specimens under load of 200 MPa, followed by sintering at different temperatures. The phase content and microstructure of the samples were analyzed by X-ray Diffraction (XRD) and Scanning Electron Microscope (SEM) methods, respectively. Microhardness and toughness of the sintered samples were investigated by means of Vickers micro-hardness test. Young's modulus and nano-hardness of the glass sealant were measured by nano-indentation method. The thermal expansion coefficient of the specimens was estimated by a dilatometer. The results showed that after sintering at 750°C, sealants with homogeneous microstructure and high density were obtained. The sealants were characterized by mechanical and thermal properties appropriate for SOFC applications with a very low leak rate.

1. INTRODUCTION

High-temperature sealants are among the most important components of the planar Solid Oxide Fuel Cells (p-SOFCs) [1]. The p-SOFCs are composed of at least three thin layers including cathode, electrolyte, and anode. The fuel is fed into the anode side while the cathode is in contact with the oxidant gas (oxygen) [1]. Different fuels, with their own advantages and disadvantages, are used in SOFCs, among which pure hydrogen, ethanol, methane, etc. can be considered [2]. Usually, in a commercial SOFC, 8mol% Yttria Stabilized Zirconia (8YSZ), Ni/YSZ, and Lanthanum Strontium Manganite (LSM) are used for electrolyte, anode, and cathode, respectively [2]. The fuels and oxidant in a p-SOFC must be kept separate since mixing these gasses deteriorates cell performance. Indeed, sealants that prevent the intermixing of fuel and oxidant plays a crucial role in the development of SOFCs with high output power [3]. The sealants in the SOFCs must be kept stable during the service life and be compatible with other cell components. Therefore, the sealing materials must be thermodynamically, chemically, and mechanically stable in harsh working conditions of SOFC, including reducing and oxidizing conditions, at high temperatures (T~800°C) [4].

The sealants should be compatible with other components and remain chemically inert during their service life. In addition, any mismatch in the thermal expansion coefficients (α) of sealants and other components creates thermal stress in the cell structure, resulting in premature degradation of the SOFC [4].

There are a number of different sealing materials developed for the SOFCs which are categorized into three types including compressive sealants, compliant sealants, and rigidly bonded sealants [5]. The compressive sealants which are based on materials with layered structure, such as mica, can mitigate the mismatch of " α " among different components through the slippage of the structural layers [6]. This kind of sealant behaves like a gasket and does not provide enough sealing performance unless an external pressure is applied on the sealant which complicates the SOFC cell design [7]. The compliant and rigid sealants are mainly based on glass and glass ceramics which soften at high temperatures and provide hermetic joints [8-11]. The glass-based rigid sealants that are rigid materials at low temperatures and are transformed into highly viscous glass at higher temperatures glue the components together through chemical bonding. These kinds of sealants are vulnerable to cracking due to their brittleness and thermal stresses rising during the

* Corresponding Author Email: mghatee@yahoo.com (M. Ghatee)

heating/cooling cycles in the SOFCs. However, the magnitude of " α " of these sealants can be adjusted by controlling the composition. Various rigid glass sealants were developed for SOFC sealing including alkali silicates, alkaline earth silicates, borosilicates, aluminoborosilicate, etc. [8].

Barium/Calcium Aluminosilicate (BCAS) glasses which are originally developed by Pacific Northwest National Laboratory Institute are among the most significant sealing materials used for high-temperature SOFCs and have been the subject of numerous studies [11–14]. It has been reported that adding oxides such as La_2O_3 , Nd_2O_3 , TiO_2 , ZnO , and Y_2O_3 affects different properties of BCAS glass materials [15]. Yang et al. studied the chemical stability of BCAS glass sealant under fuel cell working conditions [16]. Milhans et al. investigated the creep properties of BCAS glass at high temperatures [11]. Batfalsky et al. reported the chemical interaction between BCAS sealants and SOFC interconnect [17].

BCAS glass ceramics are used to join and seal different metallic and non-metallic materials [14,18]. These glass materials are electrically insulating and create gas-tight joints [19]. In this type of glasses, BaO and SiO_2 are network formers, CaO is network modifier, and Al_2O_3 is an intermediate oxide which can be either network former or modifier. The glass composition directly affects the thermal properties of the BCAS glass [18,20].

According to recent reports, adding second phases such as alumina [21], SiC fiber [22], and zirconia particles [19] improved the mechanical properties of BCAS glass ceramics. However, there is not enough comprehensive report on different properties of BCAS glass sealants.

This study aims to synthesize and characterize the BCAS glass for SOFC applications. First, the glass powder is synthesized by solid oxide mixing followed by melt quenching process. An organic vehicle with a basic function of mixing terpineol with ethyl cellulose is developed to render the required flowability to the sealant. Young's modulus, hardness, compressive strength, and toughness of the sintered samples are also investigated. The Coefficient of Thermal Expansion (CTE) and leak rate are also measured at high temperatures.

2. EXPERIMENTAL PROCEDURE

The BCAS glass was synthesized by solid mixing followed by melt quenching method. All powders with more than 99.9 wt% purity were purchased from Merck Company. First, powders were washed in acetone and dried overnight. The composition of the glass is presented in Table 1. The weighted amounts of the powders were mixed with acetone and sonicated for 15 min followed by magnetic stirring until the solvent evaporates. The mixed powders were pressed into

cylindrical pellets under load of 200 MPa in order to reduce their volume occupied by the raw materials during melting process.

TABLE 1. The composition of the constituents of the glass powder

Component	B_2O_3	SiO_2	CaO	BaO	Al_2O_3
Amount (wt%)	7.3	22.1	8.8	56.4	5.4

The pellets were then heated to 1330°C with a heating rate of 10 K/min and held at that temperature for 30 min in a platinum crucible.

The melted material was then quenched in water in a stainless steel cylinder and the prepared powders were crushed using planetary ball mill for 2h at 300 rpm. In order to prepare the sample for further analysis, the prepared glass powder was mixed with 5 wt% Polyvinyl Alcohol (PVA). The prepared mixture was formed into a disk with a diameter of 10 mm and height of 5 mm by uniaxial pressing under pressure of 200 MPa. The specimens were sintered at different temperatures from 600°C to 800°C for 2h. The heating rate in all sintering processes was 20K/min.

The density of the sintered samples was measured using Archimedes method (Precisa, Switzerland) with accuracy of $\pm 0.1 \text{ g/cm}^3$.

The phase content of the samples was studied by X-Ray Diffraction method (XRD, PW1730, Philips, Netherland) using CuK_α radiation. The microstructure of the sintered samples was investigated by SEM (Mira3, TESCAN, Czech Republic).

The Vickers micro-hardness of the sintered glass was measured under load of 50g applied on the polished surfaces. The toughness of the samples was measured using the Anstis formula [23] by means of the Vickers micro-hardness test under different applied loads. Young's modulus and nano-hardness of the prepared sealants were evaluated by the nanoindentation method (NHT3-Anton paar, Austria). The compressive strength of the sintered specimens was measured by the uniaxial testing machine with a loading rate of 0.15 MPa/s on the samples with diameter and height of 10 mm.

The thermal expansion coefficient of the sample was measured by dilatometer (DIL 402, Netch, Germany) with a heating rate of 10 K/min.

The sealing performance was studied by homemade setup, as depicted in Fig.1.

To prepare flowable sealant paste, the glass powder was mixed with different amounts of the ethyl cellulose/terpineol with different proportions, and the resulting mixture ball was milled for 2h using zirconia grinding media. A button single cell SOFC was placed at the end of the alumina tube and the paste was applied around the sample. The sealed sample was placed inside

a programmable furnace, heated to 250°C to dry the paste, and kept at that temperature for 1 h. Argon gas was used in the leak test at pressure of 0.3 KPa and the pressure drops were recorded at different times by a pressure gauge at a temperature of 750°C.

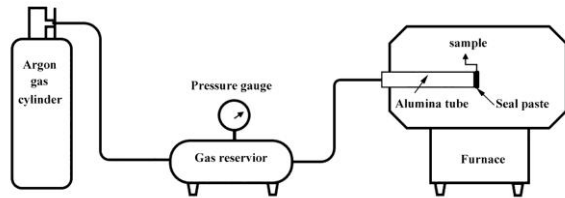


Figure 1. The schematic picture of leak rate test setup

3. RESULTS AND DISCUSSION

The result of the XRD analysis of the prepared glass powders is presented in Fig.2. As observed, the glass was fully amorphous and no crystallization occurred during the sample preparation.

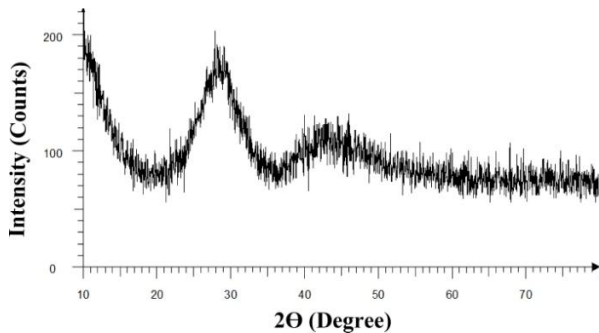


Figure 2. XRD pattern of prepared glass powder

The density variations of the samples as a function of the sintering temperature are presented in Fig. 3. Given that the theoretical density of the pure glass is 3.93 g/cm³, it is observed that the relative density (measured density/theoretical density) of the sample sintered at 750°C is around 98% and does not increase at higher temperatures. Therefore, it can be concluded that the sintering temperature of the BCAS glass is ~750°C. The properties of the specimens sintered at 750°C are presented in the following.

The SEM image of the sintered sample at 750°C is presented in Fig.4 and it confirms the homogeneity of the microstructure with high density.

The mechanical properties of the sintered pellets are presented in Table 2. The hardness of the sintered glass is consistent with previously reported data on other similar glasses [20].

Nano-hardness was calculated by Eq. 1 [24]:

$$H_c = \frac{P_{\max}}{A(h_c)} \quad (1)$$

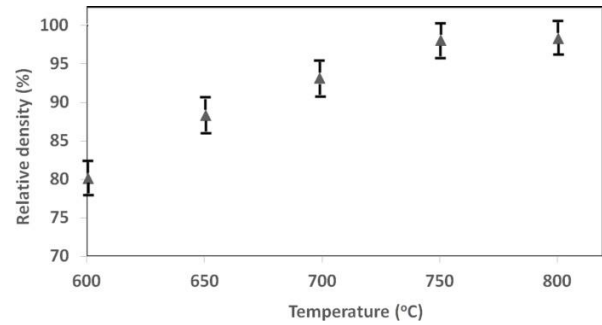


Figure 3. The density variations of the sample as a function of temperature

where P_{\max} is the peak load and $A(h_c)$ is the projected area of the Berkovich tip. The value of $A(h_c)$ for non-ideal Berkovich indenter is determined through Eq. 2 [24]:

$$A(h_c) = h_{\max} - 0.75 \frac{P_{\max}}{S} \quad (2)$$

Where h_{\max} is the maximum penetration depth and S is the contact stiffness which is the slope of the upper portion of the unloading curve. Young's modulus was calculated using Eq. 3 [20]

$$\frac{1}{E_r} = \frac{1 - \nu^2}{E} + \frac{1 - \nu_i^2}{E_i} \quad (3)$$

where E_r is the reduced elastic modulus, considering the fact that elastic displacement occurs in both the specimen and indenter. Here, E and ν represent the elastic modulus and Poisson's ratio of the sample, respectively. The elastic constants of the diamond indenter were assumed to be $E_i = 1140$ GPa and $\nu_i = 0.07$.

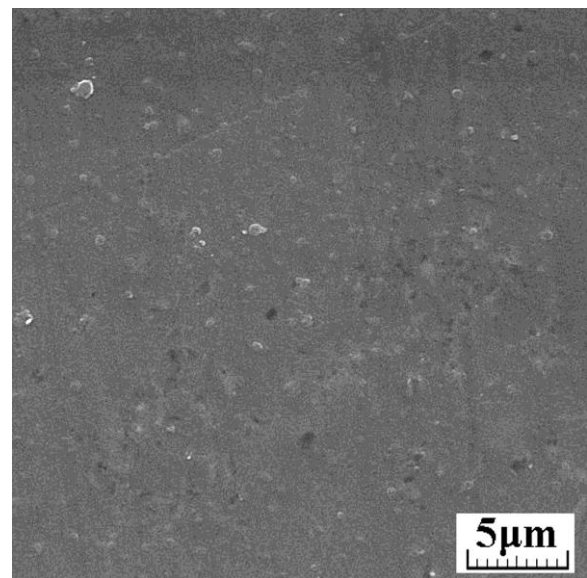


Figure 4. The SEM image of the sintered glass

TABLE 2. The mechanical properties of the sintered sample

Sample	Micro-Hardness (GPa)	Nano-Hardness	Young's modulus (GPa)	Toughness (MPa.m ^{1/2})	Compression strength (MPa)
BCAS	6.1 ± 0.1	6.4 ± 0.5	72.74 ± 8.1	0.15 ± 0.2	191.26 ± 23.5

The nanoindentation load-displacement curve is presented in Fig.5. No pop-in behavior is observed in the loading/unloading curve; therefore, it can be concluded that the microstructure is homogeneous with high density. The presence of porosity and/or any microstructural inhomogeneity results in discontinuity in the load-displacement curve in nano-indentation test [21]. Young's modulus is a significant parameter in managing thermal stress of the solid oxide fuel cell seal materials. Young's modulus of different parts of SOFC must be consistent to prevent the rise of thermal stress. In addition, the toughness of the ceramic materials is proportional to the magnitude of Young's modulus. The reported Young's modulus in this study is comparable with the previously reported data[14]. The magnitudes of nano-hardness and microhardness in Table 2 are in complete agreement, thus confirming the homogeneity of the microstructure.

The measured compression strength is 191.2 MPa which is in the common range of the reported values for pure sintered glass seal materials [25]. The glass ceramic sealants in SOFCs are usually under compressive applied pressure of 0.16 MPa. Indeed, the sealants manufactured in this study attained the required level of compressive strength [21].

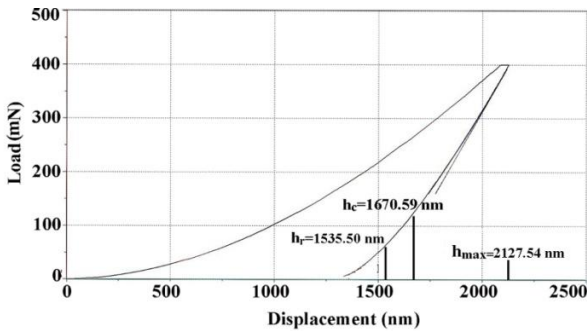


Figure 5. The nanoindentation load-displacement curve for the pure sintered glass

Fig.6 presents the result of dilatometry analysis; in addition, the estimated value of the average thermal expansion coefficient is $12.2 \times 10^{-6} K^{-1}$ which is comparable to the ones reported for other components of the commercial SOFCs. The crystallization temperature (T_g) and softening temperature (T_s) of the sealant are 630°C and 680°C respectively. The softening temperature is a crucial factor regarding the

performance of the sealants because at temperatures higher than T_s , the glass softens and flows among the components and makes hermetic joint. The working temperature of the SOFCs must be higher than the softening point of the sealant.

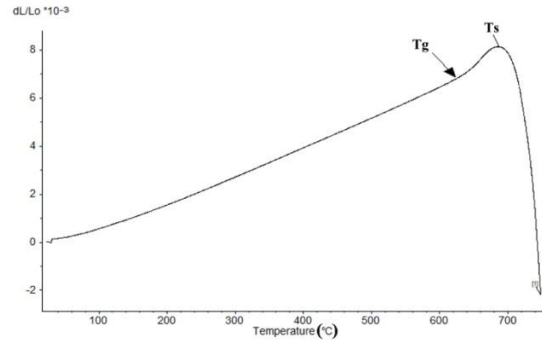


Figure 6. The result of dilatometry analysis of the sintered glass

The result of leak test is presented in Fig. 7 in which the leak rate (LR) was calculated as follows [6]:

$$LR = \frac{(P_f - P_i)V}{RT(t_f - t_i)} \tag{4}$$

where "P" represents pressure, "R" the gas constant, V the reservoir volume, "T" the temperature, and "t" the time.

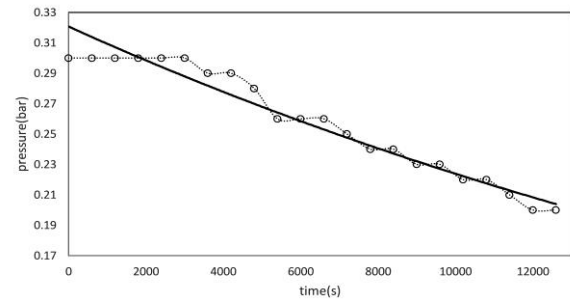


Figure 7. The result of leak test

The proper composition of the sealant paste was 90 wt% glass powder mixed with 10 wt% organic vehicles. The terpeneol-to-ethyl cellulose ratio in the organic vehicle was 3 to 1 wt%. These proper compositions were obtained through trial and error, using the leak test as an acceptable condition for the proper performance. The leak rate of the sealant with proper composition at 750°C was $1.408 \times 10^{-4} sccm/cm$, which was quite low and acceptable for SOFC applications. The prolonged performance of the synthesized sealant under fuel cell working conditions requires more investigations.

4. CONCLUSION

The BCAS glass sealant was successfully synthesized through the melt quenching method. The sintering process at a temperature of 750°C conferred a relative density of 98% to the glass. The micro-hardness and compressive strength of the sealant were 6.1 GPa and 191.2 MPa, respectively. The Young's modulus and nano-hardness measured by nano-indentation test method were 6.4 GPa and 72.7 GPa, respectively. The sealant had a thermal expansion coefficient of $12.2 \times 10^{-6} \text{K}^{-1}$, and the magnitude of T_s was estimated at 680°C. The measured leak rate was 1.408×10^{-4} sccm/cm at 750°C, which is acceptable for SOFC.

5. ACKNOWLEDGMENT

The authors acknowledge the financial support from Shahrood University of Technology.

REFERENCES

- Jamil, S. M., Othman, M. H. D., Rahman, M. A., Jaafar, J., Ismail, A. F., Li, K., "Recent fabrication techniques for micro-tubular solid oxide fuel cell support: a review", *Journal of the European Ceramic Society*, Vol. 35, No. 1, (2015), 1-22. <https://doi.org/10.1016/j.jeurceramsoc.2014.08.034>
- Yano, M., Tomita, A., Sano, M., Hibino, T., "Recent advances in single-chamber solid oxide fuel cells: a review", *Solid State Ionics*, Vol. 177, No. 39-40, (2007), 3351-3359. <https://doi.org/10.1016/j.ssi.2006.10.014>
- Mahapatra, M. K., Lu, K., "Seal glass for solid oxide fuel cells", *Journal of Power Sources*, Vol. 195, No. 21, (2010), 7129-7139. <http://doi.org/10.1016/j.jpowsour.2010.06.003>
- Fergus, J. W., "Sealants for solid oxide fuel cells", *Journal of Power Sources*, Vol. 147, No. 1-2, (2005), 46-57. <https://doi.org/10.1016/j.jpowsour.2005.05.002>
- Weil, K. S., "The state-of-the-art in sealing technology for solid oxide fuel cells", *JOM*, Vol. 58, No. 8, (2006), 37-44. <https://doi.org/10.1007/s11837-006-0052-6>
- Chou, Y. S., Stevenson, J. W., Chick, L. A., "Ultra-low leak rate of hybrid compressive mica seals for solid oxide fuel cells", *Journal of Power Sources*, Vol. 112, No. 1, (2002), 130-136. [https://doi.org/10.1016/s0378-7753\(02\)00356-7](https://doi.org/10.1016/s0378-7753(02)00356-7)
- Ghosh, S., Sharma, A. D., Kundu, P., Basu, R. N., "Glass-based Sealants for Application in Planar Solid Oxide Fuel Cell Stack", *Transactions of the Indian Ceramic Society*, Vol. 67, No. 4, (2008), 161-182. <https://doi.org/10.1080/0371750x.2008.11078652>
- Goel, A., Pascual, M. J., Ferreira, J. M., "Stable glass-ceramic sealants for solid oxide fuel cells: influence of Bi_2O_3 doping", *International Journal of Hydrogen Energy*, Vol. 35, No. 13, (2010), 6911-6923. <https://doi.org/10.1016/j.ijhydene.2010.04.106>
- Aniseh, N., Rezvani, M., Ghahremanzadeh, H., Tabean, S., "Investigation of crystallization and sinterability properties of $\text{BaO-SiO}_2\text{-Al}_2\text{O}_3$ glass-ceramics containing K_2O and B_2O_3 ", *Advanced Ceramic Progress*, Vol. 1, No. 3, (2015), 1-10. <https://doi.org/10.30501/acp.2015.70005>
- Lee, H., Kim, U. S., Kim, S. D., Woo, S. K., Chung, W. J., " $\text{SiO}_2\text{-B}_2\text{O}_3\text{-BaO-WO}_3$ glasses with varying Al_2O_3 content as a sealing material for reversible solid oxide fuel cells", *Ceramics International*, Vol. 46, No. 11, (2020), 18256-18261. <https://doi.org/10.1016/j.ceramint.2020.04.148>
- Bhattacharya, S., Shashikala, H. D., "Effect of BaO on thermal and mechanical properties of alkaline earth borosilicate glasses with and without Al_2O_3 ", *Physica B: Condensed Matter*, Vol. 571, (2019), 76-86. <https://doi.org/10.1016/j.physb.2019.06.065>
- Milhans, J., Khaleel, M., Sun, X., Tehrani, M., Al-Haik, M., Garmestani, H., "Creep properties of solid oxide fuel cell glass-ceramic seal G18", *Journal of Power Sources*, Vol. 195, No. 11, (2010), 3631-3635. <https://doi.org/10.1016/j.jpowsour.2009.12.038>
- Chou, Y. S., Stevenson, J. W., "Mid-term stability of novel mica-based compressive seals for solid oxide fuel cells", *Journal of Power Sources*, Vol. 115, No. 2, (2003), 274-278. [https://doi.org/10.1016/s0378-7753\(03\)00020-x](https://doi.org/10.1016/s0378-7753(03)00020-x)
- Stephens, E. V., Vetrano, J. S., Koepfel, B. J., Chou, Y., Sun, X., Khaleel, M. A., "Experimental characterization of glass-ceramic seal properties and their constitutive implementation in solid oxide fuel cell stack models", *Journal of Power Sources*, Vol. 193, No. 2, (2009), 625-631. <https://doi.org/10.1016/j.jpowsour.2009.02.080>
- Mahapatra, M. K., Lu, K., "Glass-based seals for solid oxide fuel and electrolyzer cells—a review", *Materials Science and Engineering: R: Reports*, Vol. 67, No. 5-6, (2010), 65-85. <https://doi.org/10.1016/j.msere.2009.12.002>
- Yang, Z., Xia, G., Meinhardt, K. D., Weil, K. S., Stevenson, J. W., "Chemical stability of glass seal interfaces in intermediate temperature solid oxide fuel cells", *Journal of Materials Engineering and Performance*, Vol. 13, No. 3, (2004), 327-334. <https://doi.org/10.1361/10599490419298>
- Batfalsky, P., Haanappel, V. A. C., Malzbender, J., Menzler, N. H., Shemet, V., Vinke, I. C., Steinbrech, R. W., "Chemical interaction between glass-ceramic sealants and interconnect steels in SOFC stacks", *Journal of Power Sources*, Vol. 155, No. 2, (2006), 128-137. <https://doi.org/10.1016/j.jpowsour.2005.05.046>
- Yang, Z., Meinhardt, K. D., Stevenson, J. W., "Chemical compatibility of barium-calcium-aluminosilicate-based sealing glasses with the ferritic stainless steel interconnect in SOFCs", *Journal of the Electrochemical Society*, Vol. 150, No. 8, (2003), A1095. <https://doi.org/10.1149/1.1590325>
- Heydari, F., Maghsoudipour, A., Hamnabard, Z., Farhangdoust, S., "Mechanical properties and microstructure characterization of zirconia nanoparticles glass composites for SOFC sealant", *Materials Science and Engineering: A*, Vol. 552, (2012), 119-124. <https://doi.org/10.1016/j.msea.2012.05.019>
- Sasmal, N., Garai, M., Karmakar, B., "Influence of Ce, Nd, Sm and Gd oxides on the properties of alkaline-earth borosilicate glass sealant", *Journal of Asian Ceramic Societies*, Vol. 4, No. 1, (2016), 29-38. <https://doi.org/10.1016/j.jascer.2015.11.002>
- Dev, B., Walter, M.E., Arkenberg, G.B., Swartz, S.L., "Mechanical and thermal characterization of a ceramic/glass composite seal for solid oxide fuel cells", *Journal of Power Sources*, Vol. 245, (2014), 958-966. <https://doi.org/10.1016/j.jpowsour.2013.07.054>
- Bansal, N.P., "Celsian formation in fiber-reinforced barium aluminosilicate glass-ceramic matrix composites", *Materials Science and Engineering: A*, Vol. 342, No. 1-2, (2003), 23-27. [https://doi.org/10.1016/s0921-5093\(02\)00313-1](https://doi.org/10.1016/s0921-5093(02)00313-1)
- Anstis, G.R., Chantikul, P., Lawn, B.R., Marshall, D.B., "A

- critical evaluation of indentation techniques for measuring fracture toughness: I, direct crack measurements”, *Journal of the American Ceramic Society*, Vol. 64, No. 9, (1981), 533-538. <https://doi.org/10.1111/j.1151-2916.1981.tb10320.x>
24. Oliver, W.C., Pharr, G.M., “An improved technique for determining hardness and elastic modulus using load and displacement sensing indentation experiments”, *Journal of materials research*, Vol. 7, No. 6, (1992), 1564-1583. <https://doi.org/10.1557/jmr.1992.1564>
25. Meinhardt, K.D., Kim, D.S., Chou, Y.S., Weil, K.S., “Synthesis and properties of a barium aluminosilicate solid oxide fuel cell glass-ceramic sealant”, *Journal of Power Sources*, Vol. 182, No. 1, (2008), 188-196. <https://doi.org/10.1016/j.jpowsour.2008.03.079>



Bioabsorbable Screws for Anterior Cruciate Ligament Reconstruction Surgery: A Review

J. Esmailzadeh ^{a*}, H. Setayesh ^b

^a Department of Materials and Chemical Engineering, Esfarayen University of Technology, Esfarayen, North Khorasan, Iran

^b Department of Materials and Metallurgical Engineering, Faculty of Engineering, Ferdowsi University of Mashhad, Mashhad, Razavi Khorasan, Iran

PAPER INFO

Paper History:

Received 17 April 2020
Accepted in revised form 08 July 2020

Keywords:

Anterior Cruciate Ligament
Reconstruction
Bioabsorbable Screws Mechanical
Properties
Biological Properties

ABSTRACT

One of the popular orthopedic implants is utilizing fixation screws to fix Anterior Cruciate Ligament (ACL) grafts and secure the graft into femur and tibia. Currently, these screws are made of titanium or bioabsorbable materials. In this respect, bioabsorbable screws were generated in order to overcome some of the potential problems caused by metallic screws. Although the bioabsorbable screws are susceptible to some drawbacks including bone ingrowth features as well as good in vitro and in vivo mechanical properties. The biomechanical results of ACL screws showed that the ultimate failure loads and yield point loads varied from 800-1500 N and 600-1000 N, respectively. Moreover, the evaluations of in vivo degradation behavior showed the almost complete or fully complete resorption of ACL screws from 6 month to 2 years. However, it was proved that the addition of bone mineral phases such as Hydroxyapatite (HA), β -Tricalcium Phosphate (β -TCP), and Calcium Carbonate (CC) could enhance this degradation rate. Incorporation of biceramics into pure polymeric ACL screws may contribute to enhancing the osteogenesis of bone after full resorption of screws, function as buffering agents that decrease the acidity of screw adjacents resulting from degradation of products, and improve the mechanical properties of ACL screws. In this paper, the latest bioabsorbable ACL screws which are currently available for graft fixation in orthopedic markets are discussed. A brief review of the literature regarding the physical, biological, and mechanical properties of bioabsorbable ACL screws was made. Besides, the insertion technique, various manufactured sizes, and in vitro and in vivo mechanical properties for each screw were addressed.

1. INTRODUCTION

In orthopedic surgery, biomaterials such as metals, ceramics, polymers, and composites are used as implants which are well compatible with living body tissues [1]. For many years, various metal alloys have been extensively used to fix the fractured bone or soft tissue rupture due to their desired mechanical properties and at the same time, their own proper biocompatibility [2]. Common orthopedic alloys are stainless steel, cobalt-chrome, titanium, and magnesium alloys [3]. Bone is a dynamic and complex live tissue that provides the body with the required mechanical endurance and has an elastic modulus of 10 to 30 GPa [4]. Among all of orthopedic devices used for fixation and preservation of damaged bone or soft tissues in order to restore their functions, Anterior Cruciate Ligament Reconstruction (ACLR) screws are one of the most popular orthopedic devices. The stability of knee joint is provided by four

extremely strong ligaments: ACL and Posterior Cruciate Ligament (PCL) prevent the tibia from slipping in sagittal planes; Medial Collateral Ligament (MCL) and Lateral Collateral Ligament (LCL) prevent the knee from bending in coronal plan. Among them, ACL tearing is one of the most common injuries (11 to 33% in different series) which is prevalent among athletes or patients with high activity. Fixing the graft into bone tunnel is a substantial step during the ACL reconstruction surgery. In this regard, the graft is threaded and compressed into bone pilot drilled hole by interference screws. There are two different types of ACL screws: metallic and degradable polymer-based screws. Use of metallic screws are regarded as the standard graft fixation method [5, 6]. The first ACL interference screws made of titanium alloys with a relatively sharp thread were utilized to provide a good anchorage of BPTB grafts into bone tunnel [7].

* Corresponding Author Email: Esmailzadehj@esfarayen.ac.ir (J. Esmailzadeh)

Such screws were first introduced by Lambert [8] in 1983 and then, popularized by Kurosaka et al. [9]. However, titanium screws provide high initial strength and well integration into the adjacent bone due to good biocompatibility; in some cases which need to be revised, the screw removal is known as a challenging issue [10,11]. The advantages of metallic ACL screws are solid fixation and well toleration on behalf of the body, while some of their drawbacks are their interferences with any applied probable Magnetic Resonance Imaging (MRI) following the surgery [1] and their potential interferences with any future surgeries on the knee such as ACL reconstruction, which may cause the laceration of the graft during insertion [12,13]. Currently, many attempts have been made to replace the retained unneeded foreign body materials into body by biodegradable and bioabsorbable ones. Bioabsorbable ACL screws could disappear when they are no longer needed. These categories of ACL screws are capable of overcoming some of the potential problems prevalent in metallic ACL screws. However, bioabsorbable ACL screws have their drawbacks including their fragility during insertion or inflammatory reactions [7]. Therefore, preserving the mechanical and biological properties of materials during the graft healing process is a crucial challenge. Bioabsorbable interference screws were first introduced for arthroscopic ACL reconstruction applications in the early 1990s [14]. More recent interference screws are made of biodegradable polymers or polymer/ceramic composites [2]. Different combinations of synthetic materials used as the major components of biodegradable ACL screws are Polylactic Acid (PLA) and its various enantiomers, Poly-L-lactic Acid and Poly-D-lactic Acid, Polyglycolic Acid (PGA), and copolymers of PGA/PLA. While PLA, the mainly used material, is characterized by a longer resorption time (yearly basis), the resorption takes a shorter amount of time for the PGA and PGA/PLA copolymers (monthly basis). Currently, various commercial ACLR screws are characterized by different mechanical and biological properties owing to their different chemical composition contents. These screws are usually fabricated by several companies. While substantial biodegradable polymeric ACL reconstruction screws are commonly made of biodegradable polymeric components such as PLA and its enantiomers, PGA, PLC, and some other screws have a bioceramic osteoconductive and osteoinductive fillers such as HA, BCP, TMC, β -TCP, and bioactive glass. Table 1 presents a list of some of these screws containing different polymers and copolymers formulation and those containing osteoinductive and osteoconductive filler phase. The present study aims to present a whole series of commercial ACLR screws regarding their material compositions, in vitro and in vivo studies, biodegradation behavior, and mechanical and physical properties. The hypothesis here suggests

that this collection can promote scientific research since such an issue has not been previously elaborated in the literature.

2. ANTERIOR CRUCIATE LIGAMENT RECONSTRUCTION SCREWS

In orthopedic surgery, ACLR is performed by interference screws to maintain ligament inside the bone until the tissue is remodeled. These screws are fixed into a space between the bone plugs and drilled tunnel walls. These kinds of screws are available in different sizes to meet the patient's requirements. To ensure that the screws are implanted at the appropriate angle and direction, a wire with a proper diameter is used is drawn from the inside of the screw and drill hole (Figure 1) [15]. Currently, several companies manufacture reconstruction screws used in ACL surgeries. While most commercial screws have a similar hollow socket to drive the screws, significant differences in their designs make the distinctions between different companies. For example, some parameters that usually differentiate a company's products are the diameter or length size, screw tapering, threads geometry, thread pitch, and material type. The materials used to make the screws is among those criteria that make the difference. Conventional reconstruction screws are usually made of Titanium due to its biocompatibility and acceptable mechanical and physical features; however, in the past decade, other compounds were also developed. New screws are mainly characterized by their absorbable materials in compositions that are degraded into the body, while the metal ones will remain permanently within the bone [16]. However, the probability of inherent problems caused by the absorbable interference screws for ligaments and tendon reconstructions has not been entirely proven yet.

It should be noted that a harmonic trend of the mechanical properties of loosening due to degradation of screw constructs and tendon healing process is a significant issue. Therefore, if the metal screws are replaced by biodegradable ones, it must show adequate fixation for at least 6–8 weeks until the bone block has been incorporated and biological fixation has been achieved [17,18]. It can be found that the almost whole bioscrews composed of synthetic polymers such as PLA, PGA, etc. have acid-based ingredients. While these screws that are exposed to aqueous medium into the body and reabsorbed by hydrolysis and their products dissolve in water forming liquid acids. In a specific area with good blood supply within the body, the acid is well buffered and metabolized; however, in areas with poor blood supply such as bone, the pH of the screw-adjacent medium can be quite low. A decrease in pH of the adjacent tissue results in an

accelerating rate of screw degradation, tissue damaging, and bone destruction.

This is the reason why manufacturers, in some cases of ACL screws, have added bioceramics such as hydroxyapatite and tri-calcium phosphate into the material formulations. These materials could promote the osteoconduction and osteinduction characteristics of screws and neutralize the screw-adjacent acidic medium caused by acidic products of screw degradation resulting from the alkaline ions release.

In addition to screw formulation, various other parameters including component composition, size of acidic crystals, screw geometry, and manufacturing method were identified that would influence the behaviors of screws in implant sites. Thus, all bioscrews are not equal and do not behave the same, even if they have been made from the same materials at different implants [19].

TABLE 1. Current commercial Bioabsorbable screws

Manufacturer	Composition	Bioabsorbable Screws
Inion Ltd.	PDLLA/Tri-methylenecarbonate (TMC)	Inion Hexalon
Smith &Nephew	PGA/Tri-methylenecarbonate (TMC)	EndoFix
	PGA-co-PDLLA/Calciumcarbonate (CC)	Calaxo
DePuyMitek, Inc.	PLLA/ β -Tricalciumphosphate (β -TCP)	Bio-IntrafixBiocryl
ArthroCare Corporation		Bilok
DePuyMitek, Inc.	PLGA/ β -Tricalciumphosphate (β -TCP)	Milagro
ConmedLintratec	PDLLA/ β -Tricalciumphosphate (β -TCP)	Osteo ACL Screw
	SR-PDLLA/ β -Tricalciumphosphate (β -TCP)	Matryx
Smith &Nephew	PLLA/Hydroxyapatite	Biorci-HA
Stryker		Biosteon
Arthrex, Inc.	PDLLA/Biphasic calciumphosphate (BCP)	BioComposite
ConmedLintratec	SR-PDLLA	SmartScrew
Bioscience, Ltd.	SR-PLLA	Biofix
CenterpulseMedicalAG	PDLLA	Sysorb
Biomet SportsMedicine, Inc.	PLLA-co-PGA	GentleThreadsBioCore
Karl Storz-EndoscopePhusis	PLLA-co-PDLLA	MegaFixPhusiline
Instrument Makar, Inc.	PGA-co-PDLLA	Biologically Quiet
Arthrex, Inc.	PLLA	Delta Tapered Bio-interference Screw
		Round Delta Tapered Bio-interference Screw
		Bio-interference Screw
		Biocortical Screw
		RetroScrew
		Full Thread

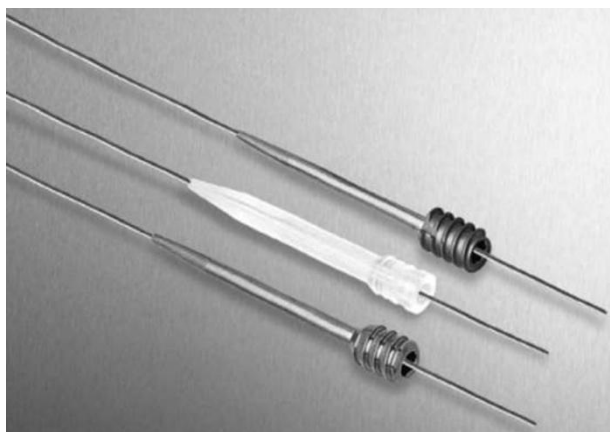


Figure 1. Example of guide wire of ACL reconstruction screws [15]

Of note, it has been reported that the tunnel widening for a poly-levodextro-lactide (PLDLA) and β -tricalcium phosphate composite screw did not occur [20], while this is a common occurrence for other series [21,22].

A study on a comparison of different combinations of absorbable interference screws showed that Poly L-Lactide (PLLA) was not completely degraded after 20 months of implantation. However, poly(DL-Lactide-co-glycolide) (PDLA-co-PGA) undergoes complete degradation during this period of time. Although no damage has been reported for poly(DL-Lactide-Acid) (PDLA) up to 6 weeks, it would be completely degraded within 10 months [23]. The degradation rate of ACL screws should be in agreement with the biological tissue growth. Bach et al. [24] evaluated the tissue growth surrounding the surgical site in ACLR with the screws made of 32.5% tri-methylene carbonate and 67.5% polyglycolide. This study conducted experiments on 20, 10, and 8 patients over 6, 12, and 24 months, respectively. The clinical and MR imaging results indicated that according to Figure 2(a-b), the screws were partially resorbed within 6 months and completely resorbed within 12 months; besides, according to Figure 2(c), these screws enlarged the bone tunnel as a result of screw replacement [24]. Another potential problem of absorbable interference screws is caused by their degradation. As the biodegradable screws breakdown, their molecules and components will be released, causing inflammatory reactions through the foreign body responses. These reactions may be either minor, releasing a small non-bacterial sinus, or significant which requires immediate attention. Although screws with long degradation time duration will cause fewer foreign body reactions, they will simultaneously require a longer period of time to complete the bone regeneration. However, it was observed in most cases that the body did not completely repel the screw until the emergence of foreign body reactions, hence the cysts formation and osteolysis [25].

Moreover, as reported in several studies, late inflammatory reactions appeared after ACL surgery. Morgan et al. [26] elaborated on the advantages of explants made of screw remnants, fibrous connective tissue, cortical-like bone, and cancellous bone due to PLLA interference screws after 30 months. Similarly, Park and Tibone [27] observed the persistence of tibial PLA interference screws 4 years past the ACL surgery, which was approved by MRI. However, under irrigation, no screw was found, probably due to late inflammatory reaction.

However, the new bone formation through replacement of ACL screws is only observed for bioscrews independent of its formulation with a slow rate of degradation manner in excess of 5 years [19, 28].

Several studies compared the biodegradable and metallic screws and suggested that bioabsorbable screws would provide good fixation like metal screws; therefore, these screws could be a rational alternative to metallic ones [29-35].

For example, on the comparison of bioabsorbable and metallic ACL reconstruction screws for graft fixation, a number of researchers have found no significant difference in the final patient outcomes in terms of clinical scores, clinical evaluation, and imaging assessments [32]. Moreover, in terms of the range of motions, the obtained comparative results of bioabsorbable and metallic screws for different fixations of grafts confirmed that there was no significant difference between the two groups in the long term, as seen in studies [29,33,36]. Concerning the functional outcomes, Rocco Papalia et al. [37] found no differences between the two types of screws.

3. ACL RECONSTRUCTION SURGERY

ACL injuries are very common, with around more than 4 million reconstruction and healing surgery every year all over the world [38]. This type of injury may occur due to severe knee blowing, sudden stopping, sudden turning, or severe stretching. Individuals who play sports like skiing, football, and basketball are more prone to ACL ligament injury than any other groups [39]. When an ACL injury occurs, the injured usually hear a pop sound, followed by a mild pain that causes swelling in the affected area [15]. The diagnosis of quick ACL tearing is performed by asking the patient to relax his/her legs and the doctor pulls the patient's legs forward to see if the bone is limited to moving in the anterior direction or not; this test is called the Lachman displacement test [15]. Now, if the bone has no limitation in displacement, it can be concluded that the ligament is torn. In this case, MRI can easily determine the ACL rupture. Reconstruction of the ACL involves the replacement of the old ligament by a tissue graft and is usually harvested from the hamstring tendon or

patellar tendon [15]. Harvesting of the graft is the first part of the ACL surgery. In the case of patellar, the surgeon creates an incision on the patellar which is of less importance. In the following, the central part, the attached and cylindrical portions of the tendon are removed outside the femoral and tibia head, so-called bone plugs. The end of the remaining tendon is sutured to regrow and continue to perform its duties. After the graft harvesting, sutures are added to the bone part of graft used in placing the tendon. Then, the remains of ACL are removed from the knee and pierces of the inter condylar notch burred away so that the surgeon will have a chance to reach the correct placement of the tendon. To complete the perforation, the surgeon creates two holes in the upper part of tibia and the lower part of the femur near the knee (Figure 3) [15]. To create each of these holes, a small hole is initially created by a small diameter drill to increase the accuracy of perforation and then, by a drill with a diameter similar to the cylindrical bone plug. After the holes are smoothed, the sutured end of the graft is inserted to the knee through tibia head, while the other end is pulled out from the femoral head [15]. The graft is tightened using the interference screws. The biodegradable interference screws keep the tendon firm within the bone (Figure. 4) [15]. After the surgery, the patient will have a fairly moderate pain and difficulty bending and extending the knee. In addition, postoperative activities are limited and a hard rehab program must be tolerated to be restored. Since the graft is gradually becoming a tendon, the postoperative activities should be limited to be well applied. During this process, the graft is very weak and the knee is partially unstable. The emergence of a tear is possible in case such activities are intense and uncontrolled. Setting a limit on these activities is absolutely necessary because the graft is only kept by an interference screw. Therefore, as the graft is being pulled by the tibia and femoral bone, the screw will be pulled out of the hole. This scenario may also lead to another reconstruction.

4. BIOABSORBABLE POLYMERIC ACL SCREWS

4.1. PLLA-BASED ACL SCREWS

Among the biopolymers that belong to poly (α -hydroxy acids) family, PLA is extremely well known and widely studied. PLLA is a kind of PLA enantiomer that is a common biodegradable polymer used in the compositions of ACL fixation screws. They go through a degradation process mainly due to the hydrolysis mechanism. Throughout the degradation, water diffuses into the structure which leads to a break in the long chains and changes them to small oligomers that can diffuse inside and outside of the polymeric matrix. These degradation products can be eliminated from the

human's body through the Krebs cycle (using urination or CO₂ gas during breathing) [40].

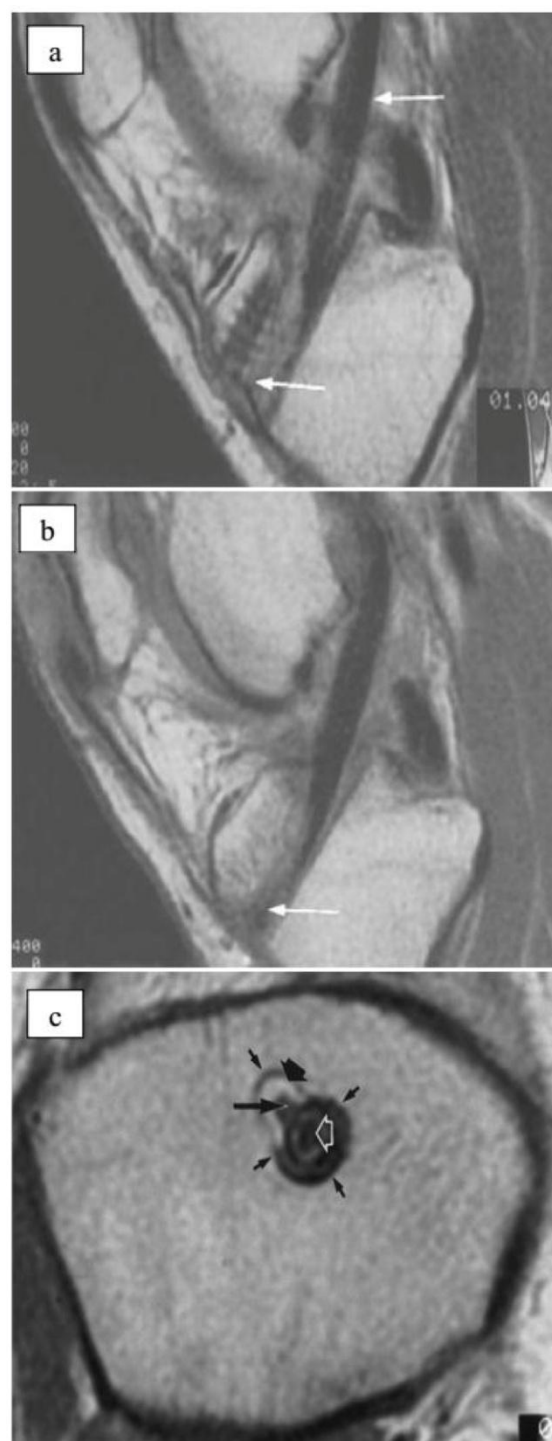


Figure 2. a) Magnetic Resonance Images (MRI) of partial resorption of interference ACL screws at 6 month following implantation, b) total resorption at 12 month following implantation, and c) implantation tunnel after total resorption. New tissue formed around the bone plug (open arrow) determined fibrous tissue (long skinny arrow) with fatty tissue surrounding it (thick short solid arrow) [24]

PLLA molecular weight varies due to its manufacturing technique; for instance, PLLA with high molecular weight (>100 kDa) has a melting point around 137 °C to 178 °C and T_g temperature of 58 °C. Although PLLA is totally semicrystalline, its injection molding also makes nanocrystalline products, leading to a biomaterial whose modulus drops above the glass transition temperature [41]. In order to enhance the PLLA mechanical properties, an alternative strategy called self-reinforced polymer composites can be implemented. The fiber reinforcement in these materials is a highly orientated version of the same polymer from which the matrix is made [42]. For example, a PLLA matrix is reinforced with highly orientated PLA fibers.

Several studies reported the in-vitro results of PLLA-based screw degradation rate as well as body responses. In most of these screws, foreign body reaction during 20 to 30 months after the implantation indicated little or no evidence of inflammatory reaction within the implant environs. In some cases, body responses to screws offer little evidence of adverse inflammatory reaction which is related to the degradation of cartilage or loosening of knee joint envious especially in cases with retardation of screw degradation. Fixation strength of a biodegradable PLLA interference screw (Arthrex, Naples, FL) was compared with press-fit fixation and a titanium interference screw in ACLR using a Bone-Patellar Tendon-Bone (BPTB) graft. The results showed that there was no significant difference between the ultimate failure load of PLLA (805.2 N; range 680 to 995 N) and titanium interference screws (768.6 N; range 544 to 1094 N) [43]. The mechanical behavior of delta tapered bio-interference screws (PLLA nanocrystalline, Arthrex) as quadriceps hamstring tendon fixator was dynamically tested. It was found that the ultimate failure load and displacement at the break point of screws were 647 ± 200 and 10.91 ± 4.4 mm, respectively. The screws obtained their toughness of 64.54 ± 22.1 N/mm [44]. The biomechanical properties of Retro screws (Arthrex, PLLA) for tibial called anterior graft-tibial tunnel fixation were also obtained. The Retro screw displays superior toughness (114.1 ± 23.3 N/mm) and displacement (18 ± 0.5 mm) during cyclic testing. During load-failure testing, the maximum load of Retro screw failure was 787 ± 177.5 N. The displacement and toughness of bioscrew resulting from the pull-out test were 5.3 ± 2 mm and 204.4 ± 52.9 N/mm, respectively [45]. In another study on BPTB fixation Bioscrews (PLLA, Conmed Linvatec, Largo, FL) implanted into a cadaver, the results illustrated that the mean load to failure was 189 ± 118 N [46]. The fixation strength of BioFix screws (Self-reinforced (SR)-PLLA, Bio Science, Ltd, Tempere, Finland) in a BPTB graft within the bovine knee is 1211 ± 362 N and its elastic moduli in upper (>500 N) and lower (<500 N) range loads are 304 ± 71.8 N and 189 ± 47.4 N, respectively [47]. There is no significant difference between these biodegradable

screws and metal screws in the BPTB graft fixation in the bovine knee; therefore, they can be recommended regarding ACL reconstruction using this type of graft. The mechanical properties of BIORCI screws (PLLA, Smith & Nephew, Andover, MA) for hybrid femoral fixation were investigated. The Ultimate Tensile Strength (UTS) of these screws was 643.5 ± 148.4 N and their toughness was reported as 315.7 ± 38.9 N/mm [48]. The initial fixation strength of two types of biodegradable screws consisted of Poly-L-Lactide/Tri-Calcium Phosphate (PLLA/TCP); one suspension screw (Bilok ST) with a diameter of 9 mm and length of 35 mm and the other interference screw (Bilok TS) with a diameter of 9 mm and length of 30 mm, determined in the hamstring reconstruction of ACL using bovine knees. The single-cycle test results showed that the maximum failure load, yield load, and stiffness were $1475.8 (\pm 315.3)$ N, $998.5 (\pm 122.56)$ N, and $248.1 (\pm 76.1)$ N/mm, respectively, in suspension screws group. For interference screws, the maximum failure load, yield load, and stiffness were measured $651.1 (\pm 155.4)$ N, $537.8 (\pm 86.7)$ N, and $199.5 (\pm 82.9)$ N/mm, respectively [49].



Figure 3. Creation of implantation holes at tibia and femur [15]

4.2. PDLLA-BASED ACL SCREWS

PDLLA is a copolymerization product of PLLA and PDLA as two enantiomers of PLA. Different mechanical properties of PDLLA are related to the composition percentage of each enantiomer. PDLLA is usually amorphous and has a glass transition temperature of about 56°C. In vivo results of PDLLA screws demonstrated that these screws would not be degraded at least for 6 weeks, but they would be completely absorbed by the body in 10 months [50]. All PDLLA, PLLA, and PGA copolymers could provide different mechanical properties together and none of them has this capability by itself. For example, the glass transition temperature of PDLLA/PGA blend with 50:50

portions is about 30°C and increasing the PDLA: PGA ratio from 65:35 to 75:25 leads to an increase in the T_g temperature from 33.3°C to 38°C [51]. A blend of PDLA and PGA with the ratio of 82:18 (Lactosorb, Biomet sport medicine, Inc., Warsaw, In) can provide a nanocrystalline copolymer with a temperature of 55.3°C T_g . It was found that a 2°C increase in T_g temperature would significantly increase the hydrolysis degradation rate of lactosorb from 20% to 25% [52]. Moreover, blending PDLA with 10, 20, and 30% wt of PCL phase decreased T_g PDLA from 67.3°C to 66.2, 65.1, and 63.5 °C, respectively [53].



Figure 4. Creation of secure fit by holding of screw between the graft bone plug and the wall of the drilled hole [15]

PDLA/PCL blends reinforced with Bioactive Glass nanoparticles (BGn) showed that the addition of BGn improved the initial mechanical properties as well as biological activity [54].

Phusilin biodegradable interference screws (poly-D(2%), L(98%)-lactide, Phusis, Saint-Ismier, France) are used in patella tendon autograft fixation. The results of an average follow-up of 24 months showed that screws were degraded while bone in-grows earlier than an individual PLLA screw. Clinical tests and MRI results showed no adverse complications during screw insertion thanks to its degradation [52]. The tin octoate is commonly used as an initiator of PDLA polymerization; however, in order to decrease body immune response to implant screws in phusilin screws, polymerization process is applied to ring-opening procedure using zinc catalyst, which consists of less toxic material. Ring-opening polymerization that uses zinc as a polymerization initiator creates a combination of stereoisomers by means of ionic reactions. In this case, the resulting screws are more hydrophilic than the PLA screws derived from tin and can create interference screws with quicker degradation [52].

Bioabsorbable interference screws (Sysorb; Sulzer Orthopedics, Baar, Switzerland) are used for autologous

BPTB fixation through the press-fit technique and distal bone block in 25 patients. The results showed that no replacement of sysorb screws in tibial tunnel took place by osseous neo-formation up to 8 months after ACLR surgery, excluding one performed on tibial bone tunnel enlargement and tibial subcutaneous cyst [55]. Mechanical evaluations of Sysorb screws used for BPTB graft fixation in cadaver indicated that the maximum pull-out force and toughness were 544 ± 109 N and 162 ± 27 N/mm, respectively. Cyclical loading elongation also showed that during the first five cycles, 5th-20th, and 20th-1500th loading cycles, the amounts of elongations reached 1.4 mm, 0.14 mm, and 4.1mm, respectively [56].

Biological ACLR screws (85/15 PDLA/PGA, Instrument Maker, Inc., Okemos, MI) revealed some pieces of evidence of total screw degradation, bone remodeling, and new bone formation in femoral and tibial bone tunnel throughout a two-year follow-up. Moreover, MRI results showed no cystic or osteolytic changes associated with minimum swelling at the implant site [57]. Studies of biodegradable screws megfix (70/30 PLLA-PDLA, Storz-Endoscope Tuttlingen, Germany) with three different diameters of 6, 7, and 8 mm implanted in porcine knee showed that none of 6mm screws, 3 of 7 mm screws, and all the 8 mm screws were able to tolerate cyclical loading protocol. Elongations after 1000 cyclic load achieved 8.36 and 4.26 mm for 7 mm and 8 mm screws, respectively. The maximum load, yield strength, and toughness for 7 mm screws were 245 N, 199.1 N, and 98.6 N/mm, respectively. These values for 8 mm screws were 567 N, 456.9 N, and 151 N/mm, respectively [58].

4.3. POLYMER/TRI-METHYL CARBONATE (TMC) ACL SCREWS

TMCs with elastic properties similar to rubbery polymers are not appropriate for biomedical application, because they are characterized by poor dimensional stability, tackiness, and inadequate mechanical properties [59]. However, the combination of TMC and other polymers like PGA, PLLA, and PDLA could create interesting biomechanical properties that will be favorable for particular applications. As an example, Polyglyconate is a block copolymer of glycolic acid and TMC linked together by covalent bonding. Copolymers of PGA and TMC have more flexibility than PGA alone. In vitro studies have shown that the molecular weight of unirradiated PGA cultured in PBS solution decreased from 124 kDa to 18.6 kDa for 31 days. The ultimate tensile strength of unirradiated PGA falls down from 51.7 MPa to 5.7 MPa after 3 weeks [60]. However, results of in vivo studies of polyglyconate implants revealed that their mechanical properties and integrity disappeared within 6 weeks and the full resorption of implant took place within 6 to 12 months [61]. Comparative in vivo studies were performed on 20

patients who had femoral bone block fixation with a bioabsorbable interference screw (EndoFix absorbable interference screw; Smith & Nephew Endoscopy, Andover, MA) and tibial bone block fixation with a titanium screw. The follow-up results of 3, 6, 12, and 24 months indicated no problem and complications related to graft fixation took place for bioabsorbable as well as titanium screws. Upon the point of 12 months, degradation of the implant was complete, whereas there was no radiological evidence of bony replacement up to 3 years postoperation [30]. ACL hexagon Inion screws (PDLLA- TMC, Inion Ltd., Tampere, Finland) illustrated that they preserved 70% to 90% of their initial strength during 12 weeks and considerable degradation during 18 to 36 weeks, whereas complete degradation took place up to 2 years, post operation [62]. MRI results of 2 follow-up years indicated that the screw degraded bone tunnels replaced by fibrosis like tissues. Initial fixation strength of Hexalon Inion screws was evaluated at three separate levels in comparison to (i) interference metallic screws for fixation of soft tissue graft, (ii) smart self-reinforced screws for fixation of soft tissue grafts, and (iii) PLLA bioscrews used for fixation of bone-tendon-bone grafts. Yield loads of Hexalon Inion screws in each experiment were obtained as 491 N, 501 N, and 901 N, respectively [63,64]. Hence, researchers found that the strength of Hexalon Inion screws was similar to that of other polymeric and metallic screws .

5. BIOACTIVE AND BIOABSORBABLE COMPOSITE ACL SCREWS

5.1. EFFECTS OF BONE MINERAL PHASES IN ACLR SCREWS

Incorporation of various inorganic phases such as calcium carbonate (CC), β -tricalcium phosphate (β -TCP), and hydroxyapatite (HA) into ACLR screws compositions could overcome some shortcomings of other polymeric ACLR screws. Addition of these phases to ACLR screw compositions could enhance the absorption rates of bioabsorbable screws, treat osteogenesis after absorption, reduce oxidation, and act as buffering agents to reduce the acidity of screw adjacent resulting from the decomposition products of screws based on polymers with the acidic origin.

A comparative clinical and radiological study was conducted on 349 patients between 2 different tibial fixations performed using bioabsorbable poly-L-lactide (PLLA) and PLLA-HA ACL screws. The results showed that the PLLA-HA screw groups would induce a significant reduction in the tibial tunnel widening and foreign body reactions, improving the osteointegration and significantly increasing screw resorption compared to the pure PLLA group [65]. The proximal tibial tunnel widening effects of PLLA groups revealed a positive

correlation with knee laxity. Hunt and Callaghan carried out an in vitro animal study to compare a composite (PLLA-HA) with PLLA screw. They concluded that the composite screw significantly increased new bone formation and decreased inflammatory reactions in comparison with the PLLA screw [66]. The Computed Tomography (CT) evaluations demonstrated that the pure PLLA screws were completely degraded after 5 years with no evidence of osteoconductivity behavior, leaving bone void after degradation [67]. In the meantime, biocomposites screws made of PLLA (70%)/ β -TCP (25%) (Bilok, ArthroCare, Sunnyvale, CA) and copolymer of 70 % PLLA/PGA with 30% β -TCP (Milagro, DePuy Mitek) showed complete degradation and osteoconductivity at 75% and 81% of the screw sites and complete filling of screw void in 10% and 19% of tests, respectively [68].

It was found that the content of mineral bone phase could also affect the degradation rate of screws and osteoconductivity behaviors. Research on two different amounts (30% and 60%) of β -TCP evaluated using CT scans over 29 to 45 months showed that the biocomposite of PLLA/30 % β -TCP (Ligafix; SBM, Lourdes, France) exhibited more dominant osteoconductivity behavior than other screws containing 60 % β -TCP [69]. This is due to at least two reasons: (a) the screws with greater β -TCP content were absorbed more rapidly; (b) the screws with 30 % β -TCP could be completely surrounded by bone plug or tibial bone rather than screws containing 60% β -TCP [70]. The other theory in this respect depicts the greater release of phosphate ions into the adjacent screw during degradation by screws with high β -TCP, resulting in a greater pH which may play an inhibitory role in the osteoconductivity manners [70].

5.2. POLYLACTIDE CARBONATE ACL SCREWS

Calcium Carbonate (CC) is a bone mineral phase that forms other bone calcium salts. A combination of CC and other polymeric materials would create an osteoconductive interface that may provide enhanced degradation properties and stimulate its replacement by new bone formation [71]. The presence of calcium carbonate into implants could also provide pH value between 7.4 and 6.3 throughout the degradation process; help avoid local acidity formation [72]. An interference screw made from a novel bioabsorbable material, polylactide carbonate (PLC) (Calaxo Screw; Smith & Nephew Endoscopy, Andover, MA) is composed of PGA and PDLLA (65%) copolymers at ratio of 85:15 and 35% calcium carbonate. The combination of PDLLA-co-PGA and calcium carbonate is an appropriate composite material for ACLR screws. In vitro studies and molecular weight (M_w) changes surveying of calaxo screws into phosphate buffer saline (PBS, pH=7.36) for following up to 12 weeks was performed. The results suggested that the calaxo screws

lost 85% of its molecular weight, whereas pH of PBS also decreased to 6.86 [73]. Researchers found that the buffering effect of CC may lead to rapid degradation of screws. The *in vivo* studies of calaxo screws carried out by insertion of ACLR screws into 41 sheep. No inflammatory reaction was realized with a mean follow-up of 6, 12, 26, and 52 weeks after implantation into sheep body. Within 26 weeks after insertion, screws partially were replaced by new bone; however, in 52 weeks after implantation, they were resorbed completely, whereas they were simultaneously replaced with a new bone. The ultimate load to failure of these screws was identified 70 N and 225 N for 6 and 12 weeks after implantation, respectively [71].

5.3. POLYMERIC COMPOSITES ACL SCREWS WITH β -TRICALCIUM PHOSPHATE

Various companies designed the ACL screws made of polymer-based composites reinforced by osteoconductive and osteoinductive phases. For example, biodegradable screws contain PDLLA, PLLA, and PLGA as polymeric and β -tricalcium phosphate (β -TCP) as osteoinductive materials. β -TCP has brittle origin with low toughness, this means that the susceptibility of cracks formation throughout the brittle materials restrict the capability of these materials for load-bearing applications. These materials presented good osteoconductive properties and hydrolytic dissolution products of materials that contain calcium and phosphate ions [74]. Adding β -TCP to PLLA screws improved the mechanical properties and also observed that β -TCP caused an increase in both the degradation kinetics of the composite material, accelerating the remodeling and healing of bone. Moreover, β -TCP is alkaline in solution and may neutralize the acidic by-product resulting from PLLA degradation. A PLGA screw has more rapid degradation than PLLA one that can, in combination with β -TCP, provide a proper degradation profile as well as osteoconductive and osteoinductive properties due to the presence of TCP phase. There are some ACL screws composed of TCP phase. For example, Bio-intrafix screws made of 30% β -TCP and 70% PLLA [75]. *In vivo* studies of Bio-intrafix screws administered to the body of patients illustrated that no post-surgery adverse inflammatory reaction occurred up to 2 years. In addition, the ultimate tensile strength of Bio-intrafix screws indicated about 700 N [76]. In this respect, another screw is composed of 30% β -TCP and 70% PLGA (Biocryl, Rapide TM). Preclinical *in vivo* studies illustrated that the composite-based screws inserted into cortical femoral bone defect were completely degraded throughout 24 months and simultaneously replaced with a new bone [77]. Another *in vitro* studies on Biocryl screws were carried out in PBS solution with pH=7.36. The results showed that the dimensional variations of the screw occurred to some extent after 12 weeks from

culturing into PBS solution [73]. Throughout this time, molecular weight decreased to 66.9%, whereas pH almost unchanged. These results proved that TCP might increase the degradation rate of Biocryl screws. This may be due to the alkaline origin of TCP materials, which could make a buffering circumstance for acidic by-products resulting from screw degradation. These screws in another study were used as ACL screws in tibial bone tunnel enlargement. Tibial fixation was performed using 2 bioresorbable interference screws. Magnetic Resonance Imaging (MRI) was performed on all patients after 1 year post operation. The results determined an increase in bone tunnel enlargement up to 43% by digitally measuring the widths of the bone tunnel perpendicular to the long axis of the tunnels on an oblique coronal and axial planes. However, there is no report about the degradation profile of screws [78]. Another study investigated the biodegradable β -TCP-PLGA screws for fixation of ACL autograft patellar tendon inserted into 41 patients. During the follow-up 3 years, the post operative results illustrated that complete degradation accompanied by new bone formation occurred. The degradation rate of β -TCP-PLGA based screws was more than that of the β -TCP-PLLA screw [73].

5.4. POLYMERIC COMPOSITE SCREWS WITH HYDROXYAPATITE

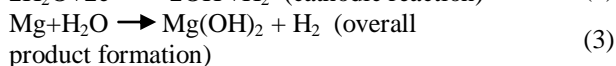
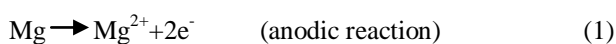
Hydroxyapatite (HA) similar to β -TCP is a bioceramic inorganic material and a major constituent of bone whose high biocompatibility has been widely used for bone remodeling [79]. Besides, HA can act as a buffering factor against acidic products resulting from PLLA degradation. Similar to β -TCP, HA suffers from low fracture toughness and also high brittleness. Elastic modulus of HA varied from 80 to 100 GPa and its compressive strength ranged from 500 to 1000 MPa [75]. *In vitro* studies of PLLA/HA composite material in PBS solution with pH= 7.36 were introduced such that no significant changes occurred throughout the 12 weeks; however, the molecular weight of screws decreased by about 22.9% and pH also slightly decreased from 7.36 to 7.32 [73]. Two biodegradable ACL screws, i.e., PLLA-HA composite screws and no composite PLLA screws, were compared. The results of evaluation studies showed that the remaining strength of HA-PLLA composite after 24 weeks is higher than PLLA screws. Modulus of composite screw was also more similar to that of natural bone tissue. This similarity between composite screws and natural bone tissue modulus causes a substantial decrease in stress shielding during the bone healing [80]. A study was performed on BIORCI-HA screws made of HA-PLLA composite for fixation of patellar tendon graft into 20 patients. Based on MRI images of screws inserted into the body, no complication during the 2-year follow-up and inflammatory reaction at patellar tendon graft were

observed. Although the degradation rate of screws and bone integration were slow based on MRI, it should be noted that in this study, screw failure during insertion was just reported in one patient [81].

6. MAGNESIUM AND MAGNESIUM ALLOYS AS POTENTIAL BIODEGRADABLE ACL SCREWS

Non-degradable titanium interference screws may impair the tendon or ligament graft throughout the screw insertion. This may be due to high mechanical strength. Besides, these screws need a second surgery for removal. In the case of bioabsorbable ACLR screws as a well-established practice, there also are some complications. As an example, due to inadequate mechanical strength, the screw may fail upon insertion. In addition, during the degradation process, some adverse reactions such as synovitis, granuloma, and tunnel enlargement may occur, retarding the healing of tendon grafts by fibrous scar tissue layer formation at the tendon-bone interface [82,83]. In this respect, biodegradable metallic screws with modulus resembling the natural bone can be a proper choice. Recently, magnesium (Mg) and Mg alloys represented an interesting potential for biomedical application and may be suitable for tendon graft fixation in ACLR reconstruction as a new generation of bioactive implants [38,84-85]. These screws could stimulate fibrocartilage regeneration. Additionally, these types of screws possess a good mechanical behavior owing to their similarity in modulus between Mg (41-45 GPa) and natural bone (15-25 GPa) [86], which could meet strength requirements throughout the insertion into bone. Mg metal could be degraded when exposed to the aqueous solution. Its degradation is initiated by chemical reaction with body fluid and release of the Mg ions and equivalent mole of hydrogen gas.

Generally, Mg is firstly oxidized throughout the anodic reactions to formations and then, throughout a cathodic reaction, the water of body fluid is reduced by the generated electrons during the last levels. Furthermore, $Mg(OH)_2$ is formed as the overall products. Dissolution of passive $Mg(OH)_2$ layers in the presence of destructive biological ions such as Cl^- ions occurs according to Equation 4. Furthermore, the degradation of Mg implants into body environments including Cl^- ions is dominant because the degradation rate of the passive layer is higher than that of degrading products on the surface [87].



Since the Mg ions have a stimulating role in osteogenic differentiation of stem cells, it could promote the osseous ingrowth into graft as well as the incorporation of tendon graft into the surrounding bone tissue enhancement [88]. Most recently, Cheng et al. introduced the high purity Mg as promising materials for use of interference ACL screws [23]. They also expressed that Mg interference screws could effectively inhibit the degeneration of the tendon graft by reducing the expression level of MMP-13, while the remodeling phase occurred. This fact indicates that more collagen fibers in the tendon graft were preserved to connect the surrounding bone tissue for higher knee stability [89]. However, it has not been yet reported if Mg-based implants could also promote graft healing in tendon-bone healing in a bone tunnel [25]. Besides, there is no sufficient information about the bone tunnel after surgery to determine the potential application of Mg implants. Therefore, it seems that the investigation of graft healing quality into bone tunnel in ACLR reconstruction model is crucial. Herein, it was hypothesized that Mg-based interference screw could significantly enhance the incorporation of tendon graft within a bone tunnel when compared to conventional Ti interference screws.

7. MECHANICAL PROPERTIES OF ACLR SCREWS

The ACLR screws intend to fix ligament into tibial or femoral bones that must have sufficient mechanical strength when either inserted into the bone tunnel during surgery or fixed the ligament into the bone for a certain time until rehabilitation of damaged ligament is completed. Regarding the initial fixation strength of ACLR screws, many factors such as bone quality and its diameter and screw features such as length, diameter, design, and material compositions are affected. Moreover, the age of patients and surgery techniques affect the mechanical properties of implanted ACLR screws. In terms of screw geometry, there are many controversies with respect to the appropriate diameter and length of screws on mechanical strength. It was found that an increase in screw diameter could increase the fixation strength [90]. There is also hypothesized over the screw length effects on biomechanical properties. In one study, it was found that the significant improvement of the mechanical properties of BPTB units was made when they were fixed with a custom-designed 9 mm interference screw rather than a 6.5 mm cancellous screw [47]. Moreover, use of fully-threaded ACL screws has remarkably increased the fixation strength rather than partially-threaded screws [47].

In terms of material compositions, several attempts have been made to develop biodegradable ACLR screws with sufficient strength for the fixation of ligament or tendon

into bone tunnel. The weakness of graft fixation immediately and during the first six to eight weeks after surgery will limit early intensive rehabilitation [91]. In a study where the fixation strength of PLLA biodegradable screws compared with two metal screws, the results show that there is no significant difference among the three groups. Therefore, the mean forces to failures in the three groups of metal interference (n=11), an AO cancellous screw (n=11), and PLLA screws (n=11) were 1358 ± 348 N, 1081 ± 331 N, and 1211 ± 362 N, respectively [47].

Regarding screw insertion during operation, since the screw was submitted to torsional and axial loads owing to the application of compression and longitudinal shear forces [92], it has been reported that the biodegradable screws may be subjected to break during operation [93]. The technical standard ASTM F2502 (Standard Specification and Test Methods for Bioabsorbable Plates and Screws for Internal Fixation Implants) provides a standard test method for measuring the mechanical properties of polymer screws in torsion [94]. According to this standard, the fully threaded screw was equipped with the holding device so that five threads under the head of the screw were exposed outside the holding device. A large enough portion of the screw thread should be gripped firmly to secure the screw so that it does not rotate when exposed to torsion loads. The torque is applied by inserting the screw driver (bit) into the screw head. However, unlike solid core osteosynthesis screws, cannulated interference bioabsorbable screws have a cylindrical orifice along almost their entire length to the screw driver connection [95].

Torsion test results of PLDLA 70/30 screws during hydrolysis circumstance identify that the mechanical behavior of screws switched from ductile to fragile as a function of degradation time up to 240 days. The results demonstrated that the maximum torque varied from 1168 N.mm to 349 N.mm after 240 days, whereas the maximum torque angle varied from 85.42 to 8.28 degrees. Moreover, the torsional stiffness of screws decreased from 70 Nmm/deg to 54 Nmm/deg [94].

A novel hydroxyapatite ACL screw with a novel geometry presented by Schumacher et al. showed that the application of multiple threads with a large thread pitch to screw design facilitated the insertion of the screws into the bone without the application of screw driver or an external torque. Besides, the *ex vivo* studies of screws with rigid polyurethane (PU) foam and sheep ankle showed the pull-out forces of 486 ± 60 N and 387 ± 160 N, respectively, and these values are comparable to commercially BioComposite interference screws (Arthrex Inc., Germany) tested in PU foam, i.e., 435 ± 120 N [96].

Another research group performed a comparison between bioabsorbable screws (self-reinforced L-lactide/D-lactide, PLA 96/4, Bionx Implant Ltd., Tampere Finland) and titanium interference (Softsilk, Acufex Microsurgical Inc., Mansfield, Massachusetts) ones in ACL reconstruction using matched pairs of porcine knees. For this reason, two groups of screws were used in single and cyclic loading conditions [97]. The results showed that the mean ultimate failure loads for the single-cycle failure loading test were 837 ± 260 N and 863 ± 192 N for the bioabsorbable and titanium interference screws, respectively (no significant difference). Moreover, the yield loads were obtained as 605 ± 142 N and 585 ± 103 N for the bioabsorbable and titanium interference screws, respectively (no significant difference) [97].

For the sake of comparison, the characteristics of biomechanical properties for the ACL screws studied in the current review paper and other commercial screws are summarized in Table 2.

8. CONCLUSION

There are two different categories of ACL screws, namely metallic and bioabsorbable. The mechanical, physical, chemical composition, insertion technique, and various manufacturers as well as *in vivo* behaviors of different biodegradable commercial ACL screws were investigated in this research. The findings illustrated that the bioabsorbable screws showed similar behaviors to the metallic ones in several cases. However, the bioabsorbable screws suffer from some drawbacks, especially in bone ingrowth that prevents them from leaving a void after disappearing. Generally, the commercial bioabsorbable ACL screws are currently composed of polymers such as PLA and the enantiomers, PGA, PCL, and in some cases, composites of these polymers with inorganic filler phases such as Ca-P based products. Incorporation of bone mineral phases into ACLR screws may enhance the absorption rates of bioabsorbable screws, lessen the chances of osteogenesis, help neutralize the environs of bone site, and improve the mechanical properties.

The potential new generation of these screws may be magnesium screws and they have not reached their commercial production objective.

Given the literature reviews, the authors hold the belief that the biocomposite ACL screws rather than polymeric and metallic ones possess interesting features in terms of biological, physical, and mechanical properties. However, there are some challenges such as the optimum contents of bioceramics on osteogenesis and mechanical properties.

TABLE 2. Comparison of mechanical properties of commercial ACLR screws

Screws Compositions	Manufacturer	Screws Dimensions	Ultimate Failure Load	Yield Point Load	Ref.
			(N)	(N)	
30% β -TCP/70% PLLGA	DePuy	10 \times 35 mm	1113 \pm 362.2	845.1 \pm 243.7	[95]
30% BCP/70% PDLA	Arthrex	10 \times 35 mm	1051 \pm 244.5	792.2 \pm 157.5	[95]
70% PLGA/30% β -TCP	Milagro(DePuy)	10 mm	877 \pm 8	728	[98]
25% HA/75% PLLA	Smith & Nephew	10 \times 35 mm	920.3 \pm 283.5	684.1 \pm 163.9	[95]
70% PLDLA/30% BCP	BioComposite (Arthrex)	10 mm	1206 \pm 248	1053 \pm 378	[98]
Self-Reinforced L-lactide/D-lactide (PLA 96/4)	Bionx Implant Ltd., Tampere, Finland	7 \times 25 mm	837 \pm 260	621 \pm 139	[99]
25% HA/75% PLLA	Srtyker	10 \times 35 mm	1073.8 \pm 378.7	797.6 \pm 293.3	[95]
PLLA/TCP	Suspension screw (Bilok ST screw, Biocomposites Ltd, Etruria, UK)	9 \times 35 mm	1475	998.5	[49]
PLLA/TCP	Interference Screw (Bilok TS; Biocomposites Ltd)	9 \times 30 mm	652	538	[49]
PLLA	Arthrex, Naples, FL	7 \times 23 mm	995	689	[43]
PLLA 70/30	Linvatec, Largo, Florida- USA	9 \times 20 mm	607.11 \pm 97.49	509.98 \pm 94.03	[100]

REFERENCES

1. Fineberg, M. S., Zarins, B., Sherman, O. H., "Practical considerations in anterior cruciate ligament replacement surgery", *Arthroscopy: The Journal of Arthroscopic & Related Surgery*, Vol. 16, No. 7, (2000), 715-724. <https://doi.org/10.1053/jars.2000.8951>
2. Lee, J. W., Han, H. S., Han, K. J., Park, J., Jeon, H., Ok, M. R., Seok, H. K., Ahn, J. P., Lee, K. E., Lee, D. H., Yang, S. J., "Long-term clinical study and multiscale analysis of in vivo biodegradation mechanism of Mg alloy", *Proceedings of the National Academy of Sciences*, Vol. 113, No. 3, (2016), 716-721. <https://doi.org/10.1073/pnas.1518238113>
3. Zhao, D., Huang, S., Lu, F., Wang, B., Yang, L., Qin, L., Yang, K., Li, Y., Li, W., Wang, W., Tian, S., "Vascularized bone grafting fixed by biodegradable magnesium screw for treating osteonecrosis of the femoral head", *Biomaterials*, Vol. 81, (2016), 84-92. <https://doi.org/10.1016/j.biomaterials.2015.11.038>
4. Staiger, M. P., Pietak, A. M., Huadmai, J., Dias, G., "Magnesium and its alloys as orthopedic biomaterials: a review", *Biomaterials*, Vol. 27, No. 9, (2006), 1728-1734. <https://doi.org/10.1016/j.biomaterials.2005.10.003>
5. Sumner, D. R., Galante, J. O., "Determinants of stress shielding: design versus materials versus interface", *Clinical Orthopaedics and Related Research*, Vol. 274, (1992), 202-212. <https://doi.org/10.1097/00003086-199201000-00020>
6. Cutright, D. E., Hunsuck, E. E., "Tissue reaction to the biodegradable polylactic acid suture", *Oral Surgery, Oral Medicine, Oral Pathology*, Vol. 31, No. 1, (1971), 134-139. [https://doi.org/10.1016/0030-4220\(71\)90044-2](https://doi.org/10.1016/0030-4220(71)90044-2)
7. Konan, S., Haddad, F. S., "A clinical review of bioabsorbable interference screws and their adverse effects in anterior cruciate ligament reconstruction surgery", *The Knee*, Vol. 16, No. 1, (2009), 6-13. <https://doi.org/10.1016/j.knee.2008.06.001>
8. Lambert, K. L., "Vascularized patellar tendon graft with rigid internal fixation for anterior cruciate ligament insufficiency", *Clinical Orthopaedics and Related Research (1976-2007)*, Vol. 172, (1983), 85-89. <https://doi.org/10.1097/00003086-198301000-00016>
9. Kurosaka, M., Yoshiya, S., Andrich, J. T., "A biomechanical comparison of different surgical techniques of graft fixation in anterior cruciate ligament reconstruction", *The American Journal of Sports Medicine*, Vol. 15, No. 3, (1987), 225-229. <https://doi.org/10.1177/036354658701500306>
10. Almazán, A., Miguel, A., Odor, A., Ibarra, J. C., "Intraoperative incidents and complications in primary arthroscopic anterior cruciate ligament reconstruction", *Arthroscopy: The Journal of Arthroscopic & Related Surgery*, Vol. 22, No. 11, (2006), 1211-1217. <https://doi.org/10.1016/j.arthro.2006.06.019>
11. Matthews, L. S., Soffer, S. R., "Pitfalls in the use of interference screws for anterior cruciate ligament reconstruction: brief report", *Arthroscopy: The Journal of Arthroscopic & Related Surgery*, Vol. 5, No. 3, (1989), 225-226. [https://doi.org/10.1016/0749-8063\(89\)90177-1](https://doi.org/10.1016/0749-8063(89)90177-1)
12. Böstman, O. M., Pihlajamäki, H. K., "Adverse tissue reactions to bioabsorbable fixation devices", *Clinical Orthopaedics and Related Research (1976-2007)*, Vol. 371, (2000), 216-227. <https://doi.org/10.1097/00003086-200002000-00026>
13. Bottoni, C. R., DeBerardino, T. M., Fester, E. W., Mitchell, D., Penrod, B. J., "An intra-articular bioabsorbable interference screw mimicking an acute meniscal tear 8 months after an anterior cruciate ligament reconstruction", *Arthroscopy: The Journal of Arthroscopic & Related Surgery*, Vol. 16, No. 4, (2000), 395-398. [https://doi.org/10.1016/S0749-8063\(00\)90085-9](https://doi.org/10.1016/S0749-8063(00)90085-9)
14. Barber, F. A., Boothby, M. H., "Bilok interference screws for anterior cruciate ligament reconstruction: clinical and radiographic outcomes", *Arthroscopy: The Journal of Arthroscopic & Related Surgery*, Vol. 23, No. 5, (2007), 476-481. <https://doi.org/10.1016/j.arthro.2006.12.026>

15. Davis, K., Huser, A., Kreofsky, C., Nadler, D., Poblacki, J., "Bioactive Interference Screw for ACL Reconstruction", *Biomedical Engineering Design* 400, University of Wisconsin-Madison. December 7, (2005). <http://130.203.136.95/viewdoc/download?doi=10.1.1.456.6058&rep=rep1&type=pdf>
16. Watson, J. N., McQueen, P., Kim, W., Hutchinson, M. R., "Bioabsorbable interference screw failure in anterior cruciate ligament reconstruction: a case series and review of the literature", *The Knee*, Vol. 22, No. 3, (2015), 256-261. <https://doi.org/10.1016/j.knee.2015.02.015>
17. Moisala, A. S., Järvelä, T., Paakkala, A., Paakkala, T., Kannus, P., Järvinen, M., "Comparison of the bioabsorbable and metal screw fixation after ACL reconstruction with a hamstring autograft in MRI and clinical outcome: a prospective randomized study", *Knee Surgery, Sports Traumatology, Arthroscopy*, Vol. 16, No. 12, (2008), 1080-1086. <https://doi.org/10.1007/s00167-008-0593-z>
18. Mayr, H. O., Hube, R., Bernstein, A., Seibt, A. B., Hein, W., von Eisenhart-Rothe, R., "Beta-tricalcium phosphate plugs for press-fit fixation in ACL reconstruction—a mechanical analysis in bovine bone", *The Knee*, Vol. 14, No. 3, (2007), 239-244. <https://doi.org/10.1016/j.knee.2007.01.006>
19. Arama, Y., Salmon, L. J., Sri-Ram, K., Linklater, J., Roe, J. P., Pinczewski, L. A., "Bioabsorbable versus titanium screws in anterior cruciate ligament reconstruction using hamstring autograft: a prospective, blinded, randomized controlled trial with 5-year follow-up", *The American Journal of Sports Medicine*, Vol. 43, No. 8, (2015), 1893-1901. <https://doi.org/10.1177/0363546515588926>
20. Gulick, D. T., Yoder, H. N., "Anterior cruciate ligament reconstruction: clinical outcomes of patella tendon and hamstring tendon grafts", *Journal of Sports Science & Medicine*, Vol. 1, No. 3, (2002), 63-71.
21. Laxdal, G., Kartus, J., Eriksson, B. I., Faxen, E., Sernert, N., Karlsson, J., "Biodegradable and metallic interference screws in anterior cruciate ligament reconstruction surgery using hamstring tendon grafts: prospective randomized study of radiographic results and clinical outcome", *The American Journal of Sports Medicine*, Vol. 34, No. 10, (2006), 1574-1580. <https://doi.org/10.1177/0363546506288014>
22. Shen, C., Jiang, S. D., Jiang, L. S., Dai, L. Y., "Bioabsorbable versus metallic interference screw fixation in anterior cruciate ligament reconstruction: a meta-analysis of randomized controlled trials", *Arthroscopy: The Journal of Arthroscopic & Related Surgery*, Vol. 26, No. 5, (2010), 705-713. <https://doi.org/10.1016/j.arthro.2009.12.011>
23. Cheng, P., Han, P., Zhao, C., Zhang, S., Wu, H., Ni, J., Hou, P., Zhang, Y., Liu, J., Xu, H., Liu, S., "High-purity magnesium interference screws promote fibrocartilaginous entheses regeneration in the anterior cruciate ligament reconstruction rabbit model via accumulation of BMP-2 and VEGF", *Biomaterials*, Vol. 81, (2016), 14-26. <https://doi.org/10.1016/j.biomaterials.2015.12.005>
24. Bach, F. D., Carlier, R. Y., Elis, J. B., Mompont, D. M., Feydy, A., Judet, O., Beaufils, P., Vallée, C., "Anterior cruciate ligament reconstruction with bioabsorbable polyglycolic acid interference screws: MR imaging follow-up", *Radiology*, Vol. 225, No. 2, (2002), 541-550. <https://doi.org/10.1148/radiol.2252010357>
25. Bedi, A., Kawamura, S., Ying, L., Rodeo, S. A., "Differences in tendon graft healing between the intra-articular and extra-articular ends of a bone tunnel", *HSS Journal*, Vol. 5, No. 1, (2009), 51-57. <https://doi.org/10.1007/s11420-008-9096-1>
26. Morgan, C. D., Gehrman, R. M., Jayo, M. J., Johnson, C. S., "Histologic findings with a bioabsorbable anterior cruciate ligament interference screw explant after 2.5 years in vivo", *Arthroscopy: The Journal of Arthroscopic & Related Surgery*, Vol. 18, No. 9, (2002), 1-6. <https://doi.org/10.1053/jars.2002.36466>
27. Park, M. C., Tibone, J. E., "False magnetic resonance imaging persistence of a biodegradable anterior cruciate ligament interference screw with chronic inflammation after 4 years in vivo", *Arthroscopy: The Journal of Arthroscopic & Related Surgery*, Vol. 22, No. 8, (2006), 911-e1. <https://doi.org/10.1016/j.arthro.2005.06.030>
28. Warden, W. H., Chooljian, D., Jackson, D. W., "Ten-year magnetic resonance imaging follow-up of bioabsorbable poly-L-lactic acid interference screws after anterior cruciate ligament reconstruction", *Arthroscopy: The Journal of Arthroscopic & Related Surgery*, Vol. 24, No. 3, (2008), 370-e1. <https://doi.org/10.1016/j.arthro.2006.12.032>
29. Barber, F. A., Elrod, B. F., McGuire, D. A., Paulos, L. E., "Bioscrew fixation of patellar tendon autografts", *Biomaterials*, Vol. 21, No. 24, (2000), 2623-2629. [https://doi.org/10.1016/s0142-9612\(00\)00130-7](https://doi.org/10.1016/s0142-9612(00)00130-7)
30. Fink, C., Benedetto, K. P., Hackl, W., Hoser, C., Freund, M. C., Rieger, M., "Bioabsorbable polyglyconate interference screw fixation in anterior cruciate ligament reconstruction: a prospective computed tomography-controlled study", *Arthroscopy: The Journal of Arthroscopic & Related Surgery*, Vol. 16, No. 5, (2000), 491-498. <https://doi.org/10.1053/jars.2000.4633>
31. Hackl, W., Fink, C., Benedetto, K. P., Hoser, C., "Transplant fixation by anterior cruciate ligament reconstruction. Metal vs. bioabsorbable polyglyconate interference screw. A prospective randomized study of 40 patients", *Der Unfallchirurg*, Vol. 103, No. 6, (2000), 468-474. <https://doi.org/10.1007/s001130050567>
32. Kaeding, C., Farr, J., Kavanaugh, T., Pedroza, A., "A prospective randomized comparison of bioabsorbable and titanium anterior cruciate ligament interference screws", *Arthroscopy: The Journal of Arthroscopic & Related Surgery*, Vol. 21, No. 2, (2005), 147-151. <https://doi.org/10.1016/j.arthro.2004.09.012>
33. Marti, C., Imhoff, A. B., Bahrs, C., Romero, J., "Metallic versus bioabsorbable interference screw for fixation of bone-patellar tendon-bone autograft in arthroscopic anterior cruciate ligament reconstruction A preliminary report", *Knee Surgery, Sports Traumatology, Arthroscopy*, Vol. 5, No. 4, (1997), 217-221. <https://doi.org/10.1007/s001670050053>
34. Myers, P., Logan, M., Stokes, A., Boyd, K., Watts, M., "Bioabsorbable versus titanium interference screws with hamstring autograft in anterior cruciate ligament reconstruction: a prospective randomized trial with 2-year follow-up", *Arthroscopy: The Journal of Arthroscopic & Related Surgery*, Vol. 24, No. 7, (2008), 817-823. <https://doi.org/10.1016/j.arthro.2008.02.011>
35. Shen, P. H., Lien, S. B., Shen, H. C., Wang, C. C., Huang, G. S., Chao, K. H., Lee, C. H., Lin, L. C., "Comparison of different sizes of bioabsorbable interference screws for anterior cruciate ligament reconstruction using bioabsorbable bead augmentation in a porcine model", *Arthroscopy: The Journal of Arthroscopic & Related Surgery*, Vol. 25, No. 10, (2009), 1101-1107. <https://doi.org/10.1016/j.arthro.2009.05.011>
36. Drogset, J. O., Grøntvedt, T., Tegnander, A., "Endoscopic reconstruction of the anterior cruciate ligament using bone-patellar tendon-bone grafts fixed with bioabsorbable or metal interference screws: a prospective randomized study of the clinical outcome", *The American Journal of Sports Medicine*, Vol. 33, No. 8, (2005), 1160-1165. <https://doi.org/10.1177/0363546504272264>
37. Papalia, R., Vasta, S., D'Adamio, S., Giacalone, A., Maffulli, N., Denaro, V., "Metallic or bioabsorbable interference screw for graft fixation in anterior cruciate ligament (ACL) reconstruction?", *British Medical Bulletin*, Vol. 109, No. 1, (2014), 19-29. <http://doi.org/10.1093/bmb/ldt038>

38. Wang, J., Xu, J., Song, B., Chow, D. H., Yung, P. S. H., Qin, L., "Magnesium (Mg) based interference screws developed for promoting tendon graft incorporation in bone tunnel in rabbits", *Acta Biomaterialia* Vol. 63, (2017), 393–410. <http://doi.org/10.1016/j.actbio.2017.09.018>
39. Chen, C. H., Lee, C. H., "Biological fixation in anterior cruciate ligament surgery", *Asia-Pacific Journal of Sports Medicine, Arthroscopy, Rehabilitation and Technology*, Vol. 1, No. 2, (2014), 48–53. <http://doi.org/10.1016/j.asmart.2014.02.004>
40. Kohn, J., Abramson, S., Langer, R., "Bioresorbable and bioerodible materials", In Ratner, B. D., Hoffman, A. S., Schoen, F. J., Lemons, J. E. (eds), *Biomaterials Science: An Introduction to Materials in Medicine*, Elsevier Academic Press, San Diego, (2004), 115–127.
41. Urayama, H., Kanamori, T., Kimura, Y., "Microstructure and thermomechanical properties of glassy polylactides with different optical purity of the lactate units", *Macromolecular Materials and Engineering*, Vol. 286, No. 11, (2001), 705-713. [https://doi.org/10.1002/1439-2054\(20011101\)286:11<705::AID-MAME705>3.0.CO;2-Q](https://doi.org/10.1002/1439-2054(20011101)286:11<705::AID-MAME705>3.0.CO;2-Q)
42. Törmälä, P., "Biodegradable self-reinforced composite materials; manufacturing structure and mechanical properties", *Clinical Materials*, Vol. 10, No. 1-2, (1992), 29-34. [https://doi.org/10.1016/0267-6605\(92\)90081-4](https://doi.org/10.1016/0267-6605(92)90081-4)
43. Rupp, S., Krauss, P. W., Fritsch, E. W., "Fixation strength of a biodegradable interference screw and a press-fit technique in anterior cruciate ligament reconstruction with a BPTB graft", *Arthroscopy: The Journal of Arthroscopic & Related Surgery*, Vol. 13, No. 1, (1997), 61-65. [https://doi.org/10.1016/s0749-8063\(97\)90210-3](https://doi.org/10.1016/s0749-8063(97)90210-3)
44. Caborn, D. N., Brand Jr, J. C., Nyland, J., Kocabey, Y., "A biomechanical comparison of initial soft tissue tibial fixation devices: the Intrafix versus a tapered 35-mm bioabsorbable interference screw", *The American Journal of Sports Medicine*, Vol. 32, No. 4, (2004), 956-961. <https://doi.org/10.1177/0363546503261696>
45. Chang, H. C., Nyland, J., Nawab, A., Burden, R., Caborn, D. N., "Biomechanical comparison of the bioabsorbable RetroScrew system, BioScrew XtraLok with stress equalization tensioner, and 35-mm Delta Screws for tibialis anterior graft-tibial tunnel fixation in porcine tibiae", *The American Journal of Sports Medicine*, Vol. 33, No. 7, (2005), 1057-1064. <https://doi.org/10.1177/0363546504272265>
46. Pena, F., Grøntvedt, T., Brown, G. A., Aune, A. K., Engebretsen, L., "Comparison of failure strength between metallic and absorbable interference screws: influence of insertion torque, tunnel-bone block gap, bone mineral density, and interference", *The American Journal of Sports Medicine*, Vol. 24, No. 3, (1996), 329-334. <https://doi.org/10.1177/036354659602400314>
47. Kousa, P., Jarvinen, T. L., Pohjonen, T., Kannus, P., Kotikoski, M., Jarvinen, M., "Fixation strength of a biodegradable screw in anterior cruciate ligament reconstruction", *The Journal of Bone and Joint Surgery. British Volume*, Vol. 77, No. 6, (1995), 901-905. <https://doi.org/10.1302/0301-620x.77b6.7593103>
48. Oh, Y. H., Namkoong, S., Strauss, E. J., Ishak, C., Jazrawi, L. M., Rosen, J., "Hybrid femoral fixation of soft-tissue grafts in anterior cruciate ligament reconstruction using the EndoButton CL and bioabsorbable interference screws: a biomechanical study", *Arthroscopy: The Journal of Arthroscopic & Related Surgery*, Vol. 22, No. 11, (2006), 1218-1224. <https://doi.org/10.1016/j.arthro.2006.07.022>
49. Weimann, A., Rodieck, M., Zantop, T., Hassenpflug, J., Petersen, W., "Primary stability of hamstring graft fixation with biodegradable suspension versus interference screws", *Arthroscopy: The Journal of Arthroscopic & Related Surgery*, Vol. 21, No. 3, (2005), 266-274. <https://doi.org/10.1016/j.arthro.2004.10.011>
50. Lenza, R. F. S., Jones, J. R., Vasconcelos, W. L., Hench, L. L., "In vitro release kinetics of proteins from bioactive foams", *Journal of Biomedical Materials Research Part A: An Official Journal of The Society for Biomaterials, The Japanese Society for Biomaterials, and The Australian Society for Biomaterials and the Korean Society for Biomaterials*, Vol. 67, No. 1, (2003), 121-129. <https://doi.org/10.1002/jbm.a.10042>
51. Nakafuku, C., Takehisa, S. Y., "Glass transition and mechanical properties of PLLA and PDLLA- PGA copolymer blends", *Journal of Applied Polymer Science*, Vol. 93, No. 5, (2004), 2164-2173. <https://doi.org/10.1002/app.20687>
52. Barber, F. A., "Poly-D, L-lactide interference screws for anterior cruciate ligament reconstruction", *Arthroscopy: The Journal of Arthroscopic & Related Surgery*, Vol. 21, No. 7, (2005), 804-808. <https://doi.org/10.1016/j.arthro.2005.04.104>
53. Esmaeilzadeh, J., Hesaraki, S., Hadavi, S. M. M., Esfandeh, M., Ebrahimzadeh, M. H., "Microstructure and mechanical properties of biodegradable poly (D/L) lactic acid/polycaprolactone blends processed from the solvent-evaporation technique", *Materials Science and Engineering: C*, Vol. 71, (2017), 807-819. <https://doi.org/10.1016/j.msec.2016.10.070>
54. Esmaeilzadeh, J., Hesaraki, S., Hadavi, S. M. M., Ebrahimzadeh, M. H., Esfandeh, M., "Poly (D/L) lactide/polycaprolactone/bioactive glass nanocomposites materials for anterior cruciate ligament reconstruction screws: The effect of glass surface functionalization on mechanical properties and cell behaviors", *Materials Science and Engineering: C*, Vol. 77, (2017), 978-989. <https://doi.org/10.1016/j.msec.2017.03.134>
55. Martinek, V., Friederich, N. F., "Tibial and pretibial cyst formation after anterior cruciate ligament reconstruction with bioabsorbable interference screw fixation", *Arthroscopy: The Journal of Arthroscopic & Related Surgery*, Vol. 15, No. 3, (1999), 317-320. [https://doi.org/10.1016/s0749-8063\(99\)70042-3](https://doi.org/10.1016/s0749-8063(99)70042-3)
56. Jagodzinski, M., Scheunemann, K., Knobloch, K., Albrecht, K., Krettek, C., Hurschler, C., Zeichen, J., "Tibial press-fit fixation of the hamstring tendons for ACL-reconstruction", *Knee Surgery, Sports Traumatology, Arthroscopy*, Vol. 14, No. 12, (2006), 1281-1287. <https://doi.org/10.1007/s00167-006-0105-y>
57. Lajtai, G., Schmiedhuber, G., Unger, F., Aitzetmüller, G., Klein, M., Noszian, I., Orthner, E., "Bone tunnel remodeling at the site of biodegradable interference screws used for anterior cruciate ligament reconstruction: 5-year follow-up", *Arthroscopy: The Journal of Arthroscopic & Related Surgery*, Vol. 17, No. 6, (2001), 597-602. <https://doi.org/10.1053/jars.2001.21535>
58. Weimann, A., Zantop, T., Herbolt, M., Strobel, M., Petersen, W., "Initial fixation strength of a hybrid technique for femoral ACL graft fixation", *Knee Surgery, Sports Traumatology, Arthroscopy*, Vol. 14, No. 11, (2006), 1122-1129. <https://doi.org/10.1007/s00167-006-0159-x>
59. Pêgo, A. P., Grijpma, D. W., Feijen, J., "Enhanced mechanical properties of 1, 3-trimethylene carbonate polymers and networks", *Polymer*, Vol. 44, No. 21, (2003), 6495-6504. [https://doi.org/10.1016/s0032-3861\(03\)00668-2](https://doi.org/10.1016/s0032-3861(03)00668-2)
60. Farrar, D. F., Gillson, R. K., "Hydrolytic degradation of polyglyconate B: the relationship between degradation time, strength and molecular weight", *Biomaterials*, Vol. 23, No. 18, (2002), 3905-3912. [https://doi.org/10.1016/s0142-9612\(02\)00140-0](https://doi.org/10.1016/s0142-9612(02)00140-0)
61. Demirhan, M., Kilicoglu, O., Akpinar, S., Akman, S., Atalar, A. C., Göksan, M. A., "Time-dependent reduction in load to failure of wedge-type polyglyconate suture anchors", *Arthroscopy: The Journal of Arthroscopic & Related Surgery*, Vol. 16, No. 4, (2000), 383-390. [https://doi.org/10.1016/s0749-8063\(00\)90083-5](https://doi.org/10.1016/s0749-8063(00)90083-5)

62. Nieminen, T., Rantala, I., Hiidenheimo, I., "Biodegradable plates and screws composed of L-lactide, D-lactide and trimethylenecarbonate: Properties during a 3-year follow-up", In *European Conference on Biomaterials*, Nantes, France, (2006).
63. Järvelä, T., Nurmi, J. T., Paakkala, A., Moissala, A. S., Kaikkonen, A., Järvinen, M., "Chapter 52 - Improving Biodegradable Interference Screw Properties by Combining Polymers", In *The Anterior Cruciate Ligament: Reconstruction and Basic Science*, Elsevier BV, (2008), 386–391. <http://doi.org/10.1016/b978-1-4160-3834-4.10052-6>
64. Barth, J., Akritopoulos, P., Gravelleau, N., Barthelemy, R., Toanen, C., Saffarini, M., "Efficacy of osteoconductive ceramics in bioresorbable screws for anterior cruciate ligament reconstruction: a prospective intrapatient comparative study", *Orthopaedic Journal of Sports Medicine*, Vol. 4, No. 5, (2016), 2325967116647724. <https://doi.org/10.1177/2325967116647724>
65. Lee, D. W., Lee, J. W., Kim, S. B., Park, J. H., Chung, K. S., Ha, J. K., Kim, J. G., Kim, W. J., "Comparison of poly-L-lactic acid and poly-L-lactic acid/hydroxyapatite bioabsorbable screws for tibial fixation in ACL reconstruction: clinical and magnetic resonance imaging results", *Clinics in Orthopedic Surgery*, Vol. 9, No. 3, (2017), 270-279. <https://doi.org/10.4055/cios.2017.9.3.270>
66. Hunt, J. A., Callaghan, J. T., "Polymer-hydroxyapatite composite versus polymer interference screws in anterior cruciate ligament reconstruction in a large animal model", *Knee Surgery, Sports Traumatology, Arthroscopy*, Vol. 16, No. 7, (2008), 655-660. <https://doi.org/10.1007/s00167-008-0528-8>
67. Barber, F. A., Dockery, W. D., "Long-term absorption of poly-L-lactic acid interference screws", *Arthroscopy: The Journal of Arthroscopic & Related Surgery*, Vol. 22, No. 8, (2006), 820-826. <https://doi.org/10.1016/j.arthro.2006.04.096>
68. Barber, F. A., Dockery, W. D., "Long-Term Degradation of Self-Reinforced Poly-Levo (96%)/Dextro (4%)–Lactide/ β -Tricalcium Phosphate Biocomposite Interference Screws", *Arthroscopy: The Journal of Arthroscopic & Related Surgery*, Vol. 32, No. 4, (2016), 608-614. <https://doi.org/10.1016/j.arthro.2015.08.037>
69. Ntgiopoulos, P. G., Demey, G., Tavernier, T., Dejour, D., "Comparison of resorption and remodeling of bioabsorbable interference screws in anterior cruciate ligament reconstruction", *International Orthopaedics*, Vol. 39, No. 4, (2015), 697-706. <https://doi.org/10.1007/s00264-014-2530-8>
70. Barber, F. A., Dockery, W. D., "Biocomposite Interference Screws in Anterior Cruciate Ligament Reconstruction: Osteoconductivity and Degradation", *Arthroscopy, Sports Medicine, and Rehabilitation*, Vol. 2, No. 2, (2020), e53–e58. <http://doi.org/10.1016/j.asmr.2019.10.001>
71. Walsh, W. R., Cotton, N. J., Stephens, P., Brunelle, J. E., Langdown, A., Auld, J., Vizesi, F., Bruce, W., "Comparison of poly-L-lactide and polylactide carbonate interference screws in an ovine anterior cruciate ligament reconstruction model", *Arthroscopy: The Journal of Arthroscopic & Related Surgery*, Vol. 23, No. 7, (2007), 757-765. <https://doi.org/10.1016/j.arthro.2007.01.030>
72. Agrawal, C. M., Athanasiou, K. A., "Technique to control pH in vicinity of biodegrading PLA- PGA implants", *Journal of biomedical materials research*, Vol. 38, No. 2, (1997), 105-114. [https://doi.org/10.1002/\(sici\)1097-4636\(199722\)38:2%3C105::aid-jbm4%3E3.0.co;2-u](https://doi.org/10.1002/(sici)1097-4636(199722)38:2%3C105::aid-jbm4%3E3.0.co;2-u)
73. Cooper, J. J., Mackie, A. T., "In vitro evaluation of a range of bioabsorbable composite interference screws designed for anterior cruciate ligament reconstruction", In *54th Annual Meeting of the Orthopaedic Research Society, San Francisco, CA*, February 2008, (2008). <https://www.ors.org/Transactions/54/1278.pdf>
74. Aunoble, S., Clément, D., Frayssinet, P., Harmand, M. F., Le Huec, J. C., "Biological performance of a new β -TCP/PLLA composite material for applications in spine surgery: In vitro and in vivo studies", *Journal of Biomedical Materials Research Part A: An Official Journal of The Society for Biomaterials, The Japanese Society for Biomaterials, and The Australian Society for Biomaterials and the Korean Society for Biomaterials*, Vol. 78, No. 2, (2006), 416-422. <https://doi.org/10.1002/jbm.a.30749>
75. Purcell, D. B., Rudzki, J. R., Wright, R. W., "Bioabsorbable interference screws in ACL reconstruction", *Operative Techniques in Sports Medicine*, Vol. 12, No. 3, (2004), 180-187. <https://doi.org/10.1053/j.otsm.2004.07.014>
76. Pigni, M., Leardi, G., Battistella, F., Bernasconi, S., "Hamstring anterior cruciate ligament reconstruction in skiers: tibial fixation with bioabsorbable or not bioabsorbable system", In *International Congress*, (2006).
77. Poandl, T., Trenka-Benthin, S., Azri-Meehan, S., Contiliano, J., Li, Y., Yuan, J., TenHuisen, K., Dooley, J., Zimmerman, M., "A new faster-absorbing biocomposite material: Long-term in-vivo tissue reaction and absorption", E-poster presented at: *Spring Arthroscopy Association of North America (AANA) Meeting, Vancouver, Canada*, May 2005, (2005), E-09. <http://prod.mitek.depuj.edgesuite.net/PDFsforWebsite/900858.pdf>
78. Siebold, R., "Observations on Bone Tunnel Enlargement After Double-Bundle Anterior Cruciate Ligament Reconstruction", *Arthroscopy: The Journal of Arthroscopic & Related Surgery*, Vol. 23, No. 3, (2007), 291–298. <http://doi.org/10.1016/j.arthro.2007.01.006>
79. LeGeros, R. Z., LeGeros, J. P., "Dense hydroxyapatite", In *An Introduction to Bioceramics*, (1993), 139-180. https://doi.org/10.1142/9789814317351_0009
80. Bailey, C. A., Kuiper, J. H., Kelly, C. P., "Biomechanical evaluation of a new composite bioresorbable screw", *Journal of Hand Surgery*, Vol. 31, No. 2, (2006), 208-212. <https://doi.org/10.1016/j.jhsb.2005.10.015>
81. Tecklenburg, K., Burkart, P., Hoser, C., Rieger, M., Fink, C., "Prospective evaluation of patellar tendon graft fixation in anterior cruciate ligament reconstruction comparing composite bioabsorbable and allograft interference screws", *Arthroscopy: The Journal of Arthroscopic & Related Surgery*, Vol. 22, No. 9, (2006), 993-999. <https://doi.org/10.1016/j.arthro.2006.05.010>
82. Baums, M. H., Zelle, B. A., Schultz, W., Ernstberger, T., Klinger, H. M., "Intraarticular migration of a broken biodegradable interference screw after anterior cruciate ligament reconstruction", *Knee Surgery, Sports Traumatology, Arthroscopy*, Vol. 14, No. 9, (2006), 865-868. <https://doi.org/10.1007/s00167-006-0049-2>
83. Krappel, F. A., Bauer, E., Harland, U., "The migration of a BioScrew® as a differential diagnosis of knee pain, locking after ACL reconstruction: a report of two cases", *Archives of Orthopaedic and Trauma Surgery*, Vol. 126, No. 9, (2006), 615-620. <https://doi.org/10.1007/s00402-006-0101-1>
84. Wang, J., Wu, Y., Li, H., Liu, Y., Bai, X., Chau, W., Zheng, Y., Qin, L., "Magnesium alloy based interference screw developed for ACL reconstruction attenuates peri-tunnel bone loss in rabbits", *Biomaterials*, Vol. 157, (2018), 86-97. <https://doi.org/10.1016/j.biomaterials.2017.12.007>
85. Song, B., Li, W., Chen, Z., Fu, G., Li, C., Liu, W., Li, Y., Qin, L., Ding, Y., "Biomechanical comparison of pure magnesium interference screw and polylactic acid polymer interference screw in anterior cruciate ligament reconstruction—A cadaveric experimental study", *Journal of Orthopaedic Translation*, Vol. 8, (2017), 32-39. <https://doi.org/10.1016/j.jot.2016.09.001>
86. Agarwal, S., Curtin, J., Duffy, B., Jaiswal, S., "Biodegradable magnesium alloys for orthopaedic applications: A review on corrosion, biocompatibility and surface modifications", *Materials Science and Engineering: C*, Vol. 68, (2016), 948-963. <https://doi.org/10.1016/j.msec.2016.06.020>

87. Zheng Y. F., Gu, X. N., Witte, F., "Biodegradable metals", *Materials Science and Engineering: R: Reports*, Vol. 77, (2014), 1–34. <http://doi.org/10.1016/j.msere.2014.01.001>
88. Li, N., Zheng, Y., "Novel magnesium alloys developed for biomedical application: a review", *Journal of Materials Science & Technology*, Vol. 29, No. 6, (2013), 489-502. <https://doi.org/10.1016/j.jmst.2013.02.005>
89. Cheng, P., Han, P., Zhao, C., Zhang, S., Zhang, X., Chai, Y., "Magnesium inference screw supports early graft incorporation with inhibition of graft degradation in anterior cruciate ligament reconstruction", *Scientific Reports*, Vol. 6, (2016), p.26434. <https://doi.org/10.1038/srep26434>
90. Yao, Y., Wang, L., Li, J., Tian, S., Zhang, M., Fan, Y., "A novel auxetic structure based bone screw design: Tensile mechanical characterization and pullout fixation strength evaluation", *Materials & Design*, Vol. 188, (2020), 108424. <https://doi.org/10.1016/j.matdes.2019.108424>
91. Butler, D. L., "Anterior cruciate ligament: Its normal response and replacement", *Journal of Orthopaedic Research*, Vol. 7, No. 6, (1989), 910-921. <https://doi.org/10.1002/jor.1100070618>
92. Rodeo, S. A., Arnoczky, S. P., Torzilli, P. A., Hidaka, C., Warren, R. F., "Tendon-healing in a bone tunnel. A biomechanical and histological study in the dog", *The Journal of bone and joint surgery. American volume*, Vol. 75, No. 12, (1993), 1795-1803. <https://doi.org/10.2106/00004623-199312000-00009>
93. Beevers, D. J., "Metal vs bioabsorbable interference screws: initial fixation", *Proceedings of the Institution of Mechanical Engineers, Part H: Journal of Engineering in Medicine*, Vol. 217 No. 1, (2003), 59-75. <https://doi.org/10.1243/095441103762597746>
94. Roesler, C. R. M., Salmoria, G. V., Moré, A. D. O., Vassoler, J. M., Fancello, E. A., "Torsion test method for mechanical characterization of PLDLA 70/30 ACL interference screws", *Polymer Testing*, Vol. 34, (2014), 34-41. <https://doi.org/10.1016/j.polymertesting.2013.12.005>
95. Nyland, J., Krupp, R., Greene, J., Bowles, R., Burden, R., Caborn, D. N., "In situ comparison of varying composite tibial tunnel interference screws used for ACL soft tissue graft fixation", *The Knee*, Vol. 22, No. 6, (2015), 554-558. <https://doi.org/10.1016/j.knee.2015.03.009>
96. Schumacher, T. C., Tushtev, K., Wagner, U., Becker, C., große Holthaus, M., Hein, S. B., Haack, J., Heiss, C., Engelhardt, M., El Khassawna, T., Rezwan, K., "A novel, hydroxyapatite-based screw-like device for anterior cruciate ligament (ACL) reconstructions", *The Knee*, Vol. 24, No. 5, (2017), 933-939. <https://doi.org/10.1016/j.knee.2017.07.005>
97. Resende, J. L., Faria, M. T. C., Las Casas, E. B., Oliveira, E. A., Gomes, P. D. T. V., "Mechanical properties characterization of knee cruciate ligaments through tensile tests", In *Proceedings of the 18th International Congress of Mechanical Engineering (COBEM 2005), Ouro Preto-MG, Brazil*, 6-11 November 2005, (2005), 1-7.
98. "Arthrex BioComposite interference screws for ACL and PCL reconstruction", LA1-0150-EN_E, Naples, FL, (2018).
99. Kousa, P., Järvinen, T. L., Kannus, P., Järvinen, M., "Initial fixation strength of bioabsorbable and titanium interference screws in anterior cruciate ligament reconstruction: biomechanical evaluation by single cycle and cyclic loading", *The American Journal of Sports Medicine*, Vol. 29, No. 4, (2001), 420-425. <https://doi.org/10.1177/03635465010290040601>
100. Moré, A. D. O., Pizzolatti, A. L. A., Fancello, E. A., Salmoria, G.V., Roesler, C. R. D. M., "Graft tendon slippage with metallic and bioabsorbable interference screws under cyclic load: a biomechanical study in a porcine model", *Research on Biomedical Engineering*, Vol. 31, No. 1, (2015), 56-61. <https://doi.org/10.1590/2446-4740.0652>



Synthesis of a Macroporous Glass-Ceramic Scaffold Containing Fluorapatite Crystalline Phase for Bone Substitutes

M. Rezvani ^{a*}, E. Alahgholizadeh ^a, L. Roshangar ^b

^a Department of Materials Engineering, Faculty of Mechanical Engineering, University of Tabriz, Tabriz, Iran

^b Histology and Embryology Stem Cell Research Center, Tabriz University of Medical Sciences, Tabriz, Iran

PAPER INFO

Paper History:

Received 02 June 2019
Received in revised form 16 July 2019
Accepted 16 August 2019

Keywords:

Glass-Ceramic
Fluorapatite
Macroporous
Porogen

ABSTRACT

Bioactive glass-ceramics play an important role in bone tissue regeneration. In the present research, the crystallization of glasses and scaffold fabrication were investigated. After choosing the appropriate composition in the $\text{SiO}_2\text{-CaO-Na}_2\text{O-P}_2\text{O}_5$ system, raw materials were melted at 1400°C and then, quenched in water. Subsequently, the crystallization of synthesized glass samples was studied. Fourier Transfer infrared (FT-IR) spectroscopy was carried out to study the structural changes of the samples. XRD patterns showed that fluorapatite $\text{Ca}_{10}(\text{PO}_4)_6(\text{O,F}_2)$ was the only precipitated crystalline phase. The template synthesis method was applied for the fabrication of the scaffold and starch as a porogen material. The optimized scaffold structure was chosen with the appropriate size of pores, interconnectivity, and strength behavior through investigating the porosity, SEM images, and mechanical properties. ICP, SEM, and EDX analyses were used to determine the in vitro bioactivity of the samples after immersion for 14 days in SBF.

1. INTRODUCTION

In recent decades, many types of research have been conducted on orthopedic surgery and bone tissue engineering. The scaffold is a key material in this application, which acts as a matrix for the growth of bone cells [1-7]. For being used as bone grafts, the ideal of scaffold for replacing part of the porous bone is as following:

- 1) Having 50-60% porosity with interconnected porosity and the average pore size higher than $100\mu\text{m}$, so that the cells can easily grow inside and carry the food to the bone.
- 2) Being made of biocompatible and bioactive materials.
- 3) Having a rough surface to make the soft tissue more adhesive.
- 4) Having a simple preparation method that can be prepared in different forms for various damaged areas of the body [1-7].

Therefore, the necessity of a bioactive material for cells growth with a porous structure is inevitable. Most of the bioactive materials used in bone tissue engineering applications are bio-ceramics, such as calcium phosphates, hydroxyapatite (HA), composite materials,

metals, glass, and glass-ceramics [8-10]. Bioactive materials can bond to bone tissue through forming a bone-like hydroxyapatite layer on their surface in physiological body fluids (in vitro and in vivo) [7-11]. The advantage of bioactive glasses and glass-ceramics among the different kinds of bioactive materials is the high speed of surface reactions that results in rapid bone formation [10-12]. Glasses and glass-ceramics, which are basically composed of SiO_2 , CaO , Na_2O , P_2O_5 , have been investigated due to their tunable bioactive behavior. The glass entitled 45S5 Bioglass[®] (with the composition of $45\text{SiO}_2\text{-}24.5\text{Na}_2\text{O}\text{-}24.5\text{CaO}\text{-}6\text{P}_2\text{O}_5$ (%wt)) is the most common bioactive glass reported by researchers [8, 13-17].

Recently, various glass-ceramics have been used by researchers for bone repair applications. Three major groups of glass-ceramics that have been examined are apatite-wollastonite, mica-apatite, and Ceravital[®] [8, 9, 13-18]. The crystalline fluorapatite phase is the most valuable phase for antibacterial and bioactive properties among these glass-ceramics [19-21]. Different methods have been proposed to create porosity in glass-ceramics such as foam synthesis, template synthesis, phase separation method, and freeze extrusion fabrication [22].

* Corresponding Author Email: m_rezvani@tabrizu.ac.ir (M. Rezvani)

The research has focused on the preparation and characterization of a macroporous bioactive glass-ceramic scaffold containing fluorapatite crystals. The fluorapatite phase has not been so far formed by any body in a combination that is nearly 45S5.

To this end, the template synthesis method was used to fabricate the porous structure because this method is the easiest way to control the pores size, the interconnectivity of the pores, and the size distribution of the pores [7, 22]. Moreover, starch was used as a porogen material for being easy crushing and economical.

The main factors affecting the final porous structure and its properties, which have been studied are the total solid loading, particle amount and size of starch powders, consolidation and burning out treatment, and sintering condition.

2. EXPERIMENTAL PROCEDURE

2.1. Synthesis of Glass Samples

The high purity commercially available powders were used as raw materials including Leached SiO₂ with high purity (>99), P₂O₅ (Merck 1005401000), Na₂CO₃ (Merck10639), CaCO₃ (Merck102069), and CaF₂ (Dau Jung 2508145). According to reaction 1, the required F ions were prepared by replacing some amounts of CaO with CaF₂. Therefore, the required CaO and F ions were produced simultaneously without changing the composition. As a result, the compositions were prepared with the following weight ratio (% wt) 40SiO₂, 12CaO, 16.71CaF₂, 21Na₂O, 15P₂O₅.



The glass frits were prepared by melting raw materials at 1450°C for 1h in an alumina crucible and quenched in cold water. The frits were dried and milled to particles with the size <40µm. The Fourier transform infrared (FT-IR) spectroscopy (Tensor27, braker, Germany) of the glass and glass-ceramic samples, was used to study the structural changes in the range of 400-1500 cm⁻¹. The thermal behavior of glass powders was determined through differential thermal analysis (DTA-Linseis L181) at the heating rate of 10°C.min⁻¹ and the crystalline phase precipitated during sintering were determined through x-ray diffraction (XRD) analysis (Siemens, model D-500). The microstructure of glass-ceramic samples was characterized by a scanning electron microscopy (FE-SEM, Mira-3Tescan).

2.2. Scaffold Fabrication

The scaffolds were fabricated through mixing starch particles and glass powders, with a thermally removable organic material as the pore former. The glass powders, which were sieved below 40µm and the starch (higher

than 99% purity) were carefully mixed for 20min in a plastic bottle using a rolling shaker to obtain an effective mixing. The obtained mixture was blended with 0.4wt% polyvinyl alcohol solution and then, pressed with uniaxial 500MPa pressure to form a pellet with 18mm diameter and 3mm thickness. Drying the pressed specimen was carried out with the gradual increase of the temperature to 100°C to prevent cracking caused by the sudden drying of the sample.

In this research, the amount of starch was varied in the range of 30-70 vol% to get the best balance between satisfactory sintering temperature, high porosity contact, porosity size, interconnectivity, and mechanical strength. Table 1 represents the experimental parameters applied to the production of each sample.

TABLE 1. Experimental parameters for the production of each sample

Sample code	Temperature(°C)	Starch (vol%)
GCF-615-P30	615	30
GCF-615-P40	615	40
GCF-615-P50	615	50
GCF-615-P60	615	60
GCF-615-P70	615	70
GCF-640-P30	640	30
GCF-640-P40	640	40
GCF-640-P50	640	50
GCF-640-P60	640	60
GCF-640-P70	640	70
GCF-665-P30	665	30
GCF-665-P40	665	40
GCF-665-P50	665	50
GCF-665-P60	665	60
GCF-665-P70	665	70

Finally, the total porosity, open porosity, and bulk density of the samples were investigated and the flexural strength was measured by three-point bending test (Zwieck Roell ZHV10, Germany). The scaffold was studied by the Scanning Electron Microscope (SEM) to evaluate the size, morphology, distribution, interconnectivity, and degree of sintering.

2.3. Chemical Degradation and Apatite Forming Ability

The bioactivity of the samples was evaluated using in vitro tests as explained by Kokubo et al. [23]. The biodegradation and apatite forming ability of the glass-ceramics were investigated by immersion of sintered glass-ceramic discs (with a diameter as much as 10mm) in 50ml simulated body fluid (SBF) solution at 37°C. The experiments were conducted at different time durations between 1 to 14 days. Each test was repeated for 3 times to ensure the accuracy of the results. The glass-ceramic sample was got out of the liquids after each test and then, pH and concentrations of Ca²⁺, P⁵⁺,

and Si^{4+} ions were measured using inductively coupled plasma-optical emission spectroscopy (ICP-OES). The apatite forming ability on glass-ceramic was studied through the XRD and SEM-EDS analysis.

3. RESULTS AND DISCUSSION

3.1. Crystallization of Glass Samples

DTA curves were studied to determine the crystallization temperatures. Figure 1 illustrates the DTA curves of the compositions after melting and quenching. The peaks of Fluorapatite phase ($\text{Ca}_{10}(\text{PO}_4)_6(\text{O}, \text{F}_2)$) (ICDD: 01-077-0120) appeared in the XRD patterns after heat-treating the samples at the first DTA peak temperature for 2h. Figure 2 presents the XRD patterns of glass and glass-ceramic samples. The XRD patterns showed that there were no unwanted phases in the glass sample and after heat-treatment of the samples. Moreover, the peaks of the crystalline phases appeared and the crystallization increased by increasing the temperature.

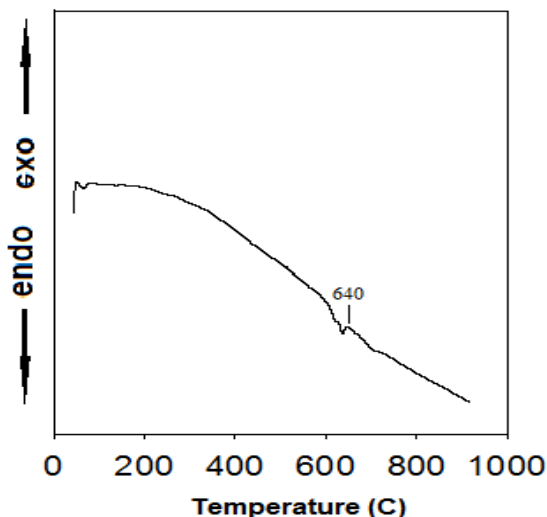


Figure 1. DTA curves of frits with a heating rate of $10^\circ\text{C}/\text{min}$

3.2. Structure of the Glass and Glass-ceramics

The FT-IR spectra of the glass and glass-ceramic samples are illustrated in Figure 3 after heat treatment at 615, 640, and 665°C [24]. The structural information about glass and glass-ceramic can be obtained from these spectra. There were clear peaks that proved the presence of SiO_4 tetrahedrons in the glass network due to the significant amount of SiO_2 in the composition of the samples. The peaks available at ~ 576.2 and $\sim 765.26\text{cm}^{-1}$ are attributed to the rocking and symmetric stretching vibrations of Si-O-Si bonds, respectively [25].

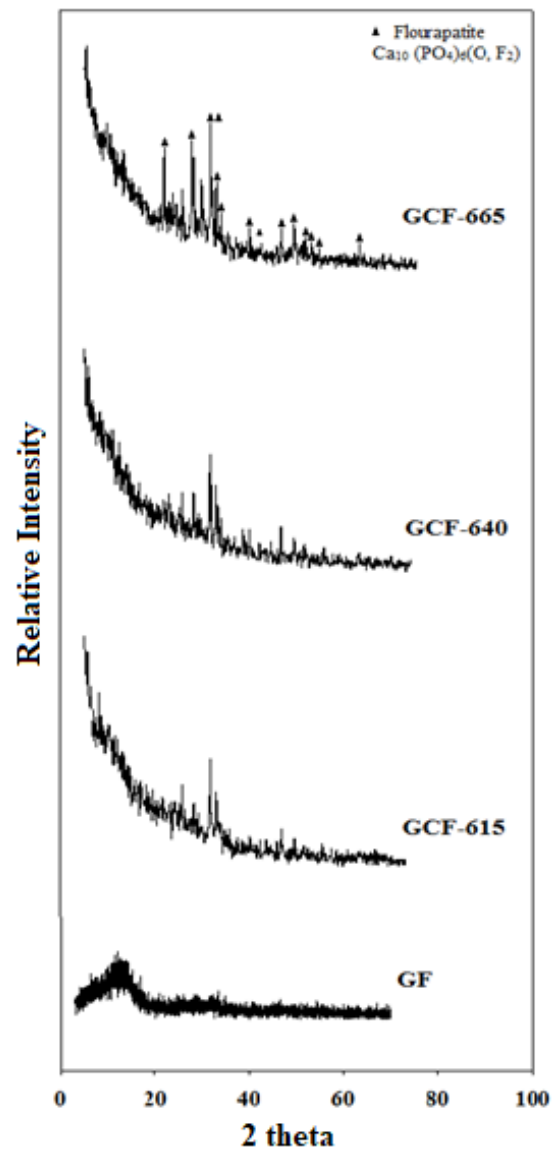


Figure 2. XRD patterns of glass and glass-ceramic heat-treated at different temperatures

As a consequence of overlapping with the rocking vibrations of Si-O-Si, the peaks of Ca-F bond were somehow difficult to be distinguished, although those peaks were reported at $\sim 468.30\text{cm}^{-1}$ [24, 26]. According to [14], it is possible to attribute the peak at $\sim 1025\text{cm}^{-1}$ to this bond. The peak visible in $\sim 1030.27\text{cm}^{-1}$ can also be attributed to the vibrations of Si-O-Ca bond, when the amount of Ca in the glass samples is high (due to the presence of CaF_2 and CaO , simultaneously). As it is reported, there are PO_3 groups due to the network forming the role of P_2O_5 and peaks available in ~ 577.67 and $\sim 1030\text{cm}^{-1}$ are attributed to PO_3 groups and P-O bonds [27, 28, 29]. It seems that these bonds were available in the samples, but overlapping with Si-O-Si and Si-O-Ca peaks made it difficult to be distinguished.

The intensity of the silicon structure peaks was higher in all investigated glass-ceramics than the base glass. These changes in the peaks can be attributed to a more regular four-dimensional SiO_4 arrangement, symmetric structure, and low-angle variation among the bonds. The intensity of the peaks in crystalline materials was more than amorphous [30].

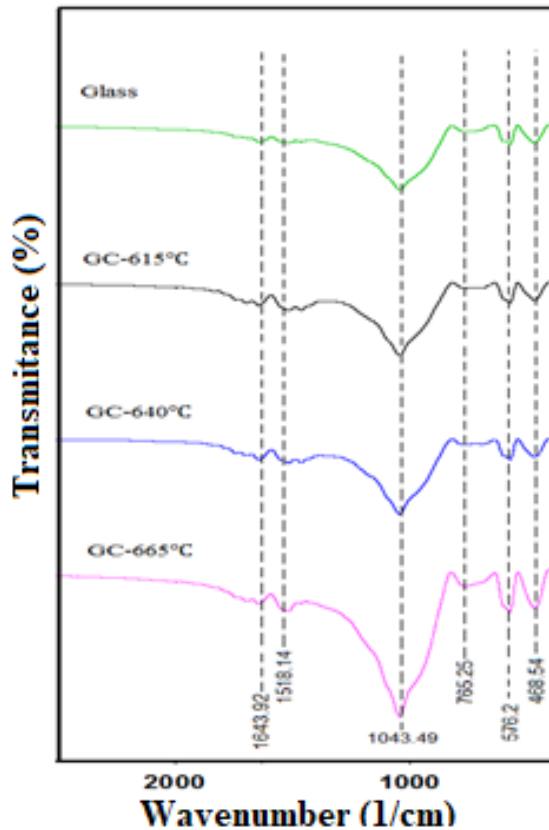


Figure 3. FT-IR spectra of the glass and glass-ceramics heat-treated at 615, 640 and 665°C

3.3. Microstructure Study of Glass-Ceramics

The microstructures of glass-ceramic samples, which were heat-treated at 665°C for 2h are illustrated in Figure 4. The obvious phase separation can be attributed to crystallization of fluorapatite. It also shows that the morphology of the fluorapatite phase is almost spherical.

Figure 5 shows the results of EDX analysis of bright areas (A in Figure 4) that are fluorapatite crystalline phase (since the peaks of calcium, fluorine, and phosphorus were observed in the EDX pattern).

3.4. Glass-Ceramic Scaffolds (Porosity and Mechanical Properties)

The heat treatment of the samples was performed at 615-665°C for 2 hours. The total porosity percentages of porous glass-ceramics are shown in Figure 6. The starch was added to glasses from 30 to 70 vol%.

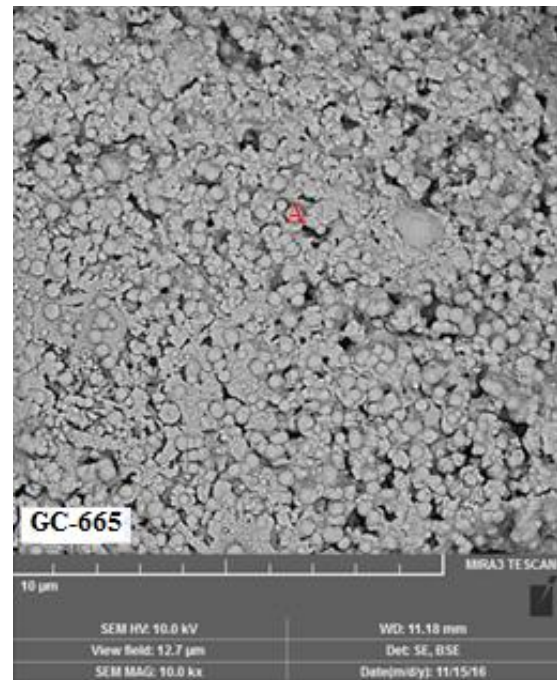


Figure 4. SEM image of glass-ceramic sample heat-treated at 665°C for 2h

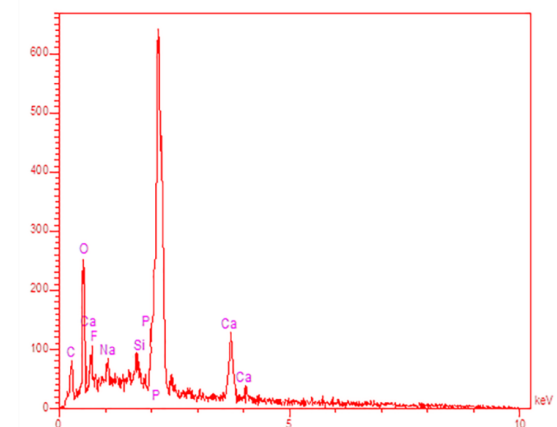


Figure 5. EDX spectrum of fluorapatite crystalline phase

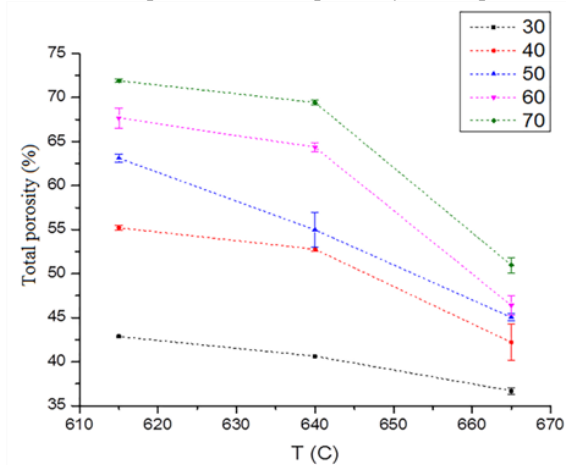


Figure 6. Total porosity percentage of glass-ceramic scaffolds heat-treated for 2h

It is clear that the amount of total porosity and open porosity decrease and the density increases with increasing of temperature and reducing of porogens. According to the results obtained in porous bodies, the GCF-615-P40 (Glass-ceramic fluorapatite, heat-treated at 615°C, starch 40 vol%), GCF-615-P50, GCF-615-P60, GCF-615-P70 samples had not a suitable strength. The flexural strength of the samples GCF-640-P40, GCF-640-P50, and GCF-665-P70 was about 12, 8, and 4MPa, respectively. Considering the previously reported flexural strength, the ranges of the samples are within the acceptable range [31-33].

The samples including GCF-640-P50 (with 58% porosity), GCF-640-P40 (with 55% porosity), and GCF-665-P70 (with 56% porosity) were selected as glass-ceramic scaffolds for bone body applications with acceptable appearance and porosity.

The results of obtained flexural strength showed that the strength of all three samples was in this range due to the flexural strength of the ideal scaffolds for porous bone in the range of 2-12MPa. On the other hand, this strength reduction can be attributed to the amount of starch although the porosities were close to each other. As was expected, the interconnectivity of porosities increases with increasing of starch, which cause a reduction in strength.

3.5. Microstructure Study of Glass-Ceramic Scaffold

The scanning electron microscopy images of the glass-ceramic scaffolds are shown in Figure 7.

According to the ideal scaffolds, the average pore size for bone is higher than 100µm. The results showed that the average pore size of all three samples is almost within this range, but only the sample GCF5-665-P70 has interconnection of porosities, which is due to the high amount of porosity. Therefore, the GCF-665-P70 was selected as the appropriate porous scaffold body.

3.6. The Ability of Apatite Forming and Biodegradation

Variations of ion concentration with immersion time were investigated for various ionic species (Ca^{2+} , P^{5+} , Si^{4+}) and the results are presented in Figure 8.

The important points of this test are as below:

i) Higher concentrations of Ca were observed at longer immersion times in Figure 8a for the glass-ceramic leading to maximum leaching ability and surface reactivity of the respective glass-ceramic. The higher concentration of Ca in SBF at longer soaking times indicates that the modifier cations in the glass are no more exchanged with hydronium ions in the external solution (i.e. the inhibition of the biomineralization process) [34, 35].

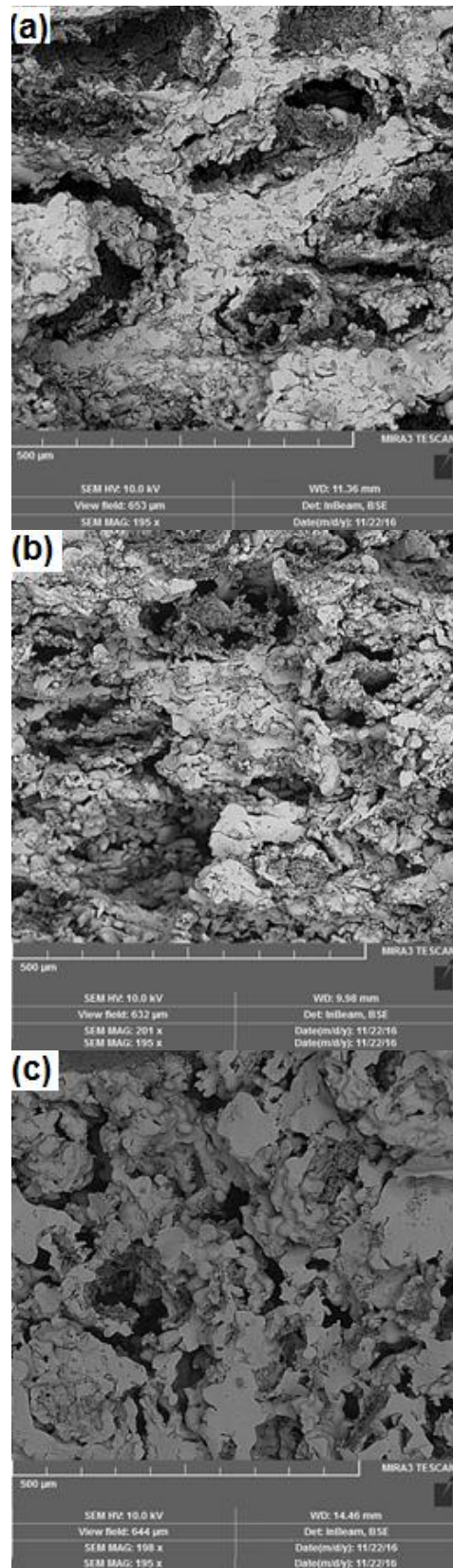


Figure 7. SEM images of glass-ceramic scaffolds a) GCF-640-P40 b) GCF-640-P50 c) GCF-665-P70, (All were heat-treated for 2 h)

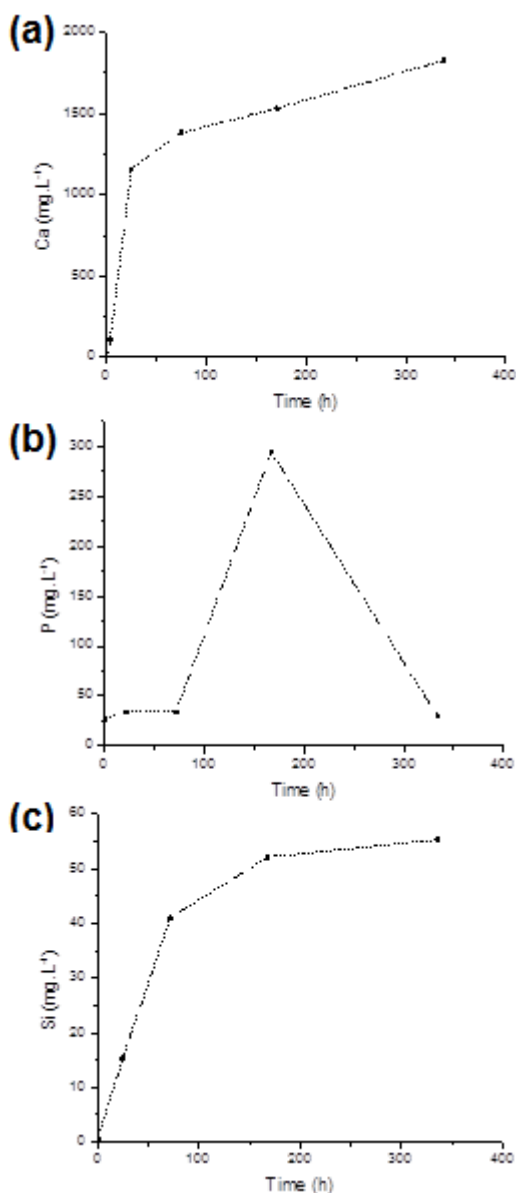


Figure 8. ICP plots of elemental concentration of (a) Ca, (b) P, and (c) Si, in SBF solution versus immersion time for the investigated GCs

ii) The sample exhibited higher concentration of phosphorus for the glass-ceramic Figure 8b once soaked in SBF, so that the highest phosphorus concentration was achieved after 7 days of soaking, beyond which time significantly lower concentrations were observed. The initial increase in the concentration of phosphorus might be related to two reasons including (1) the release of excessive soluble phosphate species, or (2) the rapid hydrolysis of low amounts of labile P–O–Si bridges from the remaining glassy phase in the fluid. These might have brought about two implications including (1) the local super-saturation of the solution, thereby

facilitating the process via which, the HA content of the solution is precipitated, and/or (2) providing a buffer and hence, reducing surface acidity, which in turn would inhibit the bone-bonding [36, 37].

Moreover, it seems that the increase in the concentration of phosphorus occurs simultaneously with the initial stage of the reactivity mechanism features during which, the Si-OH groups was developed on the glass surface. At the other end of the spectrum, the lower concentration of phosphate following the maximum (Figure 8c) has been found to be linked to the movement of phosphorus ions to the glass surface where a layer of high calcium phosphate content was developed [34, 35].

iii) The higher concentration of Si ion was observed in the SBF solution with increasing the soaking time. Indeed, the surface Si-OH groups developed during the hydrolysis of the Si-O-Si contribute to the higher bioactivity of the resultant compound upon the decrease in silica content of glass-ceramic indirectly, which results in attenuating the hydroxyapatite-glass-ceramic interface energy [38].

Figure 9 demonstrates the SEM images of glass-ceramic samples after various soaking times in SBF solution. According to the images, an appetite-like layer was developed and well-grown on the surface of the samples following 14 days of soaking in SBF. According to the results of EDX analysis (Figure 10), phosphorus and calcium were the main constituents of these agglomerates. The weak Si peak could be attributed to the high content of SiO₂ in the layer developed on the bioactive surface [15, 39, 40].

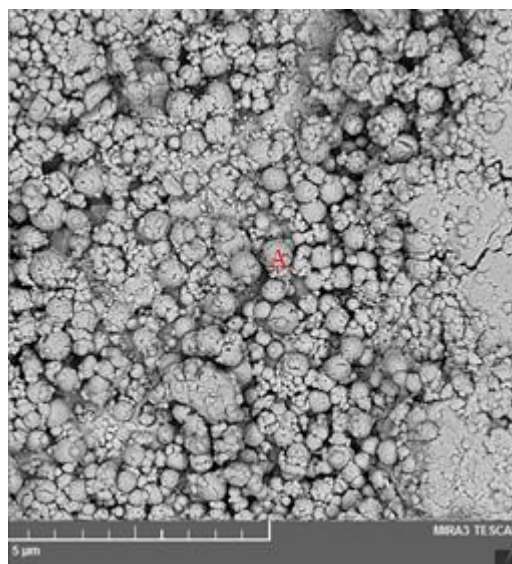


Figure 9. SEM image of glass-ceramic sample after immersion for 14 days in SBF solution (13000×)

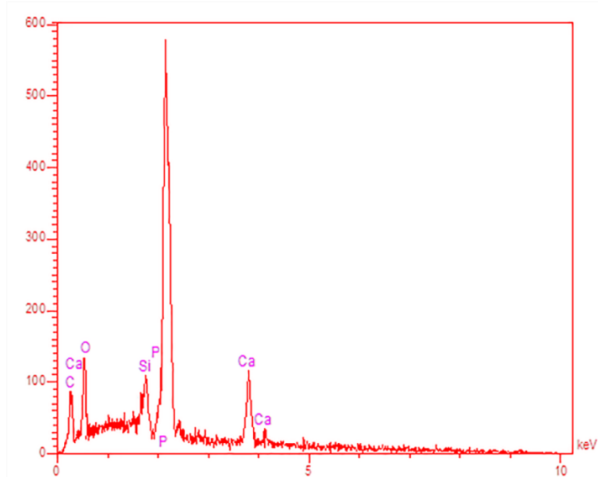


Figure 10. EDX analysis of glass-ceramic sample after 14 days of immersion in SBF solution (A area)

4. CONCLUSION

The purpose of this research was to prepare and characterize a macroporous glass-ceramic scaffold containing fluorapatite crystalline phase with composition near to 45S5. Macroporous bioactive glass-ceramic scaffolds were successfully obtained and the results of XRD, FTIR, and SEM analyses showed that the fluorapatite phase was formed and its amount increases with increasing the temperature.

The correct selection of the sintering temperature as well as the amount of progen materials leads to a well-sintered specimen with good compromising between strength and highly porous structure. Furthermore, the prepared scaffold showed excellent bioactive behavior. In fact, in vitro studies showed that the CEL2 coating had high bioactivity due to the formation of a hydroxyapatite layer on its surface.

REFERENCES

1. Bravarone, C. V., Verné, E., Appendino, P., "Macroporous bioactive glass-ceramic scaffolds for tissue engineering", *Journal of Materials Science: Materials in Medicine*, Vol. 17, No. 11, (2006), 1069-1078. <https://doi.org/10.1007/s10856-006-0533-8>
2. Mortera, R., Onida, B., Fiorilli, S., Cauda, V., Bravarone, C. V., Bains, F., Verné, E., Garrone, E., "Synthesis and Characterization of MCM-41 spheres inside bioactive glass-ceramic scaffold", *Chemical Engineering Journal*, Vol. 137, No. 1, (2008), 54-61. <https://doi.org/10.1016/j.cej.2007.07.094>
3. Renghini, C., Komlev, V., Fiori, F., Verné, E., Bains, F., Vitale-Bravarone, C., "Micro-CT studies on 3-D bioactive glass-ceramic scaffolds for bone regeneration", *Acta Biomaterialia*, Vol. 5, No. 4, (2009), 1328-1337. <https://doi.org/10.1016/j.actbio.2008.10.017>
4. Vitale Bravarone, C., Bains, F., Verné, E., "Feasibility and tailoring of bioactive glass-ceramic scaffolds with gradient of porosity for bone grafting", *Journal of Biomaterials Applications*, Vol. 24, No. 8, (2010), 693-712. <https://doi.org/10.1177/0885328209104857>
5. Jones, J. R., Hench, L. L., "Bioactive 3D scaffolds in regenerative medicine: the role of interface interactions" In *Surfaces and Interfaces for Biomaterials*, Woodhead Publishing, (2005), 545-572. <https://doi.org/10.1533/9781845690809.4.545>
6. Jones, J. R., "Review of bioactive glass: From Hench to hybrids", *Acta Biomaterialia*, Vol. 9, No. 1, (2013), 4457-4486. <https://doi.org/10.1016/j.actbio.2012.08.023>
7. Vitale-Bravarone, C., Bains, F., Miola, M., Mortera, R., Onida, B., Verné, E., "Glass-ceramic scaffolds containing silica mesophases for bone grafting and drug delivery", *Journal of Materials Science: Materials in Medicine*, Vol. 20, No. 3, (2009), 809-820. <https://doi.org/10.1007/s10856-008-3635-7>
8. El-Meleigy, E., Van Noort, R., *Glasses and Glass Ceramics for Medical Application*, Springer science & business media, New York, (2012). <https://doi.org/10.1007/978-1-4614-1228-1>
9. Anand, V., Singh, K. J., Kaur, K., "Evaluation of zinc and magnesium doped 45S5 mesoporous bioactive glass system for the growth of hydroxyl apatite layer", *Journal of Non-Crystalline Solids*, Vol. 406, (2014), 88-94. <https://doi.org/10.1016/j.jnoncrysol.2014.09.050>
10. Gerhardt, L. C., Boccaccini, A. R., "Bioactive glass and glass-ceramic scaffolds for bone tissue engineering", *Materials*, Vol. 3, No. 7, (2010), 3867-3910. <https://doi.org/10.3390/ma3073867>
11. Kansal, I., Goal, A., Tulyaganov, D. U., Rajagopal, R. R., Ferreira, José M. F., "Structural and thermal characterization of CaO-MgO-SiO₂-P₂O₅-CaF₂ glasses", *Journal of the European Ceramic Society*, Vol. 32, No. 11, (2012), 2739-2746. <https://doi.org/10.1016/j.jeurceramsoc.2011.10.041>
12. Wu, C., Chang, J., "Mesoporous bioactive glasses: structure characteristics, drug/growth factor delivery and bone regeneration application", *Interface Focus*, Vol. 2, No. 3, (2012), 292-306. <https://doi.org/10.1098/rsfs.2011.0121>
13. Bellucci, D., Cannillo, V., Sola, A., Chiellini, F., Gazzarri, M., Migone, C., "Macroporous bioglass®-derived scaffolds for bone tissue regeneration", *Ceramics International*, Vol. 37, No. 5, (2011), 1575-1585. <https://doi.org/10.1016/j.ceramint.2011.01.023>
14. Bellucci, D., Sola, A., Cannillo, V., "Bioactive glass-based composites for the production of dense sintered bodies and porous scaffolds", *Materials Science and Engineering: C*, Vol. 33, No. 4, (2013), 2138-2151. <https://doi.org/10.1016/j.msec.2013.01.029>
15. Fiorilli, S., Bains, F., Cauda, V., Crepaldi, M., Vitale-Bravarone, C., Demarchi, D., Onida, B., "Electrophoretic deposition of mesoporous bioactive glass on glass-ceramic foam scaffolds for bone tissue engineering", *Journal of Materials Science: Materials in Medicine*, Vol. 26, No. 1, (2015), 21. <https://doi.org/10.1007/s10856-014-5346-6>
16. Adams, L. A., Essien, E. R., Adesalu, A. T., Julius, M. L., "Bioactive glass 45S5 from diatom biosilica", *Journal of Science: Advanced Materials and Devices*, Vol. 2, No. 4, (2017), 476-482. <https://doi.org/10.1016/j.jsamd.2017.09.002>
17. Hench, L. L., Wilson, J., *An Introduction to Bioceramics, advanced series in ceramics*, Vol. 1, Singapore: World Scientific, (1993). <https://doi.org/10.1142/2028>
18. Peitl, O., Zanotto, E. D., Serbena, F. C., Hench, L. L., "Compositional and microstructural design of highly

- bioactive P_2O_5 - Na_2O - CaO - SiO_2 glass-ceramics”, *Acta Biomaterialia*, Vol. 8, No. 1, (2012), 321-332. <https://doi.org/10.1016/j.actbio.2011.10.014>
19. Clupper, D. C., Hench, L. L., Mecholsky, J. J., “Strength and toughness of tape cast bioactive glass 45S5 following heat treatment”, *Journal of the European Ceramic Society*, Vol. 24, No. 10-11, (2004), 2929-2934. [https://doi.org/10.1016/s0955-2219\(03\)00363-7](https://doi.org/10.1016/s0955-2219(03)00363-7)
 20. Du, R., Chang, J., “Preparation and characterization of bioactive sol-gel-derived $Na_2Ca_2Si_3O_9$ ”, *Journal of Materials Science: Materials In Medicine*, Vol. 15, No. 12, (2004), 1285-1289. <https://doi.org/10.1007/s10856-004-5736-2>
 21. Lefebvre, L., Chevalier, J., Gremillard, L., Zenati, R., Thollet, G., Bernache-Assollant, D., Govin, A., “Structural transformations of bioactive glass 45S5 with thermal treatments”, *Acta Materialia*, Vol. 55, No. 10, (2007), 3305-3313. <https://doi.org/10.1016/j.actamat.2007.01.029>
 22. Ji, L., Si, Y., Li, A., Wang, W., Qiu, D., Zhu, A., “Progress of three-dimensional macroporous bioactive glass for bone regeneration”, *Frontiers of Chemical Science and Engineering*, Vol. 6, No. 4, (2012), 470-483. <https://doi.org/10.1007/s11705-012-1217-1>
 23. Kokubo, T., Takadama, H., “How useful is SBF in predicting in vivo bone bioactivity?”, *Biomaterials*, Vol. 27, No. 15, (2006), 2907-2915. <https://doi.org/10.1016/j.biomaterials.2006.01.017>
 24. Allahgoliyane, E., Rezvani, M., “Investigating the affect Factors in Manufacturing process of Porous Ceramic Glass Containing Crystalline Fluorapatite”, In *12th ICERS Congress Proceedings*, Iran, 30th April & 1st May 2019, Iranian Ceramic Society, (2019).
 25. Farahinia, L., Rezvani, M., Alahgoliyan, E., “Optical characterization of oxyfluoride glasses containing different amounts of K_2O additive”, *Materials Research Bulletin*, Vol. 70, (2015), 461-467. <https://doi.org/10.1016/j.materresbull.2015.05.015>
 26. Tahvildari, K., Esmaceli Pour, M., Ghammamy, S., Nabipour, H., “ CaF_2 Nanoparticles: Synthesis and characterization”, *International Journal of Nano Dimension*, Vol. 2, No. 4, (2012), 269-273. <https://doi.org/10.7508/ijnd.2011.04.008>
 27. Peitl, O., Zanutto, E. D., Hench, L. L., “Highly bioactive P_2O_5 - Na_2O - CaO - SiO_2 glass-ceramics”, *Journal of Non-Crystalline Solids*, Vol. 292, No. 1-3, (2001), 115-126. [https://doi.org/10.1016/s0022-3093\(01\)00822-5](https://doi.org/10.1016/s0022-3093(01)00822-5)
 28. Ghomi, H., Fathi, M. H., Edris, H., “Fabrication and characterization of bioactive glass/hydroxyapatite nanocomposite foam by gelcasting method”, *Ceramics International*, Vol. 37, No. 6, (2011), 1819-1824. <https://doi.org/10.1016/j.ceramint.2011.03.002>
 29. Majhi, M. R., Pyare, R., Singh, S. P., “Studies on preparation and characterizations of CaO - Na_2O - SiO_2 - P_2O_5 bioglass-ceramics substituted with Li_2O , K_2O , ZnO , MgO , and B_2O_3 ”, *International Journal of Scientific & Engineering Research*, Vol. 2, No. 9, (2011), 1-9. https://www.ijser.org/paper/Studies_on_preparation_and_charac terizations.html
 30. Doweidar, H., El-Damrawi, G., Mansour, E., Fetouh, R. E., “Structural role of MgO and PbO in MgO - PbO - B_2O_3 glasses as revealed by FT-IR: a new approach”, *Non-Crystalline Solids*, Vol. 358, No. 5, (2012), 941-946. <https://doi.org/10.1016/j.jnoncrsol.2012.01.004>
 31. Thompson, I. D., Hench, L. L., “Mechanical properties of bioactive glasses, glass-ceramics and composites”, *Proceedings of the Institution of Mechanical Engineers, Part H: Journal of Engineering in Medicine*, Vol. 212, No. 2, (1998), 127-136. <https://doi.org/10.1243/0954411981533908>
 32. Crovace, M. C., Souza, M. T., Chinaglia, C. R., Peitl, O., Zanutto, E. D., “Biosilicate® - A multipurpose, highly bioactive glass-ceramic. In vitro, in vivo and clinical trials”, *Journal of Non-Crystalline Solids*, Vol. 432, (2016), 90-110. <https://doi.org/10.1016/j.jnoncrsol.2015.03.022>
 33. Vyas, V. K., Kumar, A. S., Singh, S. P., Pyare, R., “Effect of nickel oxide substitution on bioactivity and mechanical properties of bioactive glass”, *Bulletin of Materials Science*, Vol. 39, No. 5, (2016), 1355-1361. <https://doi.org/10.1007/s12034-016-1242-7>
 34. Jones, J. R., Sepulveda, P., Hench, L. L., “Dose-dependent behavior of bioactive glass dissolution”, *Journal of Biomedical Materials Research: An Official Journal of The Society for Biomaterials, The Japanese Society for Biomaterials, and The Australian Society for Biomaterials and the Korean Society for Biomaterials*, Vol. 58, No. 6, (2001), 720-726. <https://doi.org/10.1002/jbm.10053>
 35. Oliveira, J. M., Correia, R. N., Fernandes, M. H., “Surface modifications of a glass and a glass-ceramic of the MgO - $3CaO$ - P_2O_5 - SiO_2 system in a simulated body fluid”, *Biomaterials*, Vol. 16, No. 11, (1995), 849-854. [https://doi.org/10.1016/0142-9612\(95\)94146-c](https://doi.org/10.1016/0142-9612(95)94146-c)
 36. Karlsson, K. H., Fröberg, K., Ringbom, T., “A structural approach to bone adhering of bioactive glasses”, *Journal Non-Crystal Solids*, Vol. 112, No. 1-3, (1989), 69-72. [https://doi.org/10.1016/0022-3093\(89\)90495-x](https://doi.org/10.1016/0022-3093(89)90495-x)
 37. Zhang, H., Ye, X. J., Li, J. S., “Preparation and biocompatibility evaluation of apatite/wollastonite-derived porous bioactive glass ceramic scaffolds”, *Biomedical Materials*, Vol. 4, No. 4, (2009), 045007. <https://doi.org/10.1088/1748-6041/4/4/045007>
 38. Tilocca, A., Cormack, A. N., de Leeuw, N. H., “The formation of nanoscale structures in soluble phosphosilicate glasses for biomedical applications: MD simulations”, *Faraday Discussions*, Vol. 136, (2007), 45-55. <https://doi.org/10.1039/b617540f>
 39. Bains, F., Verné, E., Vitale-Brovarone, C., “Feasibility, tailoring and properties of polyurethane/bioactive glass composite scaffolds for tissue engineering”, *Journal of Materials Science: Materials In Medicine*, Vol. 20, No. 11, (2009), 2189-2195. <https://doi.org/10.1007/s10856-009-3787-0>
 40. Hashmi, M. U., Shah, A. S., Elkady, A. S., “Effect of sintering time on crystallization, densification and in-vitro characteristics of bioactive glass ceramics”, *International Journal of Engineering Science and Innovative Technology*, Vol. 3, No. 1, (2014), 368-377. <https://citeseerx.ist.psu.edu/viewdoc/download?doi=10.1.1.1047.2168&rep=rep1&type=pdf>



Investigation of Microstructure, Hardness, and Corrosion Resistance of Ni-P-GO Electroless Nanocomposite Coating on AZ31D Alloy Surface

M. Hanachi^a, Z. S. Seyedraoufi^{a*}, V. Abouei^a

^a Department of Metallurgy and Materials Engineering Karaj Branch, Islamic Azad University, Karaj, Alborz, Iran

PAPER INFO

Paper History:

Received 31 May 2020
Accepted in revised form 26 July 2020

Keywords:

Electroless
Phosphorus Content
Ni-P-GO Nanocomposite Coating
Cauliflower
Corrosion

ABSTRACT

In the present study, the Ni-P-GO nanocomposite coating was applied to the surface of AZ31D alloy through electroless plating process. To achieve the nanocomposite coating, 5 g/L Graphene Oxide (GO) was added to the plating bath. By changing the pH of the bath, coatings were created in three ranges of low, medium, and high phosphorus on the surface of AZ31D. According to the results, by increasing the phosphorus content, the amount of graphene oxide absorbed in the coating increased. Microstructural examination by Scanning Electron Microscopy (SEM) showed that all coatings formed on the substrate had the cauliflower morphology. Phase analysis of the coating by X-Ray Diffraction (XRD) showed that at a low phosphorus level, the coating is semi-amorphous; however, with increasing phosphorus content, the coating becomes completely crystalline. The highest hardness value of the specimen was observed with the lowest amount of phosphorus. The microhardness measurements showed that the hardness decreased with increasing the amount of phosphorus so that the minimum hardness of the specimen containing 14.97 wt.% phosphorus was measured at 521 H₅₀. Contrary to the morphology, phosphorus levels have a significant effect on the structure and hardness of Ni-P-GO nanocomposite coatings. As the amount of phosphorus increased, the corrosion resistance of the coating increased. This is attributed to the reduction of the current of corrosion and more positive potential values.

1. INTRODUCTION

Weight reduction has always been the concern of industry. That is the reason why every year more and more researchers, designers, and craftsmen are turning to use lighter materials. Magnesium and its alloys are among the materials that are widely used to meet the needs of the aerospace, automotive, military, and medical industries due to their low weight. The high strength-to-weight ratio and low density are the main reasons for the importance of magnesium alloys. Poor resistance to abrasion and corrosion is the Achilles's heel of magnesium alloys. Therefore, these shortcomings have challenged the frequent use of this material [1-4].

Every year, various methods such as thermal spraying, veneering, work surface friction, surface processing, and composite fabrication by turbulent friction process, sol-gel, and electroless and electrical plating are used to improve the surface properties of magnesium alloys [5-10]. Electroless plating is usually considered as the first option due to the low cost of the process, the uniform

layer created, and the abrasion and corrosion resistance of the formed layer.

Electroless coatings usually based on nickel, copper, cobalt, silver, and serum are formed on the surface of the part according to the user's needs. Nickel-based coatings are divided into three types according to the type of bath and the composition of the layer created: nickel, nickel-boron, and nickel-phosphorus electroless coatings [11]. To improve the properties of these coatings, they are usually either alloyed with Mo, Co, Cr, and Cu elements, or form composite through secondary phases [12]. These two approaches both in amorphous and crystalline states lead to increased hardness and wear resistance of the coating.

Due to the short duration of the electroless process, these coatings are formed in the amorphous state. Through heat treatment, the amorphous structure becomes crystalline and the energy for the formation of intermediate phases (nickel-phosphorus intermetallic compounds) is supplied [13]. Crystallization and distribution of intermediate phases increase the hardness and wear resistance of the coating [13]. Recent research has shown that the addition

* Corresponding Author Email: z.seyedraoufi@kia.ac.ir (Z. S. Seyedraoufi)

of graphene oxide nanoparticles increases wear resistance by reducing the coefficient of friction, which is increased by heat treatment at 400°C [14,15].

However, previous researchers have expressed opposing views on either adverse effects or positive effects of heat treatment on the corrosion resistance of nickel-phosphorus coatings.

In the present study, Ni-P-GO composite electroless coatings with different amounts of phosphorus were formed on AZ31D alloy surface. The aim of this study was to achieve the optimal amount of phosphorus to achieve the highest values of hardness and corrosion resistance by formation of composite coating with graphene oxide (GO) nanoplates.

Electroless plating coatings in acidic baths are difficult to form on a magnesium substrate. Therefore, this research is one of the few researches carried out to create electroless nanocomposite coating on magnesium substrate.

2. MATERIALS AND METHODS

In this study, the AZ31D magnesium-based alloy plate purchased from Iranian company of NOVIN RAHYAFT with dimensions of 20 × 20 × 5 mm was used as a substrate. The chemical composition of the alloy is shown in Table 1. GO was used to fabricate Nickel-phosphorus composite coating. GO was purchased from Indian company of UNITED NANOTECH INNOVATIONS. Specifications of graphene oxide nanoplates are presented in Table 2.

TABLE 1. The chemical composition of the substrate obtained from quantummetry

El.	Mg	Al	Zn	Mn	Sn	Fe	Ni
wt.%	Base	3.38	1.19	0.44	0.01	0.005	0.005

TABLE 2. Specifications of graphene oxide nanoplates

Lateral Dimensions (µm)	Density (g/cc)	Surface Space (BET) (m ² /g)	Layers number	Purity (%)	Thickness (nm)
5-10	0.42	Less than 120	8-10	99.999	3-6

Specimens were polished by SiC abrasive papers up to No. 1200. Polished specimens were washed with acetone and then, with distilled water. After washing, the specimens were air-dried to obtain a clean surface with suitable surface roughness. Finally, the following steps were performed to activate the specimens in accordance with ASTM B480 standard:

a) Primary cleaning with detergent and water.

b) Degreasing with acetone in an ultrasonic bath for 20 minutes.

c) Chromate conversion coating in 25% chromic acid with 11% nitric acid for 40 seconds.

d) Removal of surface oxide films in a mixture of 5.5% fluoride acid (HF) for 10 minutes.

After each step, the specimens were washed in distilled water and in the final step, they were immediately immersed in an electroless bath. To make composite coating, 5 g/L GO was added to the plating bath. In order to facilitate the plating process, some part of the specimens (substrate) was drilled so that it could be easily placed in the bath. The chemical composition of the bath used in this study is shown in Table 3.

TABLE 3. Composition of plating bath for Ni-P coating on AZ31D alloy surface

Chemical Compounds	NiSO ₄ ·6H ₂ O (g/L)	NaH ₂ PO ₄ ·H ₂ O (g/L)	CH ₃ COONa (g/L)	Lactic acid (ml/L)
Concentration	30	25	25	20

The plating process was performed in the temperature range of 85 to 90°C. Due to the oxidation of magnesium specimens during the electroless process, 0.6% HF was added to the solution before starting the coating process. This solution was placed in an ultrasonic bath for 1 hour to obtain a suitable dispersion of GO particles in the solution.

Ni-P coating was formed in baths with acidic conditions, and the hardness of this coating was completely affected by pH variations; therefore, pH control of these solutions is very important [11]. As the precipitate forms, the pH of the solution changes over time, regularly controlled by adding dilute NaOH. Due to the high potential of the substrate, applying Ni-P coating to the AZ31D alloy requires a catalyst to initiate the chemical reaction. A small iron nail was used as the reaction catalyst. The catalyst was placed in the plating bath for 20 seconds at the specified temperature and pH. After the electroless solution reached the desired temperature and pH, a magnetic stirrer system at 350 rpm was used to prevent the particles from settling in the bath during the plating process. The electroless process was performed for one hour. In this study, Ni-P electroless coatings with three phosphorus percentages of P < 6%, P = 6-10%, and P > 10% were used and pH values were fixed at 3.5, 4.5, and 5.5 during the formation of electroless Ni-P coating. Microstructural features of the coated specimens were analyzed. The X-ray diffraction pattern was obtained by the Dutch Philips X-pert device using a Cu K α lamp with a wavelength of $\lambda = 1.542 \text{ \AA}$ at an angle of 20 to 80 degrees with step size = 0.02. The resulting patterns were analyzed by Xpert software to identify each of the possible phases.

To investigate the microstructure, a scanning electron microscope manufactured by the Czech company TESCAN model VEGA TS5130MM with a working voltage of 20.00 kV was used. Secondary electron mode was used for imaging. In addition, the device was equipped with elemental analysis using X-ray EDS, which was used for the elemental exploration of the coating surface or any specific point of the coating. Corrosion resistance of all specimens including substrate, plated, and heat treated specimens was investigated. The corrosion test was performed by the EG & G 263A Potentiostat/Galvanostat Instrument in the environment and with Saturated Calomel reference Electrode (SCE). Platinum used as an auxiliary electrode and the coated steel substrate as a working electrode were placed in NaCl solution with 3.5% concentration. In this test, the desired parts were exposed to corrosive environment (coated parts) and the rest of the surface of the specimens was covered with varnish. The scanning speed of potential of 1 mV/s in the range of ± 400 mv around the open circuit potential was considered in polarization tests. Prior to measurement, the specimens were placed in corrosive environment for one hour to establish the potential of the open circuit.

3. RESULTS AND DISCUSSION

Fig. 1 shows the SEM morphological images of nickel-phosphorus-oxide graphene coatings with different amounts of phosphorus. What is clear in all three parts of Fig. 1 is the formation of the nanocomposite coating with the morphology of the cauliflower. This type of coating is common to all electroless coatings [16]. Due to the presence of porosity between the colonies, this structure has self-lubrication properties and shows good abrasion resistance [11, 13]. The size of colonies is affected by process parameters [17].

Given that all process variables have been constant, this change in colony size can be considered as a function of phosphorus content. As shown in Fig. 2, increasing the

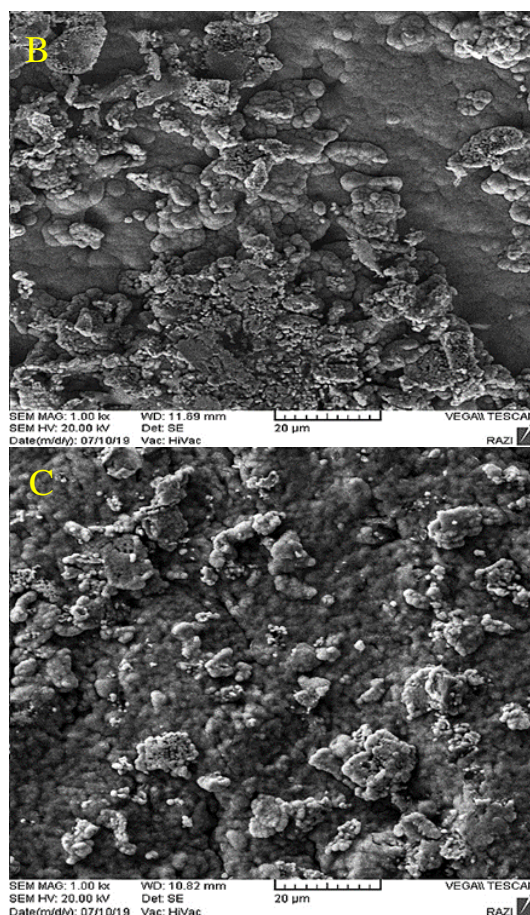
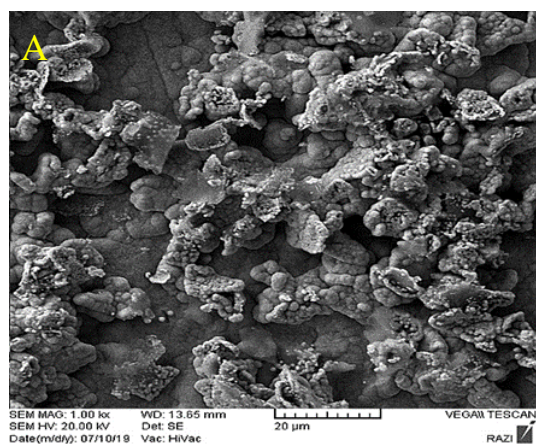


Figure 1. SEM images of nickel-phosphorus-graphene oxide nanocomposite coatings (A) less than 6% phosphorus (B) 6 to 10% phosphorus (C) more than 10% phosphorus

amount of phosphorus has led to a decrease in the size of colonies, which can be attributed to an increase in the nucleation sites in the coating and a decrease in the crystallite sizes. Each colony is made up of millions of crystallites [17].

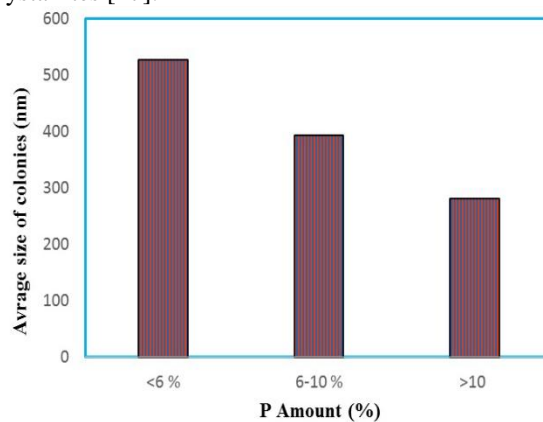


Figure 2. The relation between the amount of phosphorus in the nickel-phosphorus-graphene oxide nanocomposite coatings and coating colonies

Table 4 shows the local analysis results of the area marked with a yellow square in Figure 1. It should be noted that as shown in Table 4, the amount of graphene oxide absorbed in the coating has increased with increasing phosphorus content. Increasing the amount of carbon and oxygen in the EDS results confirms this fact. The reason for this is the greater tendency of phosphorus than nickel to react with carbon.

TABLE 4. EDS results of Ni-P-GO nanocomposite coatings

Specimens	Amount of Elements		
	Element	Wt. %	At. %
P < 0.6%	Ni	80.15	64.85
	P	5.21	12.14
	C	1.98	4.07
	O	12.66	19.21
6-10 % P	Ni	73.12	50.21
	P	7.66	15.91
	C	2.31	7.17
	O	16.91	26.71
P > 10%	Ni	61.72	41.41
	P	14.97	18.18
	C	4.04	13.30
	O	19.27	27.11

Fig. 3 shows the SEM images of the cross-sectional area of the coatings. All coatings are uniformly formed on the substrate surface. One of the characteristics of electroless coatings is their uniformity. Due to the lack of external flow during the application of these coatings, there is no accumulation of flow in sharp points or no uniformity in some parts of the coating [18]. It seems that during the process and nucleation of the first points in the coating, a reaction has taken place between the magnesium substrate and the nickel-based coating which concludes in the formation of a very thin intermetallic layer (Mg_2Ni). The formation of an intermetallic compound between nickel and magnesium does not require high energy and temperature according to the literature [19]. As the coating forms and the amount of magnesium in the substrate decreases, the coating becomes rich in nickel and the formation of the coating returns to its normal state.

In Figure 4, elemental mapping image of Ni, P, and C in the medium phosphorus coating is shown. As can be seen, the carbon element that characterizes graphene oxide is well distributed in different parts of the coating. On the other hand, Figure 4 shows that phosphorus is also well distributed in a nickel matrix.

Fig. 5 shows the XRD patterns of all three coatings. As shown, at the highest phosphorus level, the coating is formed in the crystalline state with a small amount of amorphous phase on the substrate surface. The intermetallic compound created on the substrate discussed in the previous section is well illustrated in the

XRD results. Fig. 5 shows also the XRD pattern of the specimen with moderate phosphorus. In this image, it is clear that the amorphous phase located at 45 degrees has reached a minimum.

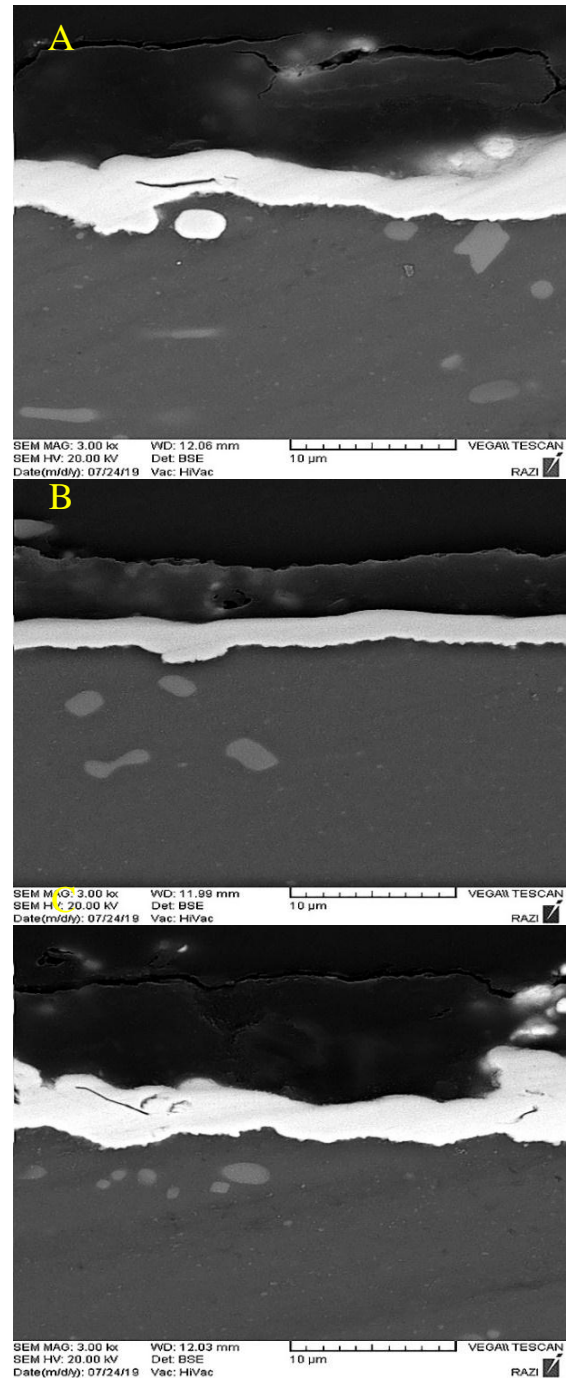


Figure 3. Cross-sectional SEM images of nickel-phosphorus-graphene oxide nanocomposite coatings (A) less than 6% phosphorus (B) 6 to 10% phosphorus (C) more than 10% phosphorus

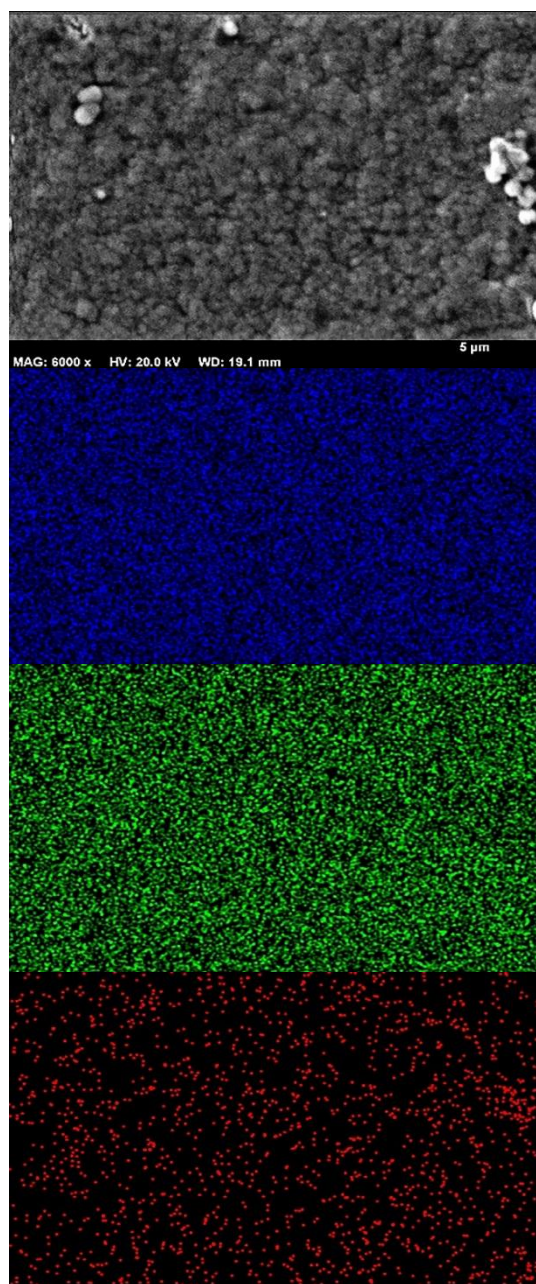


Figure 4. Elemental mapping images of Ni(blue), P(green), and C(red) in the medium phosphorus coating

As the pH of the bath decreases, the amount of phosphorus in the coating decreases. As shown in the XRD pattern images, the crystallinity has also intensified with lowering the phosphorus content. It is stated in the literature that increasing the amount of phosphorus or boron increases the possibility of amorphous coating due to rise in segregation of alloying elements [20]. It is also observed that the amount of nickel-phosphorus intermetallic compound (Ni_2P) has increased for higher phosphorus content.

As shown in Table 4, with increasing phosphorus content, the amount of graphene oxide absorbed in the

coating has increased. Increasing the amount of carbon and oxygen in the EDS results confirms this.

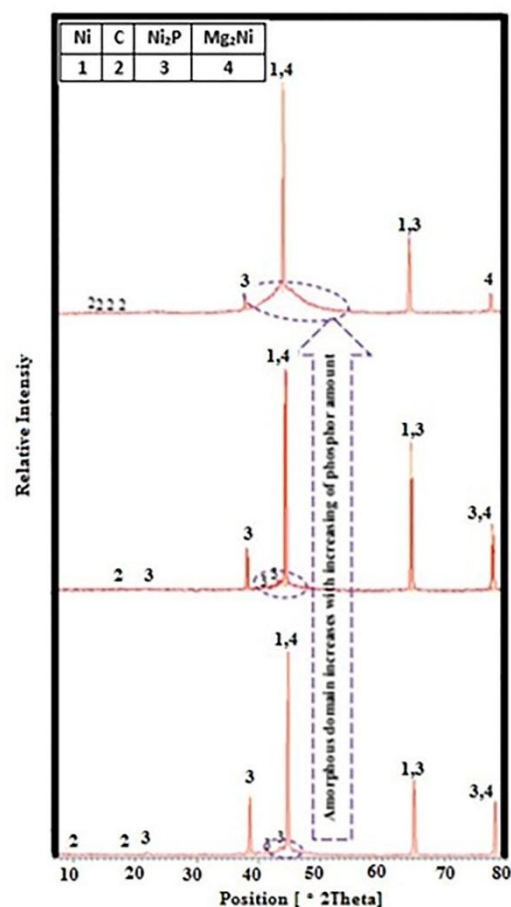
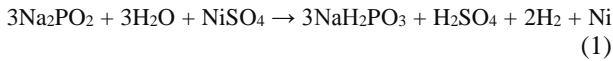


Figure 5. XRD pattern of nickel-phosphorus-graphene oxide nanocomposite coatings

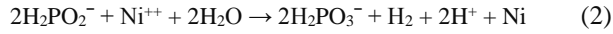
Thickness, crystallite size, and lattice strain values of the specimens with different P contents are given in Table 5. As indicated, the higher values of pH has expanded the thickness of the coating. Previous researches have also stated that increasing the pH in the acidic range results in an increase in the thickness of the coating, and when the pH reaches the neutral point, the thickness of the coating starts to reduce. The thickness of the coating in the basic range reaches its lowest level [21]. The general reaction of nickel ion reduction by hypophosphite can be considered as relation (1).

TABLE 5. Thickness, crystallite size, and lattice strain of Ni-P-GO nanocomposite coatings

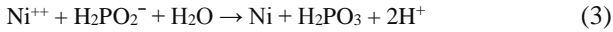
Specimens	Low (P)	Medium (P)	High (P)
Thickness (μm)	1.24	2.19	3.01
Crystallite size (nm)	41	37	25
lattice strain	2186.636363	2358.723558	3490.909090



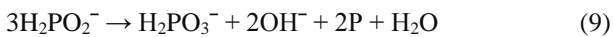
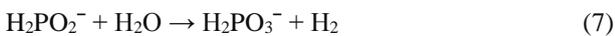
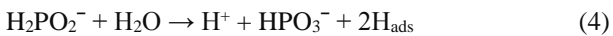
The above reaction can also be formulated as in Relation (2):



Moreover, some changes are made as seen in Relation (3):



All of these reactions take place on the catalytically active surface by applying external energy, i.e. heating the solution to a temperature between 60 and 95°C. In addition to the formation of metallic nickel, some molecular hydrogen is also produced, which is removed during heat treatment [22]. Apart from these changes, the formation of H⁺ ions leads to further acidification of the bath, while orthophosphate (H₂PO₃⁻) ions will also form. The nature of the partial reactions involved during precipitation of nickel ions in solution by reduction with the use of sodium hypophosphite has not yet been fully understood. According to studies, partial reactions of the process are given in Relations (4 to 9) [22].



All of the above steps occur during reduction reactions simultaneously. The rate of these reactions depends on various factors in the bath such as pH, temperature, and chemical composition. From Relations (8) and (9), it can be concluded that in addition to nickel, the phosphorus element is also formed in the coating. In general, Reaction 8 is slower than Reaction 3. If the pH decreases, reactions (8) and (9) tend to proceed towards the formation of more phosphorus in the coating while Reactions (5) and (3) tend to proceed towards nickel decrease.

Therefore, a decrease in pH leads to a decrease in the rate of Ni-P deposition, while the amount of phosphorus in the coating also increases.

Fig. 6 demonstrates the hardness changes of the specimens with increasing the phosphorus content. Composite coating formation increases the hardness of the coating due to creation of obstacles to the movement of dislocations. Therefore, the hardness of composite coatings is naturally higher than that of non-composite coatings.

Increasing the amount of phosphorus has resulted in a decrease in hardness. At first glance, the increase in phosphorus levels due to the increase in precipitates

should have led to an increase in hardness. However, with increasing phosphorus levels, the hardness in this study has decreased.

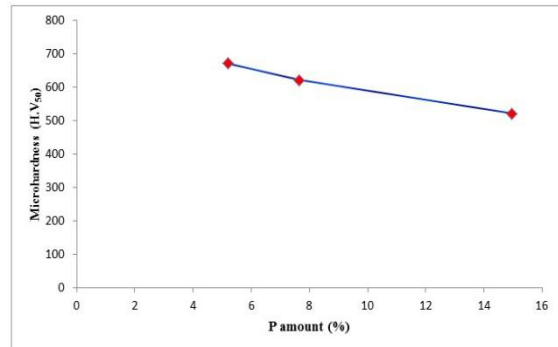


Figure 6. Variations of hardness in terms of coating P content

As shown in Table 5, with increasing phosphorus content, the nucleation of Ni₂P compounds within crystallites leads to an increase in lattice strain and, consequently, an decrease in the size of the crystallites, which in turn increases the crystallization of the coating due to compressive residual stress. The growth of new nuclei within the grains has led to an increase in size, which has resulted in a reduction in hardness. In Fig. 7, polarization corrosion diagram of all specimens is represented.

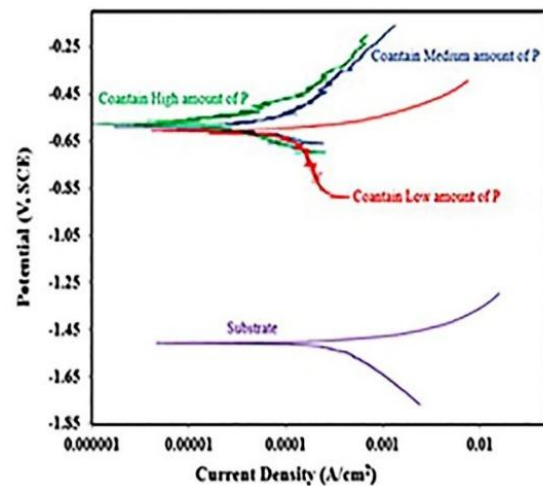


Figure 7. Polarization curves of the specimens containing different phosphorous content

The information extracted from Fig. 7 is presented in Table 6. As it is obvious, with increasing the amount of phosphorus, i_{corr} has decreased and the potential has shifted to the positive values. As the amount of phosphorus increases, the density of the phosphorous-rich layer on the surface increases during corrosion which in turn controls the current rate.

TABLE 6. Parameters extracted from polarization curves

Specimens	i_{corr} (A/cm ²)	E_{corr} (V)	Ba (V/Dec.)	Bc (V/Dec.)	Rp (Ω .cm ²)
Substrate	29.00E-05	-1.51	0.060	0.22	70.59
Low (P)	12.00E-05	-0.62	0.087	0.056	314.81
Medium (P)	2.90E-05	-0.59	0.117	0.074	678.72
High (P)	1.74E-05	-0.56	0.111	0.118	1689.50

The literature reports on Ni–P coatings indicate that preferential dissolution of nickel occurs at open circuit potential, leading to the enrichment of phosphorus on the surface layer. The enriched phosphorus surface reacts with water to form a layer of adsorbed hypophosphite anions (H₂PO₂⁻). This layer in turn will block the water supply to the metal surface, thereby preventing the hydration of nickel, which is considered to be the first step to form either soluble Ni²⁺ species or a nickel passive film [23-25]. On the other hand, as shown in the previous sections, the absorption of graphene oxide increases with increasing the amount of phosphorus in the composite coating, which is also effective in reducing the corrosion rate.

Immediately after immersion of the coating inside the corrosive solution, nickel begins to dissolve, resulting in increased current density. After a short time, the current begins to decrease to reach a stable level due to the formation of a passive layer on the surface. Elsener et al. reported that by placing the coating in chloride corrosive environments, the dissolution rate of nickel would be higher than that of phosphorus. Therefore, a two-layer passive film consisting of a phosphate layer and a phosphorous-rich layer forms on the surface. [23]. The presence of the passive phosphate layer on the raw coatings and oxide layer on the heat-treated coatings are the reasons for achieving good corrosion resistance of these coatings [24].

The presence of the passive region is observed for all specimens in the polarization curves. It can be seen that the lowest density of passive current and the greatest range of passive potential are related to the coating with the highest phosphorus content. Specimens coated with the medium phosphorus and high phosphorus contents have the highest corrosion resistance, lowest current density, and maximum corrosion potential of all other specimens and the substrate without any coating exhibits the lowest corrosion resistance among the other specimens. This indicates that in any case, the coating improves corrosion resistance.

In general, all nickel-phosphorus electroless coatings exhibit good corrosion resistance [22]. The reason for this is related to the presence of phosphorus atoms in the coating structure. In fact, by placing the specimens in the corrosive environment and dissolving nickel, the surface is enriched with phosphorus atoms, which in response to the water molecules form an absorbent layer of hypophosphite anions. This layer acts as a protective barrier, preventing water molecules to reach the surface

of the coating, hydrating the nickel, and further dissolving it [25, 26].

This research can help researchers achieve high hardness and corrosion resistance in nanocomposite coatings before heat treatment and is effective in selecting the optimal parameters for the application of electroless nanocomposite coatings on magnesium alloys.

4. CONCLUSIONS

From the present study, it can be concluded that:

- 1) As the amount of phosphorus in the coating increases, the size of the colonies in the coating with the morphology of the cauliflower decreases.
- 2) With increasing the phosphorus in the coating, the absorption rate of graphene oxide nanoplates increases.
- 3) Increasing the amount of phosphorous in the coating, increases the crystallinity of the coating and the intermediate phase of Ni₂P.
- 4) With invreasing the amount of phosphorus, the thickness of the coating increased from 1.24 to 3.01 μ m.
- 5) As the amount of phosphorus in the coating increases, the hardness of the coating decreases. the minimum hardness in the specimen containing 14.97 wt.% phosphorus was measured 521 H_{v50}.
- 6) With increasing the amount of phosphorus in the coating, the corrosion resistance of the coating increases. The lowest current density (1.74E-05 A/cm²) and the highest corrosion resistance (1689.50 Ω .cm²) were obtained in the sample containing the highest phosphorus.

5. ACKNOWLEDGMENTS

The authors would like to thank you the staffs of ceramic shaping laboratory of materials and energy research center, specially Y. Shajari and E. Jabari, for their technical supports.

REFERENCES

1. Gu, C., Jiang, Z., "Multilayer Ni-P Coating for Improving the Corrosion Resistance of AZ91D Magnesium Alloy", *Advanced*

- Engineering Materials*, Vol. 7, No. 11, (2005), 1032-1036. <https://doi.org/10.1002/adem.200500136>
2. Kanta, A. F., Vitry, V., Delaunois, F., "Wear and corrosion resistance behaviours of autocatalytic electroless plating", *Journal of Alloys and Compounds*, Vol. 486, No. 1-2, (2009), L21-L23. <https://doi.org/10.1016/j.jallcom.2009.07.038>
 3. Hu, R., Su, Y., Liu, Y., Liu, H., Chen, Y., Cao, C., Ni, H., "Deposition Process and Properties of Electroless Ni-P-Al₂O₃ Composite Coatings on Magnesium Alloy", *Nanoscale Research Letters*, Vol. 13, No. 1, (2018), 1-8. <https://doi.org/10.1186/s11671-018-2608-0>
 4. Ashtiani, A. A., Faraji, S., Iranagh, S. A., Faraji, A. H., "The study of electroless Ni-P alloys with different complexing agents on Ck45 steel substrate", *Arabian Journal of Chemistry*, Vol. 10, (2017), S1541-S1545. <https://doi.org/10.1016/j.arabj.2013.05.015>
 5. Thirumalaikumarasamy, D., Shanmugam, K., Balasubramanian, V., "Corrosion performance of atmospheric plasma sprayed alumina coatings on AZ31B magnesium alloy under immersion environment", *Journal of Asian Ceramic*, Vol. 2, No. 4, (2014), 403-415. <https://doi.org/10.1016/j.jascer.2014.08.006>
 6. Rao, K. P., Sankar, A., Rafi, H. K., Ram, G. J., Reddy, G. M., "Friction surfacing on nonferrous substrates: a feasibility study", *The International Journal of Advanced Manufacturing Technology*, Vol. 65, No. 5-8, (2013), 755-762. <https://doi.org/10.1007/s00170-012-4214-0>
 7. Liu, Q., Ma, Q. X., Chen, G. Q., Cao, X., Zhang, S., Pan, J. L., Zhang, G., Shi, Q. Y., "Enhanced corrosion resistance of AZ91 magnesium alloy through refinement and homogenization of surface microstructure by friction stir processing", *Corrosion Science*, Vol. 138, (2018), 284-296. <https://doi.org/10.1016/j.corsci.2018.04.028>
 8. Han, H. M., Wang, D. T., Yu, H. Q., Zuo, M., Wang, L. H., Zhao, D. G., "Ceria Coatings Prepared by Sol-Gel Approach on AZ91 Magnesium Alloy", In *Materials Science Forum*, Vol. 898, (2017), 1369-1380, Trans Tech Publications Ltd. <https://doi.org/10.4028/www.scientific.net/msf.898.1369>
 9. Zhang, J., Song, Z., Yu, G., Hu, B., Zhang, X., "Corrosion Behavior of Electroless Ni-P/Ni-B Coating on Magnesium Alloy AZ91D in NaCl Environment", *International Journal of Electrochemical Science*, Vol. 11, (2016), 10053-10066. <https://doi.org/10.20964/2016.12.57>
 10. Huang, C. A., Yeh, Y. H., Lin, C. K., Hsieh, C. Y., "Copper Electrodeposition on a Magnesium Alloy (AZ80) with a U-Shaped Surface", *Materials*, Vol. 7, No. 11, (2014), 7366-7378. <https://doi.org/10.3390/ma7117366>
 11. Shajari, Y., Alizadeh, A., Seyedraoufi, Z. S., Razavi, S. H., Shamakhi, H., "The effect of heat treatment on wear characteristics of nanostructure Ni-B coating on marine bronze", *Materials Research Express*, Vol. 6, No. 10, (2019), 105040. <https://doi.org/10.1088/2053-1591/ab395d>
 12. Serin, I. G., Göksenli, A., Yüksel, B., Yildiz, R. A., "Effect of Annealing Temperature on the Corrosion Resistance of Electroless Ni-B-Mo Coatings", *Journal of Materials Engineering and Performance*, Vol. 24, No. 8, (2015), 3032-3037. <https://doi.org/10.1007/s11665-015-1568-0>
 13. Shajari, Y., Porhonor, M., Seyedraoufi, Z. S., Razavi, S. H., Baghdadabadi, D. M., Yusefnia, H., Farahani, M., "Improvement of the NiBrAl casting alloy surface properties by electroless Ni-B plating for dynamic marine application", *Physical Mesomechanics*, Vol. 23, No. 1, (2020), 81-88. <https://doi.org/10.1134/s1029959920010087>
 14. Jiang, J., Chen, H., Zhu, L., Qian, W., Han, S., Lin, H., Wu, H., "Effect of heat treatment on structures and mechanical properties of electroless Ni-P-GO composite coatings", *RCS Advances*, Vol. 6, No. 110, (2016), 109001-109008. <https://doi.org/10.1039/c6ra22330c>
 15. Wu, H., Liu, F., Gong, W., Ye, F., Hao, L., Jiang, J., Han, S., "Preparation of Ni-P-GO composite coatings and its mechanical properties", *Surface and Coating Technology*, Vol. 272, (2015), 25-32. <https://doi.org/10.1016/j.surfcoat.2015.04.028>
 16. Oraon, B., Majumdar, G., Ghosh, B., "Improving hardness of electroless Ni-B coating using optimized deposition conditions and annealing", *Materials & Design*, Vol. 29, No. 7, (2008), 1412-1417. <https://doi.org/10.1016/j.matdes.2007.09.005>
 17. Loto, C. A., "Electroless Nickel Plating : A Review", *Silicon*, Vol. 8, No.2, (2016), 177-186. <https://doi.org/10.1007/s12633-015-9367-7>
 18. Zhang, W. X., Jiang, Z. H., Li, G. Y., Jiang, Q., Lian, J. S., "Electroless Ni-P/Ni-B duplex coatings for improving the hardness and the corrosion resistance of AZ91D magnesium alloy", *Applied Surface Science*, Vol. 254, No. 16, (2008), 4949-4955. <https://doi.org/10.1016/j.apsusc.2008.01.144>
 19. Portnoi, V. K., Leonov, A. V., Fedotov, S. A., "Solid-phase synthesis in Ni-Mg and Ni-Mg-C systems upon ball milling of powder mixtures", *Bulletin of the Russian Academy of Sciences: Physics*, Vol. 73, No. 9, (2009), 1211. <https://doi.org/10.3103/s1062873809090081>
 20. Baskaran, I., Kumar, R. S., Narayanan, T. S., Stephen, A., "Formation of electroless Ni-B coatings using low temperature bath and evaluation of their characteristic properties", *Surface and Coatings Technology*, Vol. 200, (2006), No. 24, 6888-6894. <https://doi.org/10.1016/j.surfcoat.2005.10.013>
 21. Czagány, M., Baumli, P., "Effect of pH on the characteristic of electroless Ni-P coatings", *Journal of Mining and Metallurgy Section B Metallurgy*, Vol. 53, No. 3, (2017), 327-332. <https://doi.org/10.2298/jmmb170530020c>
 22. Riedel, W., *Electroless Nickel Plating*, Metals Park, Ohio: ASM International, (1991).
 23. Ashassi-Sorkhabi, H., Es'haghi, M., "Corrosion resistance enhancement of electroless Ni-P coating by incorporation of ultrasonically dispersed diamond nanoparticles", *Corrosion Science*, Vol. 77, (2013), 185-193. <https://doi.org/10.1016/j.corsci.2013.07.046>
 24. Elsener, B., Crobu, M., Scorciapino, M. A., Rossi, A., "Electroless deposited Ni-P alloys: corrosion resistance mechanism", *Journal of Applied Electrochemistry*, Vol. 38, No. 7, (2008), 1053-1060. <https://doi.org/10.1007/s10800-008-9573-8>
 25. Bozzoni, B., Lenardi, C., Serra, M., Fanigliulo, A., "Electrochemical and X-ray photoelectron spectroscopy investigation into anodic behaviour of electroless Ni-9.5 wt%P in acidic chloride environment", *British Corrosion Journal*, Vol. 37, No. 3, (2002), 173-181. <https://doi.org/10.1179/000705902225006589>
 26. Ghavidel, N., Allahkaram, S. R., Naderi, R., Barzegar, M., Bakhshandeh, H., "Corrosion and wear behavior of an electroless Ni-P/nano-SiC coating on AZ31 Mg alloy obtained through environmentally-friendly conversion coating", *Surface and Coating Technology*, Vol. 382, (2020), 125156. <https://doi.org/10.1016/j.surfcoat.2019.125156>

AIMS AND SCOPE

Advanced Ceramics Progress (ACERP) as an ISC international journal is devoted to elucidating the fundamental aspects of chemistry and physics occurring at a wide range of oxide and nonoxide ceramics and composite materials and their processing, microstructure, properties, and applications. The journal provides a unique venue for publishing new exciting research, focusing on dynamic growth areas in this field.

INSTRUCTIONS FOR AUTHORS

Submission of manuscript represents that it has neither been published nor submitted for publication elsewhere and is result of research carried out by author(s).

Authors are required to include a list describing all the symbols and abbreviations in the paper. Use of the international system of measurement units is mandatory.

- On-line submission of manuscripts results in faster publication process and is recommended. Instructions are given in the ACERP web site: www.acerp.ir
- Hardcopy submissions must include MS Word and jpg files.
- Manuscripts should be typewritten on one side of A4 paper, double-spaced, with adequate margins.
- References should be numbered in brackets and appear in sequence through the text. List of references should be given at the end of the paper.
- Figures' captions are to be indicated under the illustrations. They should sufficiently explain the figures.
- Illustrations should appear in their appropriate places in the text.
- Tables and diagrams should be submitted in a form suitable for reproduction.
- Photographs should be of high quality saved as jpg files.
- Tables, illustrations, figures and diagrams will be normally printed in single column width (8 cm). Exceptionally large ones may be printed across two columns (17 cm).

PAGE CHARGES AND REPRINTS

ACERP subscribers do not need to make any payment for publication and reprints.

AUTHORS CHECKLIST

- Author(s), bio-data including affiliation(s) and mail and e-mail addresses.
- Manuscript including abstract, key words, illustrations, tables, figures with figures' captions and list of references.
- MS Word files of the paper.

Advanced Ceramics Progress,
P.O. Box 31787-316, Karaj, Alborz, I. R. Iran
Materials and Energy Research Center, Imam Khomeini Blvd, Meshkin Dasht, Karaj,
Alborz, I. R. Iran
P.O. Box 14155-4777, Tehran, I. R. Iran
No. 5, Ahuramazda St., Alvand Ave., Argentine Sq., Tehran, I. R. Iran

Advanced Ceramics Progress

Volume 6, Number 3, Summer 2020

CONTENTS

S. M. Nahvi	Effect of Carbide Particle Size on the Microstructure, Mechanical properties, and Wear Behavior of HVOF-sprayed WC-17% Co Coatings	1-14
M. Khodaei, O. Yaghobizadeh, S. A. Safavi, N. Ehsani, H. R. Baharvandi, S. Esmaeeli	The Effect of TiC Additive with Al ₂ O ₃ -Y ₂ O ₃ on the Microstructure and Mechanical Properties of SiC Matrix Composites	15-24
P. Safarzadeh Kermani, M. Ghatee, A. Yazdani	Synthesis and Characterization of Barium Aluminosilicate Glass as the Sealant for Solid Oxide Fuel Cell Application	25-30
J. Esmailzadeh, H. Setayesh	Bioabsorbable Screws for Anterior Cruciate Ligament Reconstruction Surgery: A Review	31-46
M. Rezvani, E. Alahgholiyan, L. Roshangar	Synthesis of a Macroporous Glass-Ceramic Scaffold Containing Fluorapatite Crystalline Phase for Bone Substitutes	47-54
M. Hanachi, Z. S. Seyedraoufi, V. Abouei	Investigation of Microstructure, Hardness, and Corrosion Resistance of Ni-P-GO Electroless Nanocomposite Coating on AZ31D Alloy Surface	55-62



Journal Home Page: www.acerp.ir